Université de Neuchâtel

Institut de Microtechnique

Single-chamber process development of microcrystalline Silicon solar cells and high-rate deposited intrinsic layers

Thèse

Présentée à la Faculté des Sciences
pour l'obtention du titre de Docteur ès Sciences
par

Urs Samuel Graf

Octobre 2005

Université de Neuchâtel **unine**

IMPRIMATUR POUR LA THESE

Single-chamber process development of microcrystalline silicon solar cells and high-rate deposited intrinsic layers

Urs Samuel GRAF

UNIVERSITE DE NEUCHATEL

FACULTE DES SCIENCES

La Faculté des sciences de l'Université de Neuchâtel,
sur le rapport des membres du jury

MM. A. Shah (directeur de thèse),
C. Ballif,
G. Calzaferri (Berne)
et W. Beyer (Jülich, D)

autorise l'impression de la présente thèse.

Neuchâtel, le 18 novembre 2005

Le doyen :

J.-P. Derendinger

Faculté des Sciences
■ Rue Emile-Argand 11 ■ CP 2 ■ CH-2007 Neuchâtel
■ Téléphone : +41 32 718 21 00 ■ Fax : +41 32 718 21 03 ■ E-mail : secretariat.sciences@unine.ch ■ www.unine.ch

Table of Symbols

μc-Si:H	hydrogenated microcrystalline silicon
a-Si:H	hydrogenated amorphous silicon
c-Si	monocrystalline silicon
LPCVD	low pressure chemical vapor deposition
VHF-GD	very-high frequency glow-discharge
PECVD	plasma-enhanced chemical vapor deposition
VHF	very-high frequency
HPD	high-pressure depletion
ϕ(gas)	gas flow rate in sccm
SiH_4 conc.	Gas flow ratio of SiH_4/ total gas flow
SiH_4	silane
H_2	hydrogen
TMB	trimethylboron ($(CH_3)_3B$)
ZnO	zinc oxide
TCO	Transparent Conductive Oxide
PDS	Photothermal Deflection Spectroscopy
CPM	Constant Photocurrent method
FTPS	Fourier transform photocurrent spectroscopy
SEM	Scanning Electron Microscopy
TEM	Transmission Electron Microscopy
SIMS	Secondary Ion Mass Spectroscopy
EQE	External Quantum Efficiency
J_{sc}	short-circuit current density
V_{oc}	open-circuit voltage
FF	fill-factor
rms	root-mean square
E_{Urbach}	Urbach energy
α(0.8 eV)	residual absorption
ϕ_c	Raman crystallinity factor
$\sigma_{dark@RT}$	dark-current at room temperature

Table of Contents

ABSTRACT **1**

CHAPTER 1:INTRODUCTION **3**

1.1. MOTIVATION 3

1.1.1. The need for "clean" energy sources as PV *3*

1.1.2. The advantage of the Si:H thin-film technology *4*

1.2. MICROCRYSTALLINE SI:H SOLAR CELLS 5

1.2.1. The advantage of μc-Si:H solar cells *5*

1.2.2. Basics of a-Si:H and μc-Si:H solar cells *6*

1.2.2.1. Basics on the open-circuit voltage V_{oc} 7

1.2.2.2. Solar cell structure 10

1.2.2.3. Transparent conductive oxide (TCO) 10

1.2.2.4. PECVD deposition technique for μc-Si:H growth 11

1.3. CHARACTERISATION TECHNIQUES 13

1.3.1. Micro-Raman Spectroscopy *13*

1.3.2. Electrical dark-current conductivity (σ_{dark}) *17*

1.3.3. Illuminated current-voltage characteristics (JV-measurement) *17*

1.3.4. External quantum efficiency *19*

1.3.5. Measurement of the sub-gap absorption coefficient *20*

1.3.6. Microstructure characterisation by Transmission electron microscopy (TEM) .. *22*

1.3.7. Secondary Ion Mass Spectrometry (SIMS)-Analysis *22*

OUTLINE OF THIS WORK 23

CHAPTER 2: DEVELOPMENT OF μC-SI:H LAYERS AND SPECIAL TREATMENTS **25**

2.1. P-DOPED μC-SI:H LAYERS WITH TRIMETHYLBORON (TMB) INSTEAD OF DIBORANE (B_2H_6) AS DOPING GAS 25

2.1.1. Introduction *25*

2.1.2. Development of p-doped microcrystalline Si:H layers with Trimethylboron (TMB) *28*

2.1.2.1. Comparison 70.0 vs. 110.0 MHz: 30

2.1.2.2. Dilution series of TMB at 110.0 MHz 31
2.1.2.3. Hydrogen dilution series 32
2.1.2.4. Initial concentration series of TMB for 70.0 MHz 34
2.1.3. Alternative Methods for μc-Si:H TMB p-doped layers 36
2.1.3.1. H_2-Recrystallisation of amorphous p-layers 36
2.1.3.2. Influence of an intrinsic nucleation layer for TMB-doped p-layers 38
2.1.3.3. Influence of a pre-deposition plasma on the growth of the p-layer 40
2.1.4. Conclusions on p-doped μc-Si:H layers 44
2.2. DEVELOPMENT OF HIGH-RATE DEPOSITED INTRINSIC μC-SI:H LAYERS 46
2.2.1. Power series at low pressure 49
2.2.2. Pressure series up to 8 mbar for VHF-GD 51

CHAPTER 3: DEVELOPMENT OF μC-SOLAR CELLS IN A SINGLE-CHAMBER DEPOSITION SYSTEM 61

3.1. RECIPES OF THE SI:H LAYERS AND APPLIED TREATMENTS OF THE μC SOLAR CELLS . 61
3.1.1. ZnO surface pre-treatment 61
3.1.2. Recipes of TMB p-doped μc-Si:H layers 62
3.1.3. Treatments after the deposition of the p-doped layer 62
3.1.3.1. Chamber passivation by CO_2 plasma passivation: 63
3.1.3.2. Chamber covering layer: 63
3.1.3.3. Chamber cleaning by SF_6/ O_2 etching gas: 64
3.1.3.4. Chamber cleaning by etching gas & covering layer: 64
3.1.4. Recipe of intrinsic μc-Si:H layer in the low pressure regime 65
3.1.5. Recipes of n-doped Si:H layers 65
3.2. μC-SI:H SOLAR CELLS AND ANALYSIS 65
3.2.1. Chamber treatments after the p-doped layer 70
3.2.1.1. The impact of different chamber treatments on μc-Si:H solar cell 70
3.2.1.2. SIMS-analysis of boron at the p-i interfaces for the different chamber treatments 86
3.2.1.3. Correlation of defect density determined from μc-Si:H solar cell characteristics with the results of the SIMS-analysis 93
3.2.1.4. Proposed mechanism for the "J_{SC}-degradation ↔ J_{SC}-regeneration" phenomenon and V_{OC} limitation 94

3.2.2. A novel p-i-n structuring method *103*
3.2.3. Conclusions on single-chamber μc-Si:H solar cells *106*
3.3. μC-SI:H SOLAR CELLS INCORPORATING I-LAYERS DEPOSITED CLOSE TO THE HIGH-PRESSURE REGIME 108
3.3.1. Pressure series ranging from 0.5 to 3 mbar with rates up to 14.5Å/s *109*
3.3.2. Introduction of nucleation-layer for the high-pressure regime *114*

CHAPTER 4: OPTIMISATION OF HOMOGENEITY AND PLASMA CONFINEMENT BOX DESIGN 117

4.1. IMPROVEMENT OF HOMOGENEITY WITH RESPECT TO VHF-FREQUENCY AND VHF-POWER AT HIGHER PRESSURES 118
4.2. REDEVELOPMENT OF THE PLASMA CONFINEMENT BOX DESIGN 125
4.3. OPTIMISATION OF D_{GAP} FOR THE HIGH-PRESSURE REGIME 127

APPENDIX 133

A NOVEL ZNO LIFT-OFF STRUCTURING TOOL FOR P-I-N SOLAR CELLS 133
B EVOLUTION OF PLASMA CONFINEMENT BOX 136
C CHARACTERISATION OF THE PLASMA CONFINEMENT BOX 138
C.1 Calibration of $T_{substr}(T_{heater})$ *138*
C.2 Influence of the chamber pressure to the plasma confinement box *139*

REFERENCES 141

ACKNOWLEDGEMENTS 147

Abstract

The "Micromorph" tandem solar cell concept consisting of an amorphous and a microcrystalline silicon solar cell is considered to be one of the most promising concepts for the next solar cell generation. To translate this concept into action, efficient industrial processes have to be developed. Thereby important issues have to be considered, such as e.g. the development of an economical single-chamber process and the achievement of high deposition rates for intrinsic microcrystalline silicon (μc-Si:H).

The present thesis focuses on the ***single-chamber process***. The ***development*** was done under three aspects: the aspect of ***layer optimisation*** with respect to their structural and electrical characteristics, the ***chamber-design optimisation*** and the ***solar-cell tuning***.

For the present single-chamber PECVD deposition system microcrystalline p-doped μc-Si:H layers could be obtained using trimethylboron (TMB) doping gas. At low source-gas concentration values, microcrystalline p-doped μc-Si:H layers with a Raman crystallinity factor of 0.5 – 0.6 (measured on LPCVD ZnO-coated substrates) and a conductivity of 2 - 3 S/cm were obtained. A plasma excitation frequency as high as 110.0 MHz - others use 13.56 MHz- was found to be necessary to attain a sufficiently high doping level and crystallinity for these p-doped μc-Si:H layers. The search for alternative methods led to the discovery of a crucial pre-deposition plasma treatment with H_2 as well as with CO_2 on the LPCVD ZnO layer; this treatment has a beneficial effect on crystallisation during the subsequent growth of the overlying p-doped μc-Si:H layers.

In order to obtain high deposition rates for intrinsic μc-Si:H layers, pressures up to 8 mbar were used. When working in the high-pressure regime, deposition uniformity and powder formation is critical. The use of a ***novel cylindrical design of*** the ***plasma confinement box*** – the electrode is designed as a box that defines the space of the bulk plasma- led to a homogeneous deposition. Thereby, the ***deposition rate*** on ZnO could be increased ***up to about 28 Å/s***. At the same time working at an inter-electrode distance d_{gap} of 9.5 mm made ***polysilicon (powder) formation*** even ***disappear***.

In our ***single-chamber PECVD deposition system*** the use of a standard deposition process (p-doped μc-Si:H/ intrinsic μc-Si:H/ n-doped μc-Si:H) led to solar cells with poor characteristics (V_{OC} << 500 mV & FF< 0.5) accompanied by an annealing initiated ***metastable phenomenon "J_{SC}-degradation ↔ J_{SC}-regeneration"***. Only the introduction of a ***"SF_6/O_2-cleaning & a-Si:H covering layer" as chamber treatment*** after the deposition of the p-doped layer allowed us to overcome the boron cross-contamination between p-layer and subsequent i-layer – this was proved by SIMS. We suspect that boron contamination is the cause of the metastability mentioned above, via Fe_i^+ centres. Hereby, Fe_i^+ irons are activated

by the annealing process and act then as recombination centres within the intrinsic layer. The best μc-Si:H solar cell with a typical microcrystalline V_{OC} of 516 mV, a FF of 0.685 and a J_{SC} of 18.5 mA/cm^2 leading to an efficiency of 6.5 %. SIMS-Analysis allowed us to quantify the boron contamination in the intrinsic layer for the various cases studied. The observed metastable degradation is suspected to be based on an ***equilibrium reaction*** changing by annealing an “inactive” iron atom within a ***FeB complex*** into a dissociated***,*** very strongly active ***Fe_i^+ ion.***

The incorporation of intrinsic μc-Si:H layers (deposited at rates up to 14.5 Å/s) in the high–pressure regime, e.g. at pressures of 3 mbar, however, led so far to solar cells with poor characteristics (V_{OC}≈ 200- 300 mV, FF≈ 0.3- 0.4 & J_{SC}< 12 mA/cm^2). Combined with an highly microcrystalline nucleation layer, the external quantum efficiency (EQE) could be slightly increased, but solar cell characteristics remained poor.

Finally, a ***novel structuring*** method ***by ZnO lift-off*** led to a ***substantial increase in the uniformity of the solar cell characteristics*** (V_{OC} and FF) compared to the previous standard structuring method.

Chapter 1: Introduction

1.1. Motivation

1.1.1. The need for "clean" energy sources as PV

The industrialisation in the 19th century established the modern society of the western countries with an increasing need of energy. In Switzerland the ***energy consumption has increased sixfold since 1950*** [1]. Due to the wasteful use of non-renewable energy resources such as coal, gas, nuclear energy and oil, serious problems for the environment (pollution and change in climate by the greenhouse effect [2]) can be expected. Oil will be exhausted in close future, as the well known geologist Colin Campbell emphasizes by his statement "The Peak of Oil[1] has already been exceeded now" [3].

Due to the proven, crucial ecological problems linked to non-renewable energy resources which will threaten mankind for the next generations, humanity has to look ahead to a near future using renewable energy sources, such as photovoltaic energy.

The energetic ***potential of solar irradiation on the Earth's surface*** (1.08×10^{18} kWh/year are received) is enormous and ***exceeds 15'000-folds the world wide energy demand*** [4], e.g. the ***solar power received during less than one hour could cover the whole yearly demand*** [5].

Therefore, the effort to enhance the use of the solar energy directly by using photovoltaic conversion as well as indirectly by the use of wind-, wave-, hydraulic-, and biomass-power is indeed a logic consequence.

Increased prices and prognosis for even higher prices of the "old fashioned, low-priced" energy resource oil were observed in recent times (price per barrel: "London's International Petroleum Exchange, August Brent was at $58.76 a barrel" [6]); this will hopefully contribute to increase the will to invest in renewable energies, such as photovoltaics.

---

[1] „Peak of Oil" denotes here the maximum-exploitation after a fast, steep growth followed by fast, steep decline in the term of a spiky Gaussian exploitation-curve model as function of the time, e.g. after the maximum half of the source capacity is exploited.

1.1.2. The advantage of the Si:H thin-film technology

At present, the PV market is still largely dominated by the crystalline silicon (c-Si) and poly- (or "multi-") crystalline silicon (poly-Si) technologies. However, the increased shortage of raw “highly purified” silicon -needed as a source for the product of c-Si and poly-Si solar cells- have made solar cell producers interested in silicon thin-film technology. Thus, thin-film solar cells, more particularly amorphous silicon (a-Si:H) thin-film solar cells and, even more importantly the so-called "Micromorph" (microcrystalline/amorphous) tandem solar cell concept, become more and more attractive. In the latter case, an a-Si:H solar cell can be advantageously combined with a microcrystalline silicon (μc-Si:H) solar cell, leading to higher efficiencies of up to 13 % (initial) module efficiency [7]. This technology has been pioneered by our group at IMT Neuchâtel [8, 9], but is now developed by many groups world-wide [10-12].

However, in order to obtain low production costs for the thin-film Si:H modules, a high output is needed and this must be obtained by fast industrial fabrication processes. Therefore, high deposition rates for device-grade μc-Si:H material is needed (among other aspects). The subject of high deposition rates is one of the issues of the present work.

Thin-film Si:H solar cells are now developed by Unaxis’ semiconductor equipment department (previous “Display Department”). Unaxis are adapting their Kai™ single-chamber deposition system – which is a PECVD production tool for displays- to the demands of thin-film Si:H solar cells [13, 14].

Thin-film Si:H solar modules have numerous attractive attributes compared to "traditional" wafer-based silicon modules. The main one is probably their ***substantial potential for cost reduction*** in the medium term. In silicon thin-film technology, only a very thin layer of a total thickness of some micrometers (μm) of silicon is used, whereas wafer-based technology (c-Si and poly-Si) uses silicon slices of about 300 μm thickness. The substrate on which the active thin-film silicon layers are deposited is usually glass (current developments are also devoted to flexible substrates such as plastics). In addition, silicon thin-film technology requires far less fabrication energy than wafer-based technology. Thus, the energy payback time of thin-film silicon solar cells is consequently reduced.

Moreover, compared to other thin-film technologies currently under development and being presently industrialized (CIGS, CdTe), silicon thin-films have the key advantage of using silicon as raw material, a raw material that is non-toxic and widely available in the earth’s crust. Furthermore, synergies with the flat panel display reactors, where equipment for large area deposition of a-Si thin-film transistors has already been developed.

1.2. Microcrystalline Si:H solar cells

It was in 1968 when the history of microcrystalline silicon (μc-Si:H) started. Veprek and Marecek [15] deposited first a microcrystalline silicon semiconductor layer, using CVD in a hydrogen plasma at temperatures about 600°C. Nevertheless, it took some more decades until the pioneering work for first μc-Si:H solar cells were first reported in 1991 by G. Lucovsky et al. [16] and further improved in 1994 by J. Meier et al. at IMT [8].

1.2.1. The advantage of μc-Si:H solar cells

The microcrystalline silicon material is reported to be a quite complex material consisting of an amorphous matrix with embedded crystallites plus grain boundaries [17].

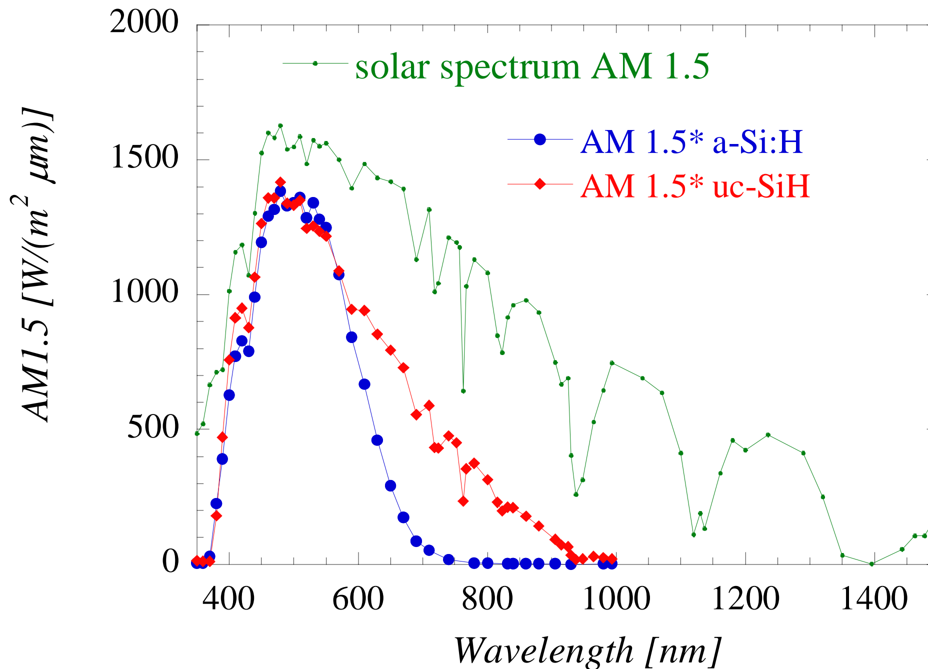

Fig. 1.1: Spectral distribution of the AM1.5 solar spectrum incident on the Earth's surface. The spectral curves of the light absorbed by a-Si:H and μc-Si:H solar cells (calibrated on AM1.5), respectively, are indicated.

Although this material has a complex microstructure, its optical properties have a marked crystalline characteristic: an optical gap at 1.12 eV like c-Si. This implies the spectral absorption of μc-Si:H covers a much larger range than a-Si:H which posses an optical gap between 1.6 and 1.75 eV [18]. Compared to a-Si:H that absorbs light up to 800 nm, μc-Si:H absorbs light coming from a wider spectral range, extending up to 1100 nm (see Fig. 1.1). On the other hand, within its range of absorption, the absorption of a-Si:H is higher than that of μc-Si:H –due to the indirect gap of the latter. Therefore, the optical combination of these two materials takes advantage of a larger part of the solar spectrum (compared to a single-junction

cell) and the conversion efficiency of the incident light into electricity can be consequently improved.

Furthermore, the μc-Si:H solar cell is reported to be largely stable against light induced degradation [19].

1.2.2. Basics of a-Si:H and μc-Si:H solar cells

Technologically, μc-Si:H is closely related to hydrogenated amorphous silicon (a-Si:H): the deposition technique for both materials is the same. For this, key-deposition parameters (such as temperature, silane concentration, H_2-flow, power, frequency and pressure) have to be adapted such as to obtain either a-Si:H or μc-Si:H material.

On the other hand, μc-Si:H can be considered as nothing else but a (complex) mixture between crystalline silicon (c-Si) and a-Si:H. Therefore, it is of high interest to present the basic characteristics of a-Si:H before studying μc-Si:H.

a-Si:H is a solid-state material made of silicon atoms which are arranged in a short range order, but not in a long range order. Compared to crystalline silicon (c-Si), the average bond angles between nearest-neighbouring atoms are distorted. Some bonds are even broken and result in so-called "dangling bonds". The presence of hydrogen during the fabrication of amorphous silicon material enables a passivation of a large part of these dangling bonds. These two main "defects" of the lattice of a-Si:H - bond distortion and dangling bonds - give rise to an electronic band structure comprising localised states within the so-called "mobility" band gap (see Fig. 1.2). Note that the value of the "optical" band gap that is extrapolated from optical measurements can be slightly different from that of the “mobility” gap.

The bond distortion results in ***band tails*** near the valence and conduction bands. In these band tails, the electrons (or holes) are localised in space and do not participate (directly) in the electronic transport. The (non-passivated) ***dangling bonds*** create deep states near the middle of the band gap. They can either be positively charged (i.e. absence of electron, D^+), neutral (i.e. one electron, D^0) or negatively charged (i.e. two electrons, D^-). The ***dangling bonds act as recombination centres for free electrons and holes***, and lead to ***two recombination*** paths: one over $\boldsymbol{D^0/D^-}$ and one over $\boldsymbol{D^+/D^0}$ (see Fig. 1.2). They can as well indirectly affect the electronic transport by influencing the total electric charge.

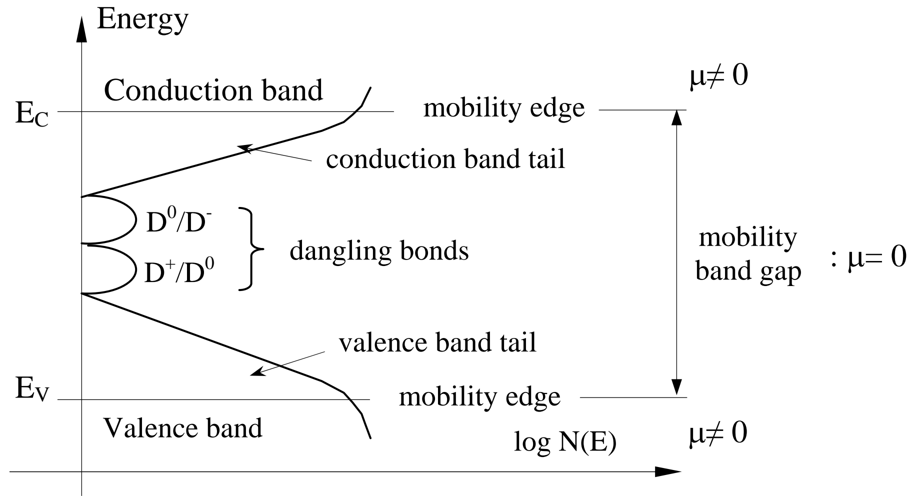

Fig. 1.2: Density of states N(E) for intrinsic a-Si:H. Within the mobility band gap (delimited by E_C and E_V), the states are localised (dangling bonds and band tails): $\mu = 0$ (@ T=0 K).

In a-Si:H as well as ***in μc-Si:H, hydrogen has the important role to reduce*** (by passivation) the ***density of dangling bonds***, or "recombination centres". Hereby the material can be made "device-grade", i.e. suitable for use in optoelectronic devices like solar cells and detectors. However, extrinsic contaminants, such as oxygen, ionized iron (well known in c-Si as a contaminant), can as well act as unintentional recombination centres.

The difference in the range of absorption of a-Si:H and μc-Si:H, as shown in Fig. 1.1, is due to different band gap energy values (E_g). For a-Si:H material, $E_g \approx 1.75$ eV, whereas for highly microcrystalline silicon $E_g \approx 1.12$ eV, similarly to c-Si. Due to the indirect gap characteristics and the lower band gap E_g of μc-Si:H, its absorption above the band gap is lower than that of a-Si:H (that has a so-called "non-direct" gap [20]).

1.2.2.1. Basics on the open-circuit voltage V_{oc}

A solar cell which is illuminated, generates a voltage at its contacts, in the forward bias polarity (+ to p and - to n-layer) as sketched in Fig. 1.3 This forward bias results in a forward dark-current I_{dark} opposite to the photocurrent I_{ph}. When the superposition principle can be applied, it is shown that the gained cell current output I_{out} is a part of I_{ph}, as given by equation (Equ. 1.1):

$$I_{ph} = I_{out} + I_{dark} \qquad \text{Equ. 1.1}$$

Note that in practice for p-i-n amorphous silicon thin-film solar cells, the superposition principle is not entirely applicable. In the present case p-n junctions are described [21].

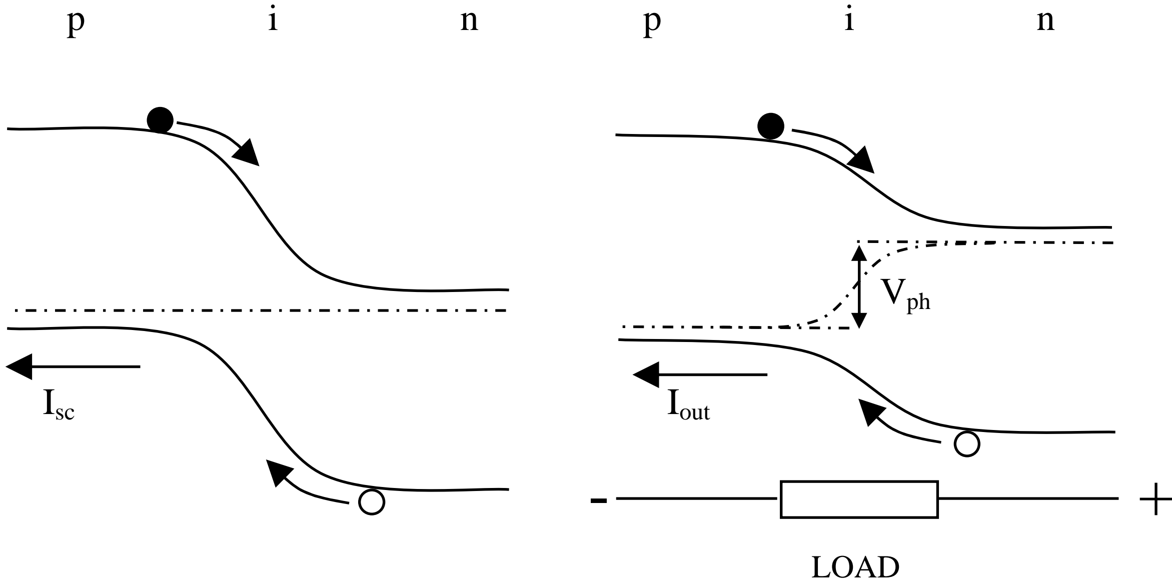

Figure 1.3: Schematic band diagram of p-i-n solar cell under illumination. On the left, the cell is under short-circuit conditions whereas on the right, the cell is connected to a load. On the right, the voltage generated V_{ph} at the output of the device stems from the difference between the quasi–Fermi levels.

The dark-current in the forward direction is consequently as significant as the photo-generated current in order to understand the cell behaviour. Several mechanisms add-up to form the dark-current as shown in Figure 1.4. All these mechanisms depend on the doping level of the doped layers (p-n junction):

- The ***diffusion current*** I_{inj}: electrons diffusing from the n-layer to the p-layer. (The same mechanism applies for holes from the p-layer to the n-layer.) This mechanism depends on the possible potential barriers or potential spikes that may exist in the band diagram of the junctions. An amorphous layer or a change of nuclei density at p-i interfaces (in p-i-n configurations) could affect I_{inj} in µc-Si:H solar cells.
- The minority ***recombination-generation current*** I_{rg}: carriers injected in the depletion region recombine through gap states such as deep defects. This is likely to be the most important mechanism in p-i-n µc-Si:H solar cells (see chapter 3.2).
- The ***tunneling current*** I_{tun}: carriers injected in the depletion region tunnel from valence or conduction band into states within the band-gap. Then the carriers either recombine or tunnel again into band-gap states towards the other band.

The sum of these contributions results in the total dark-current:

$$I_{dark} = I_{diff} + I_{rg} + I_{tun} \qquad \text{Equ. 1.2}$$

In p-n mono-crystalline silicon solar cells the first contribution I_{diff} is the most significant, for p-i-n and n-i-p solar cells, the second term (I_{rg}) plays an important role and the third term (I_{tun}) appears mostly important in hetero-junctions [21]. The third term I_{tun} will not be taken into account in the following discussion.

•

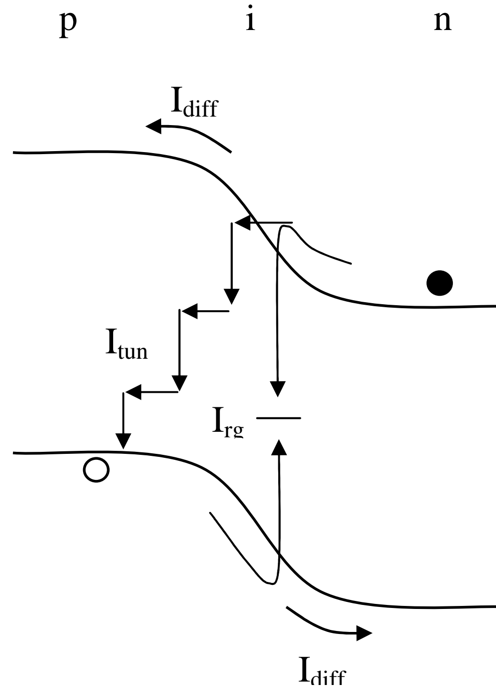

Fig. 1.4: Components of the dark-current in a p-i-n junction: diffusion current I_{diff}, multi-step tunneling current I_{tun} and minority generation-recombination current I_{rg} .

In the case of an ideal diode, the dark-current I_{dark} is given (Equ. 1.3) by

$$I_{dark} = I_0 (e^{qV/nkT} - 1) \qquad \text{Equ. 1.3}$$

where the exponential pre-factor I_0 (diode saturation current) and the diode ideality factor n are used to approximate the sum of I_{diff} and I_{rg}. V is the applied voltage, k the Boltzmann constant, T is the absolute temperature and q the charge of the electron. Under open-circuit conditions, I_{out} (in Equ. 1.1) is obviously zero and I_{dark} equals I_{ph}. The following formula can be, thus, derived for the V_{oc}:

$$V_{oc} = \frac{nkT}{q} \ln(\frac{I_{ph}}{I_0} + 1) \qquad \text{Equ. 1.4}$$

1.2.2.2. Solar cell structure

The thin-film silicon solar cell configuration used here is of p-i-n type, the first letter (p) indicating which of the layers was first deposited on the substrate. The structure is constituted of a p-doped layer, an intrinsic (i-) layer and a n-doped layer sandwiched between a front and back transparent conductive oxide (TCO). The whole structure is supported by a substrate, e.g. glass. The cell configuration is said to be p-i-n, as light should preferably enter the p-layer side first; the p-i-n cells must, therefore, be deposited on transparent substrates.

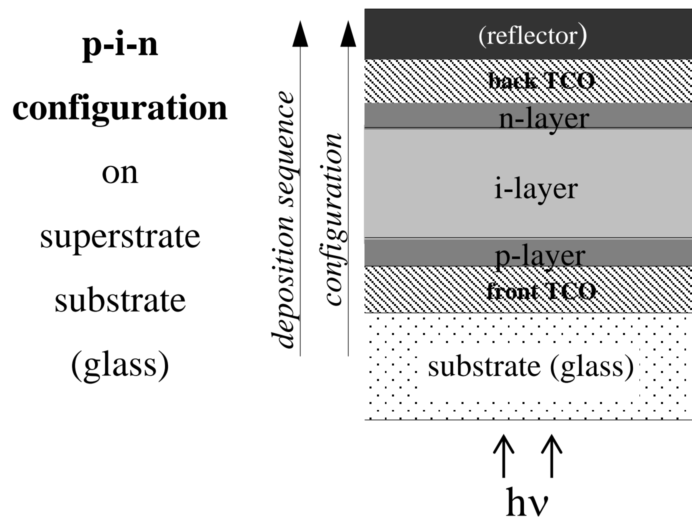

Fig. 1.5: Schematic structure of p-i-n solar cell configuration on glass.

1.2.2.3. Transparent conductive oxide (TCO)

The most commonly used TCO in the Neuchâtel group is ZnO obtained by low-pressure chemical vapour deposition (LPCVD) from a vapour mixture of diethyl zinc, water and diborane (doping) [22]. As grown LPCVD ZnO is rough: rms-roughness of 60 nm for a thickness of 2.4 μm. Thus, it constitutes a light diffuser that enhances the light trapping within the solar cell.

One should mention that ZnO is not the only TCO available: indium tin oxide (ITO), tin oxide (SnO_2) are also used in photovoltaics.

1.2.2.4. PECVD deposition technique for μc-Si:H growth

The growth of μc-Si.H material uses silane (SiH_4) and hydrogen (H_2) as source-gas. It is currently admitted that free radical precursors ($SiH_x^{\bullet}$[2]) – $SiH_3^{\bullet}$ is suspected to favour the μc-Si:H growth- and $H^{\bullet}$ - enhances crystalline growth by etching of looser a-Si:H tissue- were needed to attain microcrystalline growth. In order to obtain such reactive species, decomposition of the source-gases is necessary.

At first, this was obtained by using CVD at high temperatures (600°C) [15].

The use of low deposition temperatures of 200-300°C with a plasma present in the deposition chamber, the so called Plasma-Enhanced Chemical Vapour Deposition technique (PECVD) was developed later on [23, 24] and allowed the low-temperature deposition of μc-Si:H layers. The amorphous or microcrystalline nature of the deposited material depends on the value of the different deposition parameters that have to be adjusted.

The use of plasma excitation frequencies in the very high frequencies (VHF) range (70 to 130 MHz) was pioneered by our group at IMT. Compared to standard RF frequency (13.56 MHz), it leads to a remarkable increase of the deposition rate (of both a-Si:H and μc-Si:H samples) while still retaining good material quality [25]. In the VHF range, the sheath potential is reduced, leading to a reduced peak ion energy and, thus, to less energetic ion-bombardment [26]. However, other groups obtain comparable deposition rates for increased working pressure when using 13.56 MHz [27].

Recent research has not only focussed on increased efficiency of the "Micromorph" tandem solar cells, but also on high-rate deposition (> 10Å/s) of μc-Si:H. To attain this goal, several techniques using higher pressures (> 1 mbar) were proposed, i.e. High-pressure RF-PECVD [28] and a combination of VHF and High-pressure [29, 30]. In the latter case silane is depleted and the technique is, therefore, also known as HPD (High-Pressure Depletion). *All these techniques show promising results for μc-Si:H solar cells with conversion efficiencies η in the range of 8 - 10 % for deposition rates of 10 Å/s and more.*

The main deposition parameters are the following:

- The ***plasma excitation frequency***: The change from standard RF (13.56 MHz) to the increased VHF-range up to about 130 MHz is an important parameter which obviously increases the deposition rate of μc-Si:H. Moreover the VHF-range has a favourable impact to the growth of μc-Si:H material [31].
- The ***working-pressure*** of the chamber during the deposition: It was recently reported

[2] The chemical nomenclature denotes a free-radical with a superscripted dot; in our case, as follows, $SiH_x^{\bullet}$ and $H^{\bullet}$

that the use of higher pressures (> 1mbar) leads to an increased deposition rate of μc-Si:H. However, pumping rate and the gas feeding rates can be limiting parameters in this deposition regime. In the present work, we differentiate between the low-pressure (< 1 mbar) and the high-pressure regime ($1 < p < 10$ mbar). High pressures allow for a decreasing ion-bombardment which is favourable for the growth of μc-Si:H layers but generally demand for higher plasma excitation power. However, very high plasma excitation power (> $1 W/cm^2$) is unfavourable for growth of μc-Si:H layers. It increases the voltage drop at the sample surface, e.g. the impact on the growth surface is stronger. Defective material can, therefore, not be excluded in the high-pressure regime. Moreover, it is observed that the use of high-pressures can lead to the regime of polysilane formation (powder), if the inter-electrode distance d_{gap} is too large, e.g. $d_{gap} > 10$ mm (chapter 4.3).

- The ***silane concentration*** *c(SiH₄)* in the plasma gas phase: $c(SiH_4) = \phi(SiH_4)/(\phi(SiH_4)+\phi(H_2))$ is a key parameter that is most effective in changing the structure of the deposited layer from amorphous material (at high *$c(SiH_4)$-values*) to microcrystalline material (at low *$c(SiH_4)$-values*). In a narrow range of $c(SiH_4)$, there is the occurrence of a "μc-Si:H / a-Si:H transition". This range is of practical interest, as the best μc-Si:H solar cells contain i-layers deposited with $c(SiH_4)$-values within this range[32].
- The applied ***VHF plasma excitation power***: by increasing the power one can also increase the deposition rate as well as shift the transition from a-Si:H to μc-Si:H to higher $c(SiH_4)$- values [33]. We suppose to have a better dissociation of SiH_4 at high power, so as a higher partial pressure of free silane radicals can be obtained in the plasma bulk, e.g. a higher SiH_4 concentration is possible for the transition. However, higher plasma excitation power generally results in stronger ion-bombardment and in defective material, i.e. in a drop in solar cell efficiency, as will also be shown later in the present work. The power used for the deposition of the samples studied in this work was in the range 5 - 200 W (0.04 – 1.5 W/cm^2).
- The ***temperature***: An important impact of PECVD is its ability for growth of μc-Si:H at relatively low substrate temperatures. All the μc-Si:H samples of the present work (layers and solar cells) were deposited at a temperature (of the heater) of around 200°C (see Annex C).

All the samples characterised in this work were deposited on plain and LP-CVD ZnO-coated AF45 (Schott) glass substrates. To obtain nearly intrinsic μc-Si:H material, a gas purifier was used [34].

1.3. Characterisation techniques

In this work, the microstructure of μc-Si:H was mostly monitored by **Raman spectroscopy** (chapters 2.1 & 2.2). As will be introduced in chapter 1.3.1, Raman spectroscopy is a fast and non-destructive characterisation technique that is applicable to layers as well as to entire (functioning) solar cells. Moreover, it allows a depth profiling of the crystallinity of the top and bottom parts of the thin-film layer.

The development of device-grade μc-Si:H layers, however, not only demanded to have an idea of their microstructure, but also of their semiconductor characteristics. The latter were determined (on a selected choice of layers on glass) by dark-current measurements (explained in chapter 1.3.2), in order to determine the dark-current conductivity σ_{dark} and its activation energy E_{act}. The sub band-gap absorption, which is a measure for the defect density in intrinsic layers deposited on glass, was determined by ***PDS (Photothermal Deflection Spectroscopy)***, by ***Constant Photocurrent Measurement*** (***CPM***, explained in chapter 1.3.5).

Finally, μc-Si:H solar cells were characterised electrically by illuminated current-voltage measurements (explained in chapter 1.3.3) and external quantum efficiency measurement (explained in chapter 1.3.4). The sub band-gap absorption characteristics of the intrinsic layer in a solar cell were also obtained by ***Fourier-Transform Photocurrent Spectroscopy*** (explained in chapter 1.3.5).

An illustrative way to study the microstructure of μc-Si:H samples is ***Transmission Electron Microscopy (TEM)***, explained in chapter 1.3.6. This technique enables a direct imaging of the microstructure of layers. We applied it in the case of solar cells (chapter 3.3).

Secondary Ion Mass Spectrometry, an analysis method to determine atomic contamination and their profile within layers, is explained in chapter 1.3.7. This characterisation technique was needed to analyse doping profiles of μc-Si:H solar cells; these profiles were a crucial issue for the present work.

1.3.1. Micro-Raman Spectroscopy

Micro-Raman Spectroscopy is used to monitor the crystallinity of μc-Si:H layers and solar cells. Hereby, "bifacial depth-dependent" micro-Raman spectroscopy was applied to our samples, to measure their so called "Raman crystallinity factor" ϕ_c [35]. This factor – not to be confused with the crystalline volume fraction - is calculated by evaluating the scattered intensity ratio of the respective Raman peaks assigned to the amorphous and to the crystalline phases.

This powerful analytical technique is based on the analysis of the inelastic scattering of light interacting with the material under test. Raman spectroscopy provides spectra characteristic of molecular vibrations (or of phonons in solids) that can be used for sample identification and/or phase quantification. A Raman spectrum represents the intensity of the scattered light as a function of the shift in frequency (i.e. energy) from the excitation light frequency. This "Raman shift" is directly linked to the vibrational energy of the bonds between the atoms within the probed material. More specifically, in the case of silicon thin-films, Raman spectroscopy is particularly well suited to discriminate between the amorphous phase and the crystalline phase. Therefore, this analysis technique ***allows to quantify the degree of crystallinity of microcrystalline silicon (μc-Si:H) samples***.

Micro-Raman spectroscopy (or Raman microscopy) refers to the kind of apparatus used. Here, the excitation light is guided and focused on the sample via a microscope, and the backscattered Raman signal is also collected via the microscope.

Moreover, Raman spectroscopy is not only applicable to simple layers, but can also be performed on entire silicon thin-film solar cells [35-38].

In this work we have used bifacial depth-dependent micro-Raman measurements, i.e. we are illuminating the sample first from the top and then from the bottom side.

The Raman signal collected in the micro-Raman experiment is equal to the integral, taken over the excited volume of the depth distribution of each phase [39]. Moreover, the volume probed in Raman experiments depends on the absorption coefficient α of the sample at the excitation wavelength used for the measurement. The excited volume depends on the penetration depth ($= 1/\alpha$) of the laser light used. The penetration depth at 514 nm is of the order of 100 nm for a-Si:H and of 300 nm for μc-Si:H, whereas at 633 nm it reaches about 1 μm for both materials. However, in our experimental backscattering set-up, the collected Raman light is scattered from half of these depths [39] [40]. Indeed, we must consider the optical attenuation of the excitation light and the optical attenuation of the Raman scattered light (i.e. two optical paths in the material). Therefore, the Raman Collection Depth (RCD) for our experimental set-up working in backscattering configuration is here defined as:

$$\mathbf{RCD = 1/(2\alpha)}\ , \qquad \text{Equ. 1.5}$$

where α is the absorption coefficient of the probed material at the considered wavelength. The typical values of RCD for a-Si:H, μc-Si:H and c-Si materials and for both 514 nm and 633 nm excitation lights are given in Table 1.1. Whereas RCD is similar for a-Si:H and μc-Si:H at 633 nm, the value of RCD at 514 nm for a-Si:H is about one third of the corresponding value for μc-Si:H. One should keep in mind that the volume probed with the HeNe laser ($\lambda = 633$ nm) contains the volume probed with the Ar laser ($\lambda = 514$ nm) plus an additional

deeper volume.

The collected Raman signal in the micro-Raman experiment is scattered from a depth which equals the Raman Collection Depth (RCD, Equ. 1.5). This depth depends on the layer's absorption coefficient α and on the Laser frequency, as shown in Table 1.1. The absorption coefficients α given in Table 1.1 are typical values for a-Si:H, μc-Si:H and c-Si materials [41] at these two wavelengths.

514 nm (2.41 eV)	α [cm^{-1}]	RCD = 1/(2α)
a-Si:H	~10^5	**50 nm**
μc-Si:H	~3-4·10^4	**120-170 nm**
c-Si	~10^4	500 nm

633 nm (1.96 eV)	α [cm^{-1}]	RCD = 1/(2α)
a-Si:H	~10^4	**500 nm**
μc-Si:H	~10^4	**500 nm**
c-Si	~3-4·10^3	1.2-1.7 μm

Table 1.1: Typical absorption coefficients (α) and Raman collection depths (RCD) for a-Si:H, μc-Si:H and c-Si materials at the wavelengths of 514 nm (left) and 633 nm(right).

The enormous differences in the Raman collection depth between c-Si and μc- or a- Si:H depends on the internal scattering in the μc- and a- Si:H layers. This is also shown in Fig. 1.8 by the different absorption intensities of c-Si, μc- and a- Si:H for varied energy, especially above 1.8 eV.

Evaluation of the Raman crystallinity volume fraction

In Raman spectroscopy, the crystalline volume fraction (X_c) of a sample is defined as:

$$X_c = V_c / V_{exp} \ , \qquad \text{Equ. 1.6}$$

where V_c is the crystalline volume and V_{exp} is the total scattering volume in the Raman experiment for a mixed phase material (i.e. $V_{exp} = V_a + V_c$, with V_a the amorphous volume). Due to a correlation between scattering volume and the integrated Raman scattered intensities [42] the crystalline volume fraction of equation 1.6 can also expressed in the following manner:

$$X_c = I_c / (I_c + y \cdot I_a) \ , \qquad \text{Equ. 1.7}$$

where y is defined as the ratio of the integrated Raman cross-sections [43]:

Whereas I_c and I_a can be directly measured from the Raman spectra, the value of y is a matter of debate. Values of y from *0.88* [43] down to *0.1* [44] have been published. Furthermore, y depends on the size of the crystallites (δ) and on the excitation wavelength [42].

Because of complexity of determining the "real" crystalline volume fraction – it is not a quick check laboratory method-, a novel more simplified *"Raman crystallinity factor"* ϕ_c was

introduced for the Raman crystallinity by C. Droz et al. [45].

This factor does not reflect the actual crystalline volume fraction (it corresponds to the case where one arbitrarily sets y = 1), but is simply a ratio of Raman intensities that is expressed as:

$$\phi_c = I_c/(I_c + I_a) \ . \qquad \text{Equ. 1.8}$$

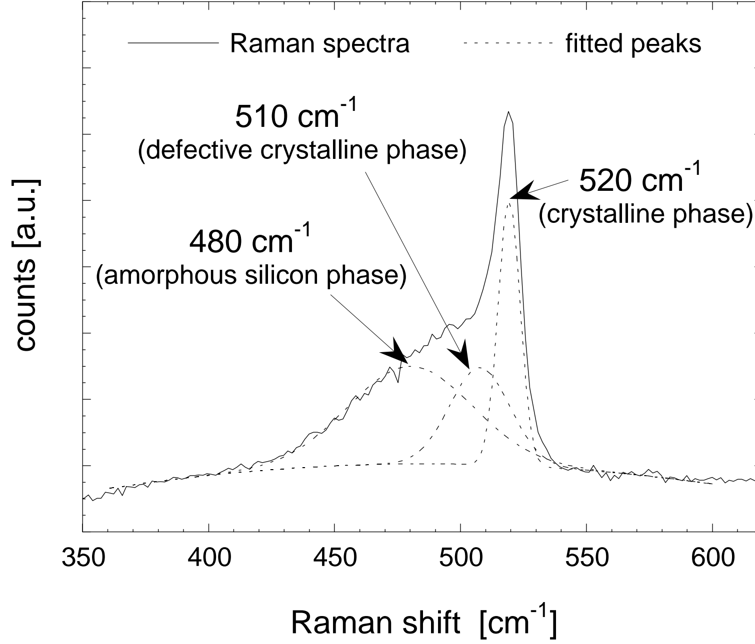

Fig. 1.6: Deconvolution of the Raman spectrum of a μc-Si:H sample into three contributions: The peak centred around 520 cm^{-1} corresponds to the crystalline phase, the peak centred around 510 cm^{-1} corresponds to the defective crystalline phase and the peak centred at 480 cm^{-1} corresponds to the amorphous phase. The three contributions are assumed to be Gaussian peaks.

In practice, ϕ_c is evaluated from the deconvoluted Raman spectra as the ratio of the area of the peak(s) related to the crystalline parts over the total area of the silicon-related peaks. The Raman spectra of our μc-*Si*:H layers or solar cells are fitted with three contributions. The 510 cm^{-1} peak, attributed to the defective part of the crystalline phase, has to be included in the crystalline part. Therefore the Raman crystallinity factor will be calculated as follows:

$$\phi_c = I_{(\mu)c}/(I_{(\mu)c} + I_a) = (I_{520} + I_{510})/(I_{520} + I_{510} + I_{480}) \ , \qquad \text{Equ. 1.9}$$

where I_i is the *area* under the Gaussian centred at i and $I_{520} + I_{510} + I_{480}$ is the total integrated intensity, as shown in Fig. 1.6 below.

This holds for Raman spectra of highly microcrystalline samples as well as for those of samples near the transition [45].*Note that the Φ_c-value underestimates the crystalline fraction, e.g. we have microcrystalline material for Φ_c> 0.3 already[45].*

1.3.2. Electrical dark-current conductivity (σ_{dark})

The dark conductivity (σ_{dark}) is the conductivity measured without illumination. It is defined as the constant of proportionality between the current density (J) and the electrical field (E), and is expressed as:

$$J = \sigma_{dark} \cdot E \qquad \text{Equ. 1.10}$$

Microscopically, in the framework of the classical transport model [46], σ_{dark} can be expressed as a product of the band mobilities of the electron and holes, respectively, with the density of the free electron and the free holes.

The measurement of σ_{dark} as a function of the temperature (T) gives us access to the activation energy (E_{act}), as they are linked by the relation:

$$\sigma_{dark}(T) = \sigma_0 \cdot \exp(-E_{act}/kT) \ , \qquad \text{Equ. 1.11}$$

where k is the Boltzmann constant and σ_0 the dark conductivity pre-factor [46].

For measurement of conductivity, two evaporated ohmic aluminium-contacts were needed. The sample was placed on a heating plate in a dark chamber, A nitrogen atmosphere of 10 mbar allows a homogeneous heating of the sample while limiting possible oxidation of the layer. The computer-controlled measurement of $\sigma_{dark}(T)$ consists of three steps: first, the sample is rapidly heated up to 180°C (i.e. 10- 20°C less than the deposition temperature of the sample); then the temperature is kept constant for 90 minutes ("annealing" step, e.g. contact becomes ohmic if it is not yet); and finally a controlled decreasing temperature ramp is applied to the sample. During this last step, one measures the current (I) while applying a voltage (U) between the two metallic electrodes. σ_{dark} is then calculated as follows, taking into account the contact geometry:

$$\sigma_{dark} = \frac{g}{l \cdot d} \cdot \frac{I}{U} \ , \qquad \text{Equ. 1.12}$$

where g is the gap between the electrodes, l is their length, and d is the sample thickness that was typically 2 µm for the µc-Si:H samples and 1 µm for the a-Si:H samples. Note that the values for σ_{dark} given hereafter are those measured at room temperature (T = 300K).

1.3.3. Illuminated current-voltage characteristics (JV-measurement)

The basic characterisation tool for a solar cell is the current-voltage (JV) measurement. It is performed under a solar simulator (double light source Wacom WXS-140S) that produces a

light with an intensity of 100 mW/cm^2 and a spectrum close to the AM1.5 solar spectrum (average illumination on earth produced at sunlight incidence of 48º). Fig. 1.7 shows a typical J(V) curve measured on a good µc-Si:H solar cell ($V_{oc} = 520$ mV, $J_{sc} = 24.2$ mA/cm^2, $FF = 73\%$, [47]).

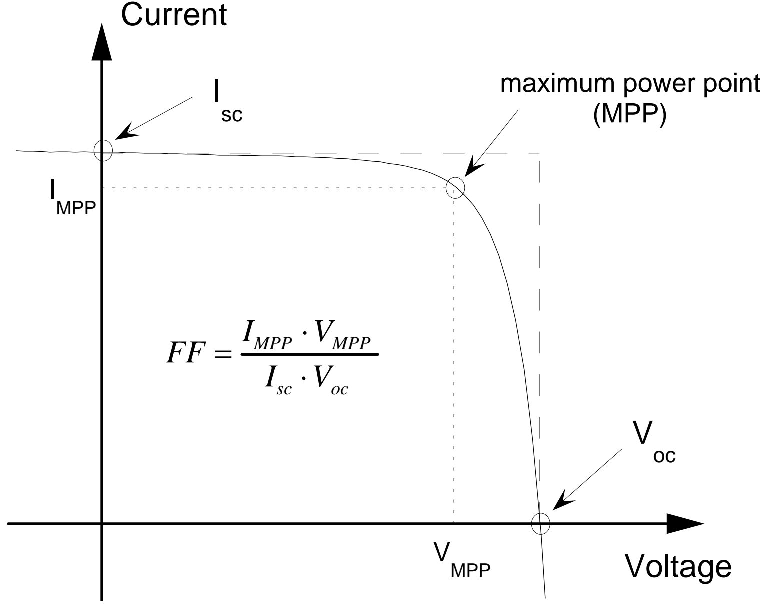

Fig. 1.7: Typical current-voltage (JV) curve of a µc-Si:H solar cell under illumination. The open-circuit voltage (V_{oc}) and the short-circuit current (J_{sc}) are indicated. The fill factor (FF) is defined as the ratio of the area of the rectangle formed by the current and voltage obtained when the power is maximal and the area of the rectangle formed by I_{sc} and V_{oc}.

The ***open-circuit voltage V_{oc}*** is the voltage measured on the solar cell when no current flows through the device (I = 0). Similarly, the ***short-circuit current I_{sc}*** is the current flowing through the cell when the voltage is zero (V = 0). The ***Fill Factor FF*** is defined as:

$$FF = \frac{J_{MPP} \cdot V_{MPP}}{J_{sc} \cdot V_{oc}}$$ Equ. 1.13

where J_{MPP} and V_{MPP} are, respectively, the current and the voltage obtained when the output power is maximum (maximum power point, MPP).

Whereas the values for V_{oc} and FF are evaluated from J(V)-measurements, J_{sc} is usually preferably obtained from quantum efficiency (QE) measurement (see 1.3.4). Indeed, one actually wants to know the current density of a solar cell that can be obtained by measuring the current while precisely evaluated the active area. However, the active area of laboratory test cells was at first not well defined and the estimation of the current density consequently difficult (the introduction of the novel lift off structuring at the end of this thesis leads to reproducible, constant areas). Furthermore, the spectrum provided by a solar simulator is not exactly AM1.5. A difference in the spectrum will affect J_{sc} more noticeably than V_{oc}.

The **efficiency** η of a solar cell is the ratio of the maximal electrical output power and the incident light power (P_{light}):

$$\eta = \frac{J_{MPP} \cdot V_{MPP}}{P_{light}} = \frac{J_{sc} \cdot V_{oc} \cdot FF}{P_{light}} \qquad \text{Equ. 1.14}$$

If the measurement of J_{sc}, V_{oc} and FF is performed under standard AM1.5 conditions, then P_{light} = 100 mW/cm^2 (= 1000 W/m^2).

1.3.4. External quantum efficiency

The ***external quantum efficiency*** (***EQE***) is the measurement of the number of electrons extracted from the device per incident photon of a given energy. Experimentally, the solar cell is illuminated with a chopped light beam from a monochromator. The cell current density $i(E_{photon})$ is measured and divided by the incident flux of photons $\phi(E_{photon})$ determined with a reference detector, whose quantum efficiency is known.

$$EQE = \frac{i(E_{photon})}{q \times \phi(E_{photon})} \qquad \text{Equ 1.15}$$

EQE measurements can be performed under a voltage bias in order to superimpose an external electric field onto the internal field of the solar cell:

In reverse bias, the collection of the generated carriers increases (losses by recombination decreases). For a sufficiently high reverse bias, recombination losses become negligible and all photo-generated electron-hole pairs are collected. By comparing the EQE curves with and without the reverse bias, one can therefore diagnose collection problems within a cell.

External quantum efficiency is used in forward bias, to evaluate the cell close to its working conditions (i.e. close to the maximum power point).

EQE measurements can also be used to evaluate the short circuit current density J_{sc} of the solar cells by integration (over the photon energy) of the product of EQE with the photon flux of AM1.5 spectrum. This method is a more precise method to determine J_{sc} than J(V) under a sun simulator, in all cases where the solar cell area cannot be precisely measured.

The EQE curve of a μc-Si:H solar cell shows an spectral absorption up to wavelengths (λ) of about 1100 nm. Note that a good μc-Si:H solar cell typically has a $EQE_{@800nm} \geq 0.3$ (at λ= 800 nm).

The values of J_{sc} given in this work have been obtained with this method (via EQE measurements).

1.3.5. Measurement of the sub-gap absorption coefficient

In order to use the absorption spectroscopy routinely to monitor the quality of the i-layer in working devices, M. Vanecek et al. developed a fast and sensitive technique based on Fourier-transform infrared (FTIR) spectroscopy [48, 49]. This new technique**,** named ***Fourier-transform photocurrent spectroscopy (FTPS)*** provides measurements of the absorbance spectrum of silicon-based thin-films over 6 orders of magnitude, in the sub band-gap region as well as above it. It only ***takes a few minutes*** as ***compared to*** several hours for the ***traditional techniques*** of ***PDS*** and ***CPM*** used so far for evaluating sub band-gap absorption (see below).

Sub band-gap absorption α is commonly measured with very sensitive techniques like Photo Deflection Spectroscopy (PDS), Constant Photocurrent Measurement (CPM) and ***Fourier-Transform Photo Spectroscopy*** (FTPS). The absorbance spectrum of interest extends roughly from 0.7 eV to 2 eV. In addition to the measurement of the optical band-gap, the absorption spectrum yields two important parameters related to the ***disorder*** and the ***defect density of the probed material***. These parameters are related to the gap states that are undesirable for solar cell applications. Indeed, if there are states in the centre of the gaps, they act as recombination centres, thereby limiting the electrical performances.

In the region just below the gap (1.12 eV for μc-Si:H and 1.75 eV for a-Si:H), the absorption coefficient (and the FTPS spectrum) stems from optical transitions involving band tail states. The spectrum in that region increases exponentially with the photon energy, forming the so-called Urbach tail. It is characterized by the exponential slope E_{Urbach} of the absorption spectrum. It is determined by fitting the absorption curve using the following formula:

$$\alpha = \alpha_0 \cdot e^{E/E_{Urbach}} \qquad \text{Equ. 1.16}$$

where α_0 is the exponential pre-factor.

In microcrystalline silicon the Urbach tail before the bend edge extends from 1.12 eV. The slope at that edge is described by the so called E_{Urbach} , e.g. 36 to 40 meV [50] are measured for device grade μc-Si:H material. ***E_{Urbach}*** can be ***related to the material disorder***. Note that the Urbach tail also exists in monocrystalline silicon (a typical value of 9.6 meV was reported [51] for room temperature measurements), although it does not originate here from material disorder.

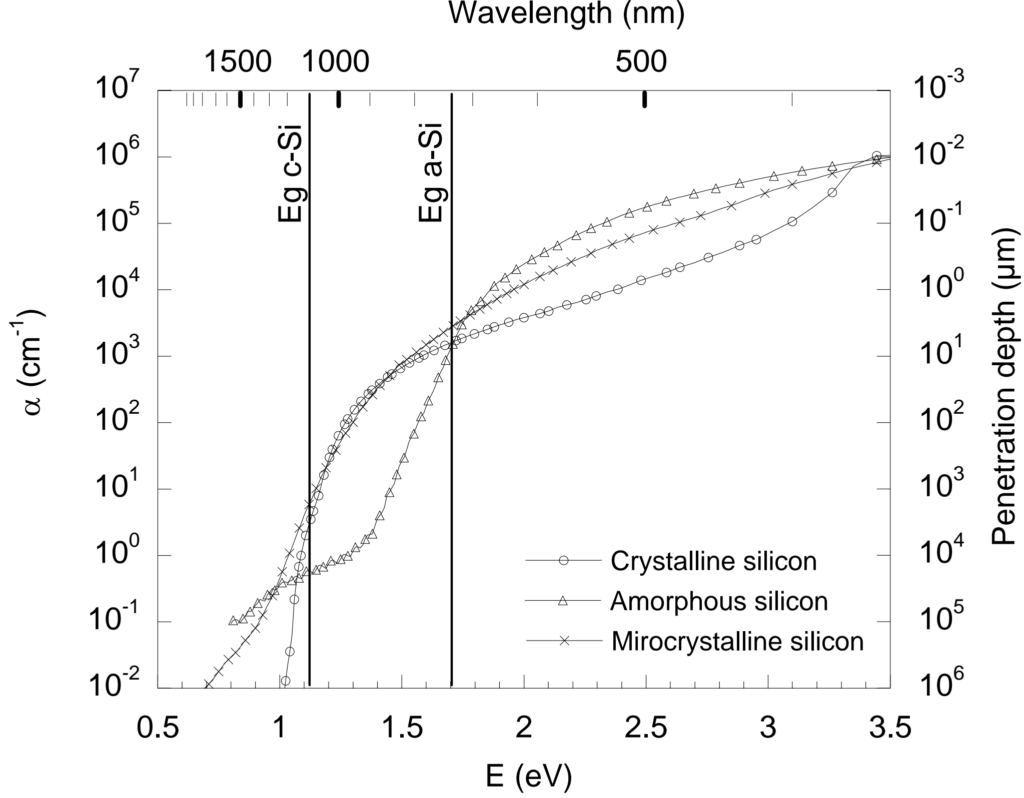

Figure 1.8: Absorption spectra of microcrystalline, amorphous and crystalline silicon measured by CPM reproduced from ref. [52]. The penetration depth, i.e. the inverse of the absorption coefficient α, is plotted on the right axis.

The ***defect densi***ty is estimated from the value of ***the absorption coefficient at a photon energy of 0.8 eV*** for µc-Si:H silicon ($\alpha_{0.8eV}$).

PDS and CPM are time consuming techniques. Besides this common disadvantage, the PDS method cannot be used for the evaluation of the sub band-gap absorption in complete solar cells. Indeed, from a photon energy of 1.6 eV and below, PDS measures the free carrier absorption of the transparent conductive oxide TCO (contact material), which is several orders of magnitude larger than the absorption α of silicon in that spectral region. The Urbach parameter E_{Urbach} and the defect related absorption thus cannot be measured by PDS in a complete solar cell configuration.

On the other hand, CPM allows the measurement in complete cells, as it is based only on the number of photons required for each photon energy to keep the photocurrent constant. Because the photocurrent is generated in the i-layer only, CPM can be used to monitor the electronic properties of the i-layer within a complete solar cell. The sensitivity of this technique in the spectral region of very low absorption (around or below 0.8 eV) is technically limited, however, and the regulation step at each photon energy value is time consuming.

1.3.6. Microstructure characterisation by Transmission electron microscopy (TEM)

TEM is the method that enables us to obtain a direct picture of the microstructure of the layers constituting the cells: metallic contacts, TCOs, n-, i- and p-layers. TEM, thus, reveals the complexity of the layers and the inhomogeneities in thickness (although the resolution for detecting amorphous material is limited here).

This unique feature, however, has its price: it is a time consuming and a destructive technique. The technique used here for sample preparation was introduced by Benedict et al. [53]. For a complete introduction to the TEM techniques, see for instance ref. [54]. In this work, we used the "tripod method" [53, 55]: Two pieces of the sample are glued head to head to obtain a "sandwich" (with the layers in the centre and the glass substrate on each side). Then, with the help of a small instrument with three micrometrical feet called a "tripod", the sandwich is mechanically polished to obtain a corner with an angle of about 0.6 to 0.8°. At that edge, the sample becomes thin enough (less than 100 nm thick) to allow transmission of the electrons. Finally, a short ion-milling procedure is used for sample cleaning. The samples have been measured in our case with a Philips CM200 microscope operated at 200 kV.

1.3.7. Secondary Ion Mass Spectrometry (SIMS)-Analysis

Secondary Ion Mass Spectroscopy (SIMS) is a useful analysis instrument to ***detect very low atomic concentrations down to the order of*** 10^{16-17} ***atoms/*** cm^3 (equal ~ 0.1 ppm). In our case it is used to detect boron contamination in the intrinsic layer within a p-i interface deposited on a wafer. For this measurement, the sandwich structure was bombarded with primary Cs^+ and O_2^+ ions at near-normal incidence accelerated with an energy of 6 keV. The electron beam bombardment has been used for charge compensation during the O_2^+ bombardment. The residual gas pressure in the SIMS analysis chamber was $< 2 \times 10^{-10}$ torr. Secondary Ion Mass Spectrometry (SIMS) depth profile analysis was performed using a quadrupole instrument (Atomika 4000). A stylus surface step profile-meter (Dektak 6M) was used to measure the sputtered crater depths. These measurements could be carried out thanks to collaboration with “Institut für Photovoltaik, Forschungszentrum GmbH, Jülich” (Germany).

Outline of this work

Besides this introduction, the present thesis is divided into three main subjects:

- The **first subject** (Chapter 2) deals with the development of μc-Si:H layers for μc-Si:H solar cells. Hereby, we focussed on one hand on the development of microcrystalline, sufficiently conductive ($\sigma_{dark} \approx 10^0$ S/cm), thin ($\leq$ 30nm), trimethylboron (TMB) p-doped Si:H layers and on the other hand on the development of high-rate deposited μc-Si:H layers in or near the high-pressure regime. The whole development is done on plain substrates and on glass substrates coated with LP-CVD ZnO layers. The characterisation of the Si:H layers was mainly done by Micro-Raman spectroscopy and partially by dark-current measurements.
- The **second subject** (Chapter 3) focuses on the deposition of μc-Si:H solar cells on "IMT-state-of-the-art" LP-CVD ZnO in a single-chamber PECVD deposition system. Herein, the influence of various chamber treatments after the deposition of the p-doped Si:H layer is studied by their effect on μc-Si:H solar cell electrical performances and by FTPS performed on the full solar cells in order to evaluate the defect density and the disorder (due to the band tail states) within the i-layer. SIMS-measurements of p-i interface samples were used to investigate boron cross-contamination and the impact of various chamber treatments. In a further approach, intrinsic, high-rate deposited μc-Si:H layers of a pressure series that extends into the high-pressure regime are studied.
- The **third subject** (Chapter 4) is devoted to the uniformity of the thickness of deposited layers and deals with plasma confinement box design. It resulted in the introduction of a novel cylindrical plasma confinement box; it is, thereby, indirectly related to the study of the high-rate deposited μc-Si:H layer in the high-pressure regime.

Chapter 2: Development of μc-Si:H layers and special treatments

2.1. p-doped μc-Si:H layers with Trimethylboron (TMB) instead of diborane (B_2H_6) as doping gas

2.1.1. Introduction

The "state-of-the-art" microcrystalline p-doped layers used up to now at IMT were based on diborane doping gas [56]. This study focuses on the development of microcrystalline p-doped layers using the alternative doping gas trimethylboron (TMB) in order to replace diborane.

The choice for the source doping gas ***TMB*** was taken because of its ***higher thermal stability***, i.e. self-decomposition of TMB (without plasma) does not exist under the given conditions in our laboratory (whereas diborane does manifest self-decomposition even without plasma). The idea was to reduce or even suppress the temperature induced (T≈ 200°C) contamination of the system equipment by boron.

In order to evaluate the development of "good" microcrystalline TMB p-doped Si:H layers, the following minimal requirements were defined – based on the experience in our laboratory with p-doped layers on plain glass, on ZnO-coated substrates and also on layers incorporated in p-i-n solar cell devices:

A p-doped μc-Si:H layer can be considered to be "good", if its Raman crystallinity factor ϕ_c is ≥ 0.5 (on ZnO) and the corresponding σ_{dark} conductivity at RT (on glass) is above 1 S/cm for a thickness of ~20- 30 nm. In practice, even thinner μc-Si:H p-doped window layers are used within solar cells, due to the need for high transparency.

Focussing on the importance of the parameters of the optimisation series, the ***plasma excitation frequency*** was seen to be ***a very important parameter for achieving high doping levels of μc-Si:H layers*** – higher frequency values are definitely advantageous. Furthermore,

the ***concentration of TMB/SiH₄*** has turned out to be a ***critical parameter for obtaining high Raman crystallinity factors ϕ_c (≥ 0.5)***. A well tuning of the TMB-concentration level is, therefore, a must, so as the TMB-concentration is neither too high – this increases the amorphous volume fraction - nor too low – this leads to an insufficient electrical conductivity σ_{dark}.

The reason of the change to TMB:

Diborane is known to be a doping gas of several critical issues.

The main problem of B_2H_6 is its low thermal stability (decomposition energy of only 164 kJ/ mol). Furthermore, the source-gas B_2H_6 as well underlies self-decomposition within the gas bottle, leading to the formation of molecules with higher boron coordination, during storage, that appear as powder.

Diborane B_2H_6 underlies a reversible equilibrium (Equ. 2.1) that shows a decomposition to boron as well as the reverse reaction, under the applied working conditions (T_{heater}= 200°C).

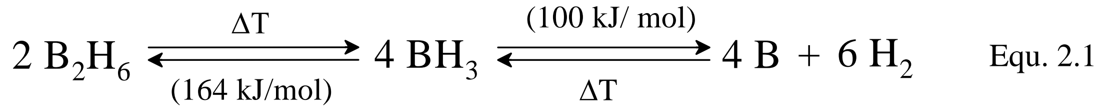

$$2\,B_2H_6 \underset{(164\ \mathrm{kJ/mol})}{\overset{\Delta T}{\rightleftarrows}} 4\,BH_3 \underset{\Delta T}{\overset{(100\ \mathrm{kJ/\ mol})}{\rightleftarrows}} 4\,B + 6\,H_2 \qquad \text{Equ. 2.1}$$

The chemical thermolysis reaction of B_2H_6 to BH_3 is initiated at elevated pressure and temperatures (>300 °C without plasma) and then keeps on reacting directly to boron (B) and hydrogen (H_2) [57]. The back reaction needs as well an initiation energy (100 kJ/mol) which can be supplied by the plasma. Thermally initiated boron contamination – even without any plasma - has to be presumed at all hot spots (> 100 °C) in the system.

In a single-chamber PECVD reactor, recycling of impurities was reported - in our case boron - which remains on the covered chamber walls and subsequently takes place during the deposition of an intrinsic Si:H layer [58].

Therefore, a strong cross-contamination into a subsequently grown intrinsic layer had to be presumed after a previous deposition of a p-doped layer.

TMB has a higher thermal stability and was, therefore, suspected to have a much weaker impact in cross-contamination. Nevertheless, TMB was as well reported to cause cross-contamination [59].

There are many possibilities of physical as well as chemical manner to cause cross-contamination. As follows, we introduce two possibilities.

Physical "sputtering" by a hydrogen plasma is known to etch silicon layers including incorporated boron [60] which then may be recycled into the subsequently grown

intrinsic layer.

Due to the presence of hydrogen on the other hand *the reverse chemical reaction* (Equ. 2.1) may occur for boron atoms that are trapped on the walls or on the surface of the device (p-layer). In this assumption diborane or even only BH_3 only act as boron intermediate carrier of the boron atoms.

Enhanced hydrogen dilution during the deposition of the intrinsic μc-Si:H layer was as well observed to increase boron contamination.

However, we do not know what kind of mechanism exactly ***causes cross-contamination of boron***. We only observed boron contamination as shown in chapter 3.2 by SIMS-Analysis.

Due to the higher thermal stability of the TMB ($B(CH_3)_3$) molecule, B_2H_6 has been replaced in our work as p-doping gas. TMB does not decompose into elementary boron, in hot zones without plasma contact as in the heated part of the gas-inlet and at the gas showerhead, However, B_2H_6 decomposes in hot zones. Therefore, TMB reduces the risk of boron contamination is in hot zones. In the bulk plasma, however, TMB is decomposed.

In order to achieve silicon layers conductivities of 1- 5 S/cm at room temperature (RT) as obtained by using B_2H_6 as doping gas source [56], we had to double the TMB doping gas concentration in the bulk plasma compared to what had been required for B_2H_6. Indeed, in the case of TMB, there is only one boron atom per molecule, while B_2H_6 has two boron atoms. Furthermore, the presence of boron atoms in a layer reduces the tendency of crystalline growth. The supplementary carbon atoms (3 per TMB molecule) here further decrease the tendency of crystalline growth, favouring amorphous growth.

In order to fabricate p-layers as conductive as possible, it is desirable to obtain highly crystalline p-doped Si:H layers. If the Raman crystallinity factor ϕ_c of the p-layer is too low, i.e. if the p-layer is too amorphous, this leads to a loss in V_{OC} because of the reduced shift in Fermi-level in such layers, and also to the promotion of subsequent growth of an unsatisfactory intrinsic Si:H layer. The p-i-n solar cells can also show poor J(V) characteristics because of a barrier that is formed between the underlying n-type ZnO layer and an insufficiently doped p-layer. [61]. Furthermore, these p-doped window layers need to be of high transparency. It is towards achievement of these goals that this study of TMB p-doped μc-Si:H films has been conducted.

The fact that the development of the p-doped layer has to be done with the same electrode configuration – all the work is done in a single-chamber system - as for the one used for the high-pressure intrinsic layers complicates this work. The electrode configuration for the high-pressure regime demanded several modifications (see chapter 4), to which the p-doped layer always had to be readapted. This demanded additional work.

There are several possibilities to achieve highly microcrystalline p-doped Si:H layers. The easiest way to control microcrystalline crystallisation is by a carefully control of the TMB/SiH_4 concentration; this investigation was historically the first point of this study, it was first undertaken for an excitation frequency of 70.0 MHz (see Fig. 2.4). Initially the development was made using a source-gas bottle of too high TMB concentration of 2 % TMB diluted in H_2. There were further limitations with respect to the flow controllers. All this led to insufficiently crystalline ($\phi_c < 0.3$) and insufficiently conductive ($\sigma_{dark} < 10^{-3}$ S/cm) p-doped Si:H layers. Finally, we changed the TMB-source-gas bottle from 2 % to a concentration of 500 ppm TMB (factor 40 lower bottle concentration).

Due to these initial limitations, three more complicated methods to achieve microcrystalline silicon layers were also studied (see 2.1.3). The first is H_2-recrystallisation of an amorphous p-doped layer, the second the introduction of an intrinsic microcrystalline nucleation layer and, finally, a simple pre-deposition plasma applied to the underlying LP-CVD ZnO layer, a plasma of either H_2 or CO_2.

2.1.2. Development of p-doped microcrystalline Si:H layers with Trimethylboron (TMB)

The growth of trimethylboron (TMB) doped microcrystalline Si:H p-layers at very high plasma excitation frequencies (VHF) was studied based on an earlier work [62].

Deposition parameters for microcrystalline TMB doped layers, similar to these published in the above mentioned study, were applied. In the series (using a 500 ppm TMB source-gas concentration) we focused on the following deposition parameters: TMB/SiH_4 concentration, hydrogen dilution, VHF-plasma excitation power and plasma excitation frequency. The p-doped layer material quality parameters monitored first were the Raman crystallinity factor ϕ_c (LPCVD ZnO-coated substrates) and the dark conductivity σ_{dark} (plain glass substrates).

Finally, after having resolved the issue of the minimal gas phase doping concentration –by installation of a TMB source-gas bottle with reduced concentration (500 ppm compared to 2 %TMB in H_2)-, ***highly microcrystalline p-doped Si:H layers*** with ***Raman crystallinity factor*** ϕ_c ***of ~0.7*** (on LPCVD ZnO-coated substrates), and ***dark conductivities*** (on plain glass substrates) ***of up to*** $\sigma_{dark} \approx 2$ ***S/ cm*** were obtained.

The ***plasma excitation frequency proved to be the key parameter to obtain a high Raman crystallinity factor*** ϕ_c ***and high value of dark conductivity***. The best characteristics were only obtained at 110 MHz, but not at 70.0 MHz. At 110.0 MHz the doping level was significantly increased compared to 70.0 MHz. This is shown by the high values obtained in the σ_{dark}

measurements. Thereby, correspondingly high values of ϕ_c were obtained.

<u>*Experimental:*</u>

The TMB p-doped layers were examined with respect to their electrical and structural properties in order to attain reasonable values for layers with a thickness ranging from 20 to 30 nm, as measured by mechanical step profile-meter on the plain glass substrate. The development was done for an electrode gap distance d_{gap} of 9.5 mm. In the beginning, the p-layers were developed at a plasma excitation frequency of 70.0 MHz which initially was used for intrinsic μc-Si:H layers on this system. The idea was to develop a deposition process for the microcrystalline solar cell with the same excitation frequency for all Si:H layers, e.g. for the p-doped, the intrinsic, and the n-doped layer.

In a first approach the TMB/SiH_4 concentration series (500 ppm TMB source-gas concentration) of ~20 nm thick p-doped layers was set at the highest possible TMB flow. The first series of Fig. 2.4 was deposited using the following process parameters: ϕ(TMB)= 2-10 sccm (0.1-0.5 % TMB/SiH_4), $\phi(H_2)$= 60 sccm, $\phi(SiH_4)$= 1.0 sccm, p= 0.6 mbar, P= 10 W, f= 70 MHz.

In a next step the plasma excitation power was varied between 10 and 30 W for the same process parameters, and for fixed ϕ(TMB)= 5 sccm (0.23 % TMB/SiH_4).

The so far achieved maximum doping levels of TMB p-doped μc-Si:H at the excitation frequency of 70.0 MHz were far too low. The doping concentration ratio between the fluxes (TMB)/(SiH_4) of 0.25 % could not be increased beyond 0.25 % for μc-Si:H p-layers – higher TMB concentration led to a-Si:H layers. Therefore, the reported [63] crucial impact of higher plasma excitation frequencies favouring microcrystalline growth for p-doped layers frequencies was studied by increasing our plasma excitation frequency to 110.0 MHz. Here, a significant increase in doping concentration (from 5.5 to 20 sccm TMB flow rate, resp. 0.25 to 1.0 % TMB/SiH_4 gas phase doping ratio) could also be realized, obtaining μc-Si:H layers up to 0.75 % TMB/SiH_4.

The PECVD deposition system (volume ≈ 16 litre) used on study was equipped with a roots-pumping system (Q= 4.2 m^3/min.) for process gas pumping.

All depositions were carried out as co-deposition on plain AF45 glass as well as on a LPCVD ZnO-coated glass (IMT standard type: chamber B, process M4, 36 min.).

All the work reported in this chapter 2.1.1 used 500 ppm TMB diluted in H_2. In all experimental series where TMB incoming flow rate was varied, direct inflow of H_2 was also varied, but with the opposite sign, so as to keep total H_2 inflow constant. The flow rates given

here for TMB are total flow rates including H_2 dilution gas.

Results and discussion:

2.1.2.1. Comparison 70.0 vs. 110.0 MHz:

For the present deposition chamber system a very high plasma excitation frequency of 110.0 MHz was needed (Fig. 2.1) to obtain good dark conductivities ($\sigma_{dark} \approx 2.5$ S/cm) values and good Raman crystallinity ($\Phi_c \geq 0.5$) as shown in Fig 2.2.

At 70.0 MHz only very poor doping induced dark conductivities (< 10^{-2} S/cm) were obtained for μc-Si:H layers (see Fig. 2.4). The TMB doping level could no more be increased to higher TMB concentrations for μc-Si:H material, as the material became amorphous.

In order to check if there is a strong change in doping behaviour for even higher excitation frequencies, the plasma excitation frequency was changed from 70.0 MHz to 110.0 MHz.

The comparison of the excitation frequencies was carried out with the deposition parameters (corresponding to the highest possible doping level (5.5 sccm TMB flow rate; TMB/SiH_4 gas phase doping ratio= 0.25 %) at 70.0 MHz for p-doped μc-Si:H material (Fig. 2.4 a).

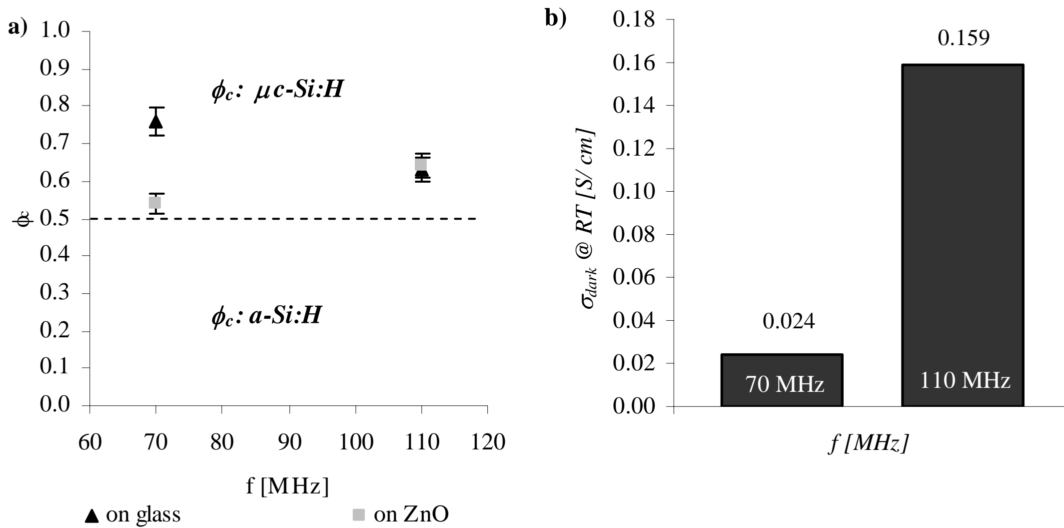

Fig. 2.1: Comparison of the effect of plasma excitation frequencies a) by the Raman crystallinity factor ϕ_c on glass (black) and on ZnO-coated substrate (grey) and b) by electrical conductivity σ_{dark} of p-doped μc-Si:H layer.

The achieved p-layers deposited at 110.0 MHz shown in Figure 2.1 then revealed a surprising increase in Raman crystallinity factor ϕ_c and increased dark conductivity. The increase in

frequency led on one hand to an increase of the ϕ_c-value for the sample on ZnO from ~0.55 to ~0.65 for 70.0 and 110.0 MHz, respectively, whereas the opposite behaviour was observed on layers deposited on plain glass (decrease in ϕ_c from 0.75 to 0.65).

However, the dark conductivity σ_{dark} (on glass) increased from 0.024 S/cm to 0.159 S/cm, conductivity must be further increased up to the order of 10^0 S/cm. The highly μc-Si:H layers (ϕ_c of 0.6- 0.7) allow a further increase in doping gas concentration. That leads to good electrical dark conductivity values as shown in Fig. 2.2.

2.1.2.2. Dilution series of TMB at 110.0 MHz

The favourable impact of the increased excitation frequency at 110.0 MHz to ϕ_c for p-doped μc-Si:H layers facilitates a further increase of the TMB doping concentration without becoming amorphous. In the present series TMB/SiH_4 concentration was increased from 0.25 to 1.0 % as shown in Fig. 2.2. Hereby, σ_{dark} conductivity at RT could be increased above 1 S/cm (layer thicknesses ≈ 25 nm). Furthermore, the total H_2 flow rate was compensated in this series, e.g. as TMB inflow was increased, direct H_2 inflow was correspondingly decreased.

Note that in a p-i-n solar cell structure, the μc-Si:H p-layer not only helps to build up the electrical field. At the same time do its surface characteristics (e.g. crystallinity) strongly influences the subsequent growth of the overlying intrinsic μc-Si:H layer.

If the Raman crystallinity factor ϕ_c of the p-layer is too low, i.e. if the p-layer is too amorphous, this leads to a subsequent growth of an unsatisfactory intrinsic Si:H layer [64]. Therefore, highly crystalline p-doped Si:H layers are necessary for a subsequent growth of a "good" microcrystalline ($\phi_c \geq 0.5$) intrinsic Si:H layer.

Indeed, at the plasma excitation frequency of 110.0 MHz μc-Si:H p-doped layers grown on ZnO, such as those shown in Fig. 2.2 a), exhibit microcrystalline material ($\phi_c \geq 0.5$) up to 0.75 % TMB/SiH_4 concentration. In contrast with this, at 70.0 MHz microcrystalline material was only achieved up to 0.2 % TMB/SiH_4 concentration (see Fig. 2.4 a).

The TMB dilution series in Fig. 2.2 shows microcrystalline material with good ϕ_c-values (≥ 0.5) on ZnO up to the concentration of 0.75 % TMB/ SiH_4 (~10 sccm TMB). However, up to ~1 % TMB/ SiH_4 concentration (~15 sccm TMB) microcrystalline material ($\phi_c \geq 0.5$) was observed on glass with a maximum peak of electrical conductivity σ_{dark} at RT of ~2.6 S/cm at about ~0.75 % TMB/SiH_4 (~15 sccm TMB).

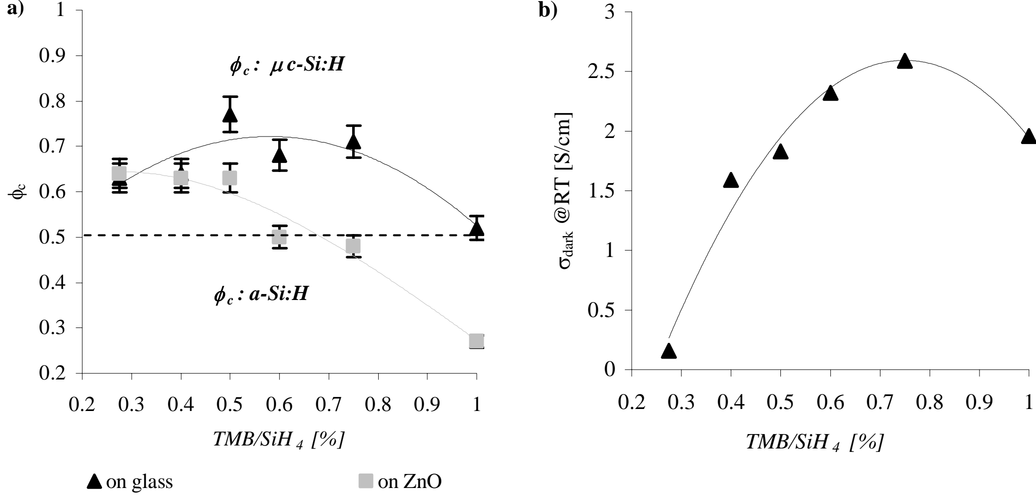

Fig. 2.2: TMB dilution series with its Raman crystallinity factor ϕ_c on glass and ZnO-coated substrates (a) and the corresponding electrical conductivity σ_{dark}–values @RT (on glass) (b) vs. TMB/ SiH_4 concentration, for $f_{exc.}$ = 110.0 MHz.

The resulting p-doped Si:H layers of the present series have sufficient conductivity to be incorporated into p-i-n solar cells.

The best TMB doped μc-Si:H p-layers possessing a dark conductivity at RT of ~2.6 S/cm and a Raman crystallinity factor ϕ_c of about 0.5 were achieved for a concentration of about 0.75 % TMB/SiH_4. This concentration-value is quite consistent with the ideal concentration for B_2H_6 doping gas (~0.4 % B_2H_6/SiH_4) which was reported by R. Flückiger [56], e.g. we need double of the TMB doping gas concentration to obtain similar conductivities as for B_2H_6. Note that TMB as well as B_2H_6 are diluted with H_2 in the source-gas bottle – this dilution was taken into account for the calculations of the doping gas concentration.

2.1.2.3. Hydrogen dilution series

High hydrogen dilution favours the microcrystalline growth of thin-film silicon, e.g. the solar cell performance increases [65].

So far, as shown in the past paragraph, Raman crystallinity factor ϕ_c-values were limited to about 0.5 (on ZnO) for the best σ_{dark} conductivities (on glass the corresponding ϕ_c-value was of 0.7). Here, we will check, if ***increased hydrogen dilution*** can lead to an increasing Raman crystallinity factor for μc-Si:H p-doped layers on ZnO, while retaining a good value for σ_{dark}. So far the H_2 flow rate was limited to 60 sccm. It will now be increased.

Based on the TMB dilution series (Fig. 2.2) the following optimized deposition conditions were chosen: p= 0.6 mbar with gas flow rates of 10 sccm TMB (0.5 % TMB/SiH_4), 1 sccm

SiH_4, at a plasma excitation power of 20 W with a frequency of 110.0 MHz. The H_2 flow rate was varied between 60 and 100 sccm. The TMB/SiH_4 gas phase ratio, however, was fixed at about 0.5 % TMB/SiH_4.

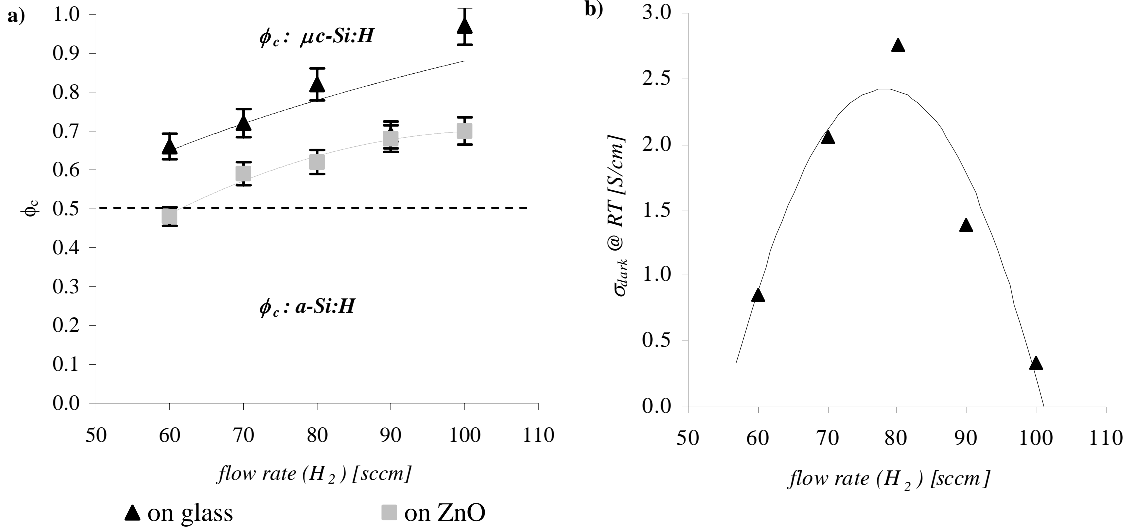

Fig. 2.3: Hydrogen dilution series: (a) Raman crystallinity factor ϕ_c as obtained on glass and ZnO-coated substrates and (b) the corresponding electrical dark-current conductivity (σ_{dark}) –values at RT (on glass) in both cases as a function of H_2 flow rate (The lines are only a guide to the eye).

The increasing hydrogen dilution leads to a linear increase of the Raman crystallinity factor ϕ_c from ~0.65 to ~1 on glass, as well as from ~0.5 to ~0.7 on the ZnO-coated substrates, respectively. Even if ϕ_c continuously increased for higher hydrogen dilutions, uniformity of the Si:H layer thickness became an issue above hydrogen flow rates of 80 sccm. In this dilution range, the p-doped layer – initially about 40 nm thick- was almost absent in the middle of the substrate. The σ_{dark} conductivity data (on plain glass) of the series, however, shows a clear maximum for a hydrogen flow rate of 80 sccm.

As already shown for the hydrogen dilution series in Fig. 2.3, the tendency of obtaining higher Raman crystallinity factors ϕ_c for higher dilution is also confirmed for even higher TMB/SiH_4 concentrations up to 0.75 % on ZnO-coated substrates as well as on plain glass. For p-doped μc-Si:H layers of about 25 nm thickness best σ_{dark} conductivities at RT of about 2 S/cm were achieved for increased TMB/SiH_4 concentrations.

Increased hydrogen dilution is found to be ***helpful to achieve very thin (thickness ≈ 25 nm), fully crystalline p-doped μc-Si:H layers (ϕ_c> 0.5) with good σ_{dark} conductivity (σ_{dark} > 2 S/cm).*** Nevertheless, too high hydrogen dilution causes strong thickness inhomogeneity.

2.1.2.4. Initial concentration series of TMB for 70.0 MHz

The change in plasma excitation frequency 70.0 to 110.0 MHz was the key modification which enabled a significantly increased dark conductivity of TMB p-doped μc-Si:H layers.

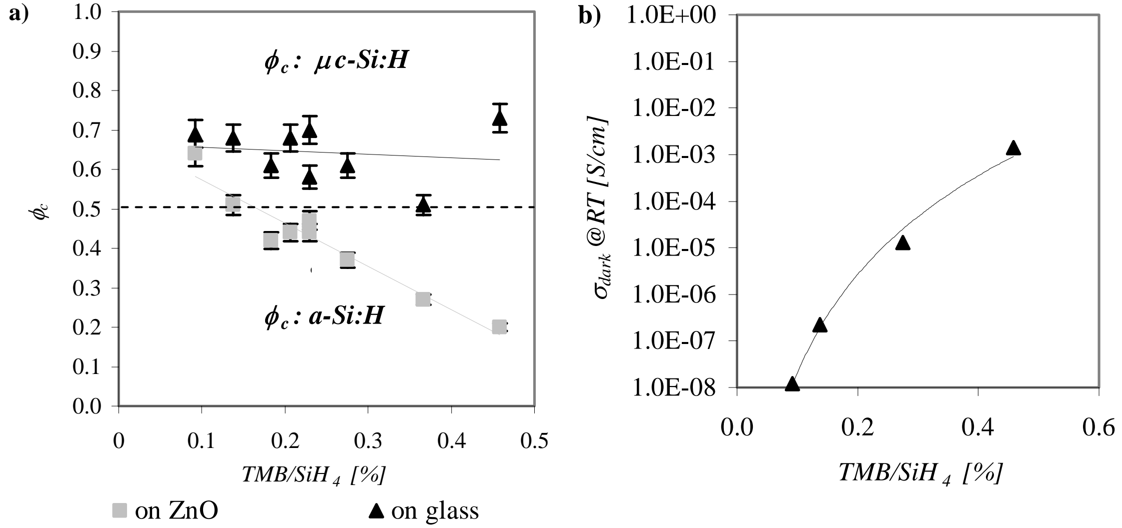

Fig. 2.4: TMB/SiH$_4$ concentration series at 70.0 MHz (a) comparison of ϕ_c-values on plain glass (black) and ZnO (grey), with (b) some corresponding electrical dark conductivity values on glass.

The TMB/SiH$_4$ concentration series in Fig. 2.4 shows the initial issue of TMB p-doping at 70.0 MHz at the beginning of our development of the TMB p-doped μc-Si:H layers (historically seen); indeed, "good" microcrystalline and conductive p-doped layers were, thereby, not been achieved.

The TMB/SiH$_4$ concentration for a p-doped μc-Si:H layer on ZnO could not exceed 0.2 % (Fig. 2.6 a), otherwise the Raman crystallinity factor ϕ_c of the 25 nm thick Si:H layers decreased to 0.2 (almost amorphous layers). The conductivity, thereby, also remained too low ($\leq 10^{-2}$ S/cm).

Enhanced doping by TMB boosted amorphous growth on ZnO, e.g. ϕ_c drastically decreased below a value of 0.5, but σ_{dark} did not increase essentially as shown in Fig. 2.4.

Due to the poor characteristics of the previous TMB/SiH$_4$ concentration series (Fig. 2.4) the impact of plasma excitation power on the μc-Si:H growth was then studied. The plasma excitation power was varied between 10 and 30 W at the frequency of 70.0 MHz for the most reasonable microcrystalline ($\phi_c \approx 0.5$) p-layer of 0.45 % TMB/ SiH$_4$ concentration.

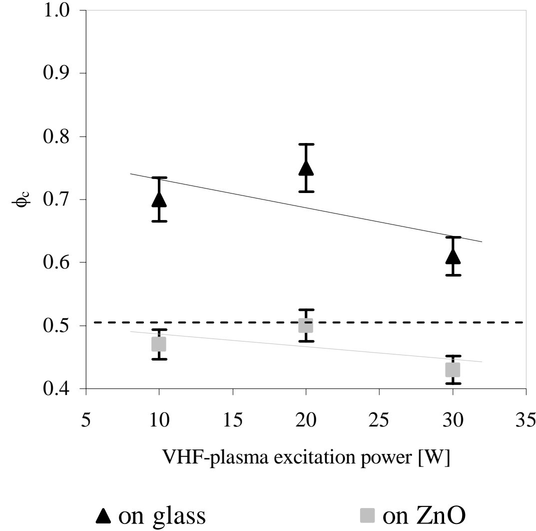

Fig. 2.5: VHF plasma excitation power series vs. Raman crystallinity factor ϕ_c on glass and ZnO.

The power series in Fig. 2.5 also did not show any significant improvement of the Raman crystallinity factor ϕ_c. For higher as well as lower plasma excitation power, the values of ϕ_c are even lower than for the "standard" power of 20 W. Neither has σ_{dark} conductivity been improved, e.g. it remained in the range of 10^{-3} to 10^{-7} S/cm.

These σ_{dark} conductivity values of the TMB/SiH_4 dilution series at 70.0 MHz are too low for the incorporation of these p-layers in a p-i-n solar cell, as they should attain at least the order of 10^0 S/cm [56].

Higher doping levels could only be achieved by the increase of the plasma excitation frequency to 110.0 MHz, as shown at the beginning of the present chapter in Fig. 2.1.

Conclusions:

The optimisation series for ***TMB p-doped μc-Si:H layers*** emphasizes the ***necessity of using an very high plasma excitation frequency of 110.0 MHz*** in order ***to attain a sufficiently high conductivity levels for μc-Si:H layers***. The best p-doped μc-Si:H layers had a Raman crystallinity factor of 0.5 – 0.6 on ZnO with a conductivity of 2 to 3 S/cm for a thickness of about 25 nm measured on the plain glass substrate.

2.1.3. Alternative Methods for μc-Si:H TMB p-doped layers

The initial limitations with respect to a too high TMB source-gas concentration in the bottle demanded for alternative methods to obtain good conductive μc-Si:H p-doped layers. In the following paragraphs we show three approaches. The first is H_2-recrystallisation of an amorphous p-doped layer, the second the introduction of an intrinsic microcrystalline nucleation layer and, finally, a simple pre-deposition plasma applied to the underlying LP-CVD ZnO layer, a plasma of either H_2 or CO_2.

2.1.3.1. H_2-Recrystallisation of amorphous p-layers

Hydrogen plasma recrystallisation was reported to significantly ***increase the Raman crystallinity factor*** of initially amorphous layers and permit growth of microcrystalline layers [66].

Experimental:

Various hydrogen plasmas for recrystallisation have been applied to an amorphous TMB p-doped layer (deposition cond: 0.8 mbar, ϕ(TMB)= 0.5 sccm, $\phi(SiH_4)$= 1.2 sccm, $\phi(H_2)$= 150 sccm, P= 10 W at f= 70.0 MHz, thickness≈ 60 nm) on LP-CVD ZnO-coated glass substrates. In order to illustrate the impact of the hydrogen plasma, a series of different exposure times of the p-layer, as exposed to hydrogen bombardment by the hydrogen plasma, was carried out. The applied hydrogen plasma conditions were chosen in view of yielding a low energy ion-bombardment [67] (p= 0.15 mbar, $\phi(H_2)$=15 sccm, P= 10 W at f= 60MHz), needed to avoid the etching of the p-layer, i.e. by sputtering.

Results and discussion:

The series, as characterized by Raman spectroscopy (Fig 2.6), shows an initial amorphous p-doped layer with a very slight microcrystalline peak at about 520 cm^{-1}.

With ***increasing exposure time to the hydrogen plasma***, an ***increase of the microcrystalline fraction*** is observed, continuing ***up to 30 minutes exposure time*** (see Fig.2.7).

At ***longer exposure times (> 30 min.)*** to the hydrogen plasma, an ***inhomogeneous etching effect*** is then visible (by eye) as shown in Fig. 2.8 (sample right).

This etching effect is very strong in the centre of the sample, and even leads to a complete removal of the layer – which has an initial thickness of 60 nm- in the centre after 45 minutes, while the remaining layer on the border still exhibits an increasing Raman crystallinity factor ϕ_c (Fig. 2.7). The drastic etching effect is illustrated in Fig. 2.8.

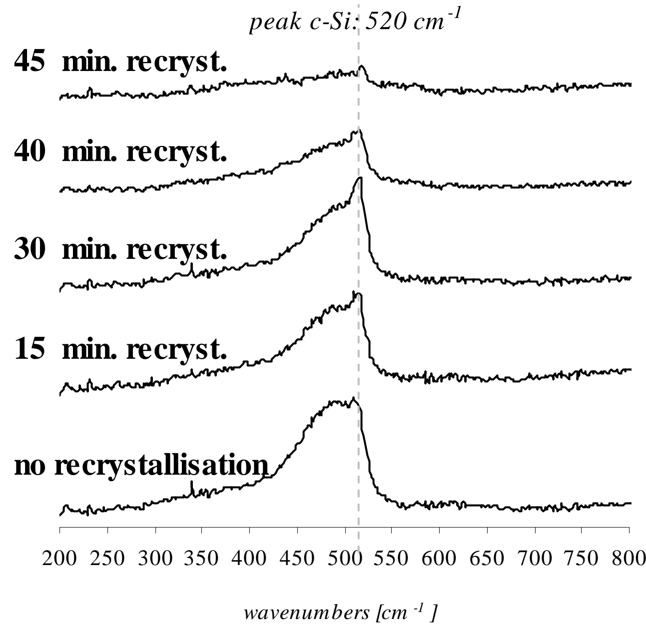

Fig. 2.6: Series of Raman spectra of TMB-doped p-layers on ZnO substrates with different exposure times to a H_2-recrystallisation plasma (experiment time increases from bottom to top). An increasing Raman crystallinity factor can be observed by the increase in the peak related to the material's crystalline phase at 520 cm^{-1}.

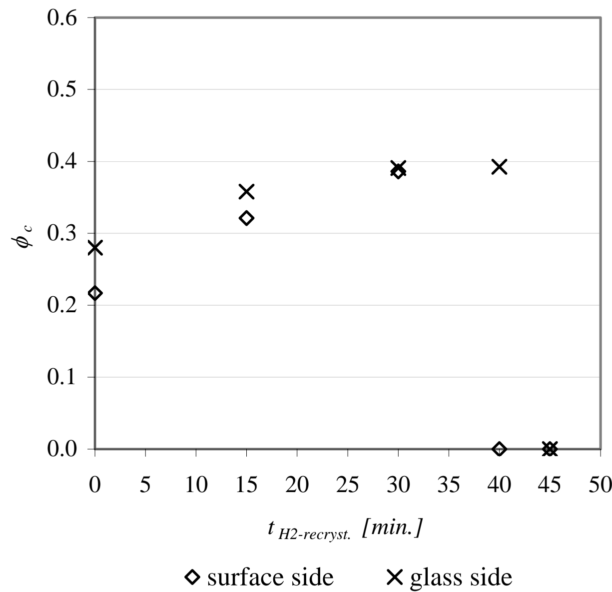

Fig. 2.7: Graph showing the Raman crystallinity factor ϕ_c vs. H_2-plasma exposure time for different depth on the sample (on surface and glass sides).

The recrystallisation study of TMB p-doped amorphous Si:H layers shows an increase of the Raman crystallinity factor from about 0.25 to 0.5 from amorphous towards microcrystalline material. Unfortunately, no further improvement in ϕ_c could be achieved, without a partial removal of the p-layer in the centre. Due to that unsatisfactory result, the recrystallisation

method was no further pursued.

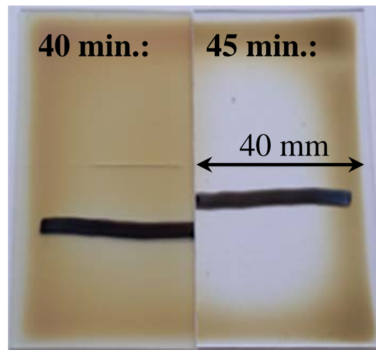

Fig. 2.8: Optical photographs of H_2-recrystallized TMB p-doped Si:H layers showing an increasing inhomogeneity after 40 min. (left) and 45 min. (right) etching.

Conclusions:

Hydrogen recrystallisation induced an improvement of the Raman crystallinity factor ϕ_c of the initially amorphous p-doped Si:H layers. Unfortunately, ϕ_c could not be improved to more than a value of ~ 0.5 and ***in the same time the hydrogen etching introduced very strong*** p-doped layer ***thickness inhomogeneities***, i.e. locally the layer was completely etched away.

2.1.3.2. Influence of an intrinsic nucleation layer for TMB-doped p-layers

For a good p-layer to be used in a μc-Si:H solar cell, the Raman crystallinity factor ϕ_c – as observed by Raman spectroscopy – based on the experience in our laboratory with p-doped layers the value must be above 0.3. If it is too low, the p-layer is too amorphous this leads to a lower V_{OC} value in solar cells and to the subsequent growth of an unsatisfactory crystalline i-layer. ***The introduction of an undoped Si:H nucleation layer*** should ***act as a nucleation layer for p-layer growth*** and enhance the Raman crystallinity factor ϕ_c of the subsequently grown Si:H p-layer, so as to achieve more microcrystalline material.

Experimental:

The deposition parameters of the applied nucleation layer correspond to the p-doped layer, except for the doping gas, which is not applied.

For the p-doped Si:H layer the following deposition conditions were used in this series: p= 0.8 mbar, ϕ(TMB)= 0.5 sccm (0.8 % TMB/SiH_4 @ 2 % TMB dilution in H_2), ϕ(SiH_4)= 1.2 sccm, ϕ(H_2)= 150 sccm, P= 10 W at f= 70.0 MHz, t= 10 min.). The depositions

were carried out as co-depositions on plain glass and on LP-CVD ZnO-coated glass substrates

Since the nucleation layer should not be too thick (< 10 nm) – else we have already a partial loss in absorption of the incident photons - the thickness of the total "p-layer" (nucleation and p-doped layer) was always checked by a step step profile-meter.

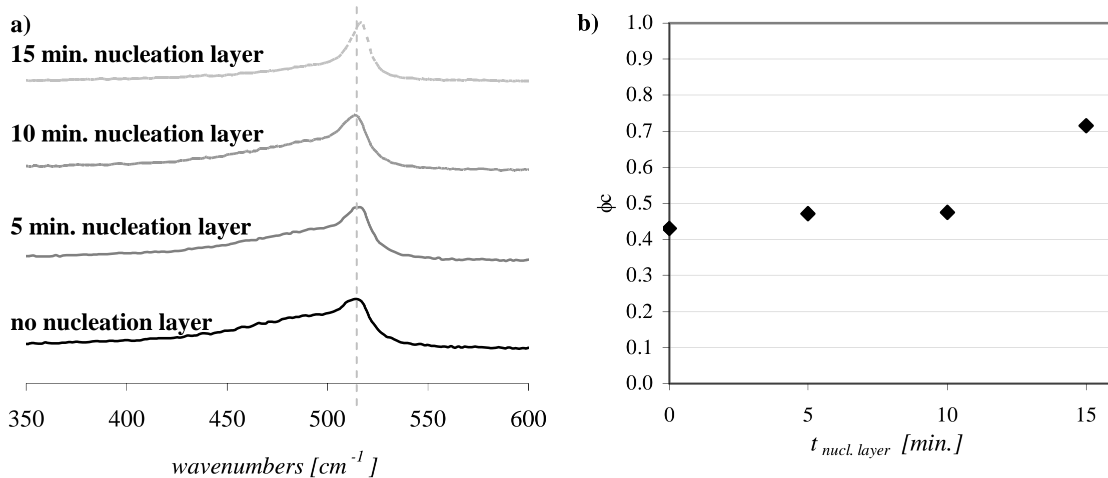

Fig. 2.9: a) Raman Spectra of a p-doped layer series on ZnO with the undoped nucleation layer (0 min., 5 min., 10 min. & 15 min.) and b) the corresponding ϕ_c vs. nucleation layer deposition time.

The analysis of the layers quality was done in a first step, by Raman spectroscopy with respect to their Raman crystallinity factor ϕ_c when deposited on ZnO, and in a second step the electrical dark-current conductivity σ_{dark} at RT was determined on substrates on glass.

<u>*Results and discussion:*</u>

The series of nucleation layer illustrates an improvement of the Raman crystallinity factor ϕ_c. However, as shown in Fig. 2.9 by the Raman spectra as well as by the ϕ_c–values, the Raman crystallinity factor of the p-doped Si:H layer was only essentially increased after a long deposition time of the nucleation layer. Due to the similar deposition conditions for all p-layers of this series – p-layer thickness can be presumed to be the same for all p-layers-, we can assume that the increase in ϕ_c is not an effect of the p-layer thickness.

Indeed, the thickness of the simple p-doped layer (on ZnO) without any underlying nucleation layer ($t_{nucl.layer}$= 0 min.) is about 30 nm.

Based on the thickness of the p-layer and the measured value for the total thickness, we calculated the thickness of the intrinsic nucleation layer. Hereby, the following thicknesses ($d_{nucl.layer}$) were calculated from the total thickness: for $t_{nucl.layer}$= 5, 10, 15 min. were obtained a

$d_{nucl.layer}$ of 30, 40 and 70 nm, respectively.

In order to observe an essential impact on ϕ_c, the nucleation layer needs in our case to be very thick, i.e. a significant improvement is shown for $d_{nucl.layer}$ of 70 nm thickness (15 min. deposition time).

Our nucleation layer approach is unfavourable due to the need of much too long deposition time of the undoped nucleation layer and the resulting total p-layer thickness. Indeed, the whole "p-layer" structure would have a thickness of 100 nm – in the solar cell device an optimal p-layer thickness should be about 10 nm – and, therefore, absorb incident photons before they reach the intrinsic layer of the solar cell.

Furthermore, σ_{dark} conductivity measurements only yielded values in the order of 10^{-1} S/cm, which reveals an insufficient doping of the p-layers. Consequently, the boron doping should be increased to higher TMB flow rates, but this would decreases ϕ_c towards low values typical of mainly amorphous material.

However, it might be possible to enhance the crystalline growth of a p-doped μc-Si:H layer, if an undoped μc-Si:H layer with a much higher hydrogen dilution was applied. Nevertheless, the basic issue of the p-doped layers was the too high TMB source-gas concentration (2 % TMB) which favoured amorphous growth.

Conclusions:

The incorporation of an ***underlying μc-Si:H nucleation layer could improve the Raman crystallinity factor*** drastically. Though, by using the same deposition parameters as for the p-doped layer – except the doping gas- the nucleation layer needs to be very thick (~70 nm) to have an advantageous impact on ϕ_c. Because of this, the ***undoped nucleation layers*** as used in this study are ***not suitable for obtaining thin highly crystalline p-doped μc-Si:H layers*** usable within μc-Si:H solar cells.

2.1.3.3. Influence of a pre-deposition plasma on the growth of the p-layer

Even though neither the H_2-recrystallisation of the p-layer (see 2.1.3.1) nor the introduction of an undoped μc-Si:H nucleation layer (see 2.1.3.2) led to satisfactory results, two suitable substrate surface treatments were found to be effective, as shown in the following.

The simple ***application*** of either a ***hydrogen plasma or a CO_2 plasma on the LP-CVD ZnO substrate leads afterwards to a subsequent growth of a highly microcrystalline p-layer***.

Under the same deposition conditions on untreated ZnO, an amorphous p-layer is grown (Fig. 2.10). The pre-deposition plasma is suspected to change the surface chemistry (oxidation state) as well as the nano-roughness of the ZnO layer. The beneficial effect of a hydrogen pre-deposition plasma on ZnO was already reported in the literature, when the plasma was shown to modify the surface morphology [68], leading to a positive effect on the crystallisation of subsequently grown, overlying μc-Si:H layers. In contrast to this, the use of CO_2 pre-deposition plasma was so far not reported in the literature as leading to a similar effect.

Experimental:

The study of the pre-deposition plasma was carried out on "IMT standard" LPCVD ZnO (process: M4 36min.). Before depositing a TMB p-doped μc-Si:H layer the pre-deposition plasma was applied on the ZnO-coated substrate glass. In the case of a H_2 plasma the following treatment parameters were applied: p= 1 mbar, $\phi(H_2)$= 100sccm, P= 50W with 70.0 MHz, t= 10 min. In the case of a CO_2 plasma the following parameters were applied: p= 0.46 mbar, $\phi(CO_2)$= 10.0 sccm, P= 10 W with 70.0 MHz, t= 4 min.

On one hand we apply for the H_2 plasma an increased plasma excitation power of about 0.4 W/ cm^2, on the other hand we apply for the CO_2 plasma a rather low power of about 0.1 W/ cm^2. Due to the power difference, we can expect different interaction behaviours with the ZnO surface, chemically as well as physically.

In a first step the impact of the pre-deposition treatments on the ZnO surface was studied on the overlying p-layer. Therefore, for both treatments the Raman crystallinity factor ϕ_c (measured by Raman spectroscopy) of the overlying p-doped μc-Si:H layer (two separate depositions with the same parameters) was compared for the case with and without ZnO treatment (blind probe). In a second step, the morphology of the ZnO surface exposed to H_2 or CO_2 plasma – without overlying p-doped layer - were studied by Scanning Electron Microscope (Philips XL30 ESEM-FEG) in order to see any changes in roughness of the ZnO surface. In order to have a blind probe for the case of no plasma exposition, half of the ZnO-coated substrate was covered during the treatment – this part was not exposed to the plasma.

Results and discussion:

The blind probes, initial TMB p-doped Si:H layer were too amorphous as shown by the Raman crystallinity factor ϕ_c-values of less than 0.3 for the Raman spectra in Fig. 2.10. However, ***after exposing ZnO either to a H_2 or a CO_2 plasma, the ϕ_c-values drastically increased towards μc-Si:H material***. Further optimisation – only done for the CO_2 plasma -

allowed us to obtain even higher ϕ_c–values up to 0.6- 0.7, as shown in chapter 2.1.1.

In order to study the impact of the H_2 and the CO_2 plasma on the ZnO layer, SEM micrographs were taken with enlargements up to 80000 magnification on the untreated as well as on the plasma treated section of the ZnO samples. The ***treatment by plasma did not change the long range (scale ~ 100 nm) surface morphology*** in neither case. A typical ***pyramidal texture*** in the order of 10^2 nm of the ZnO surface can be ***presumed*** to exist before the treatment. It is also seen in Fig. 2.11 left. However, the fine t***exture of the previously smooth pyramid plains was strongly roughened by the application of an H_2 plasma***, as micrographs of Fig. 2.11 a) show. The micrograph clearly illustrates in a ***short range roughening (< 5 nm)*** which may facilitate crystallisation of a subsequently grown, overlying p-doped μc-Si:H layer as already reported by S. Hasegawa et al. [69].

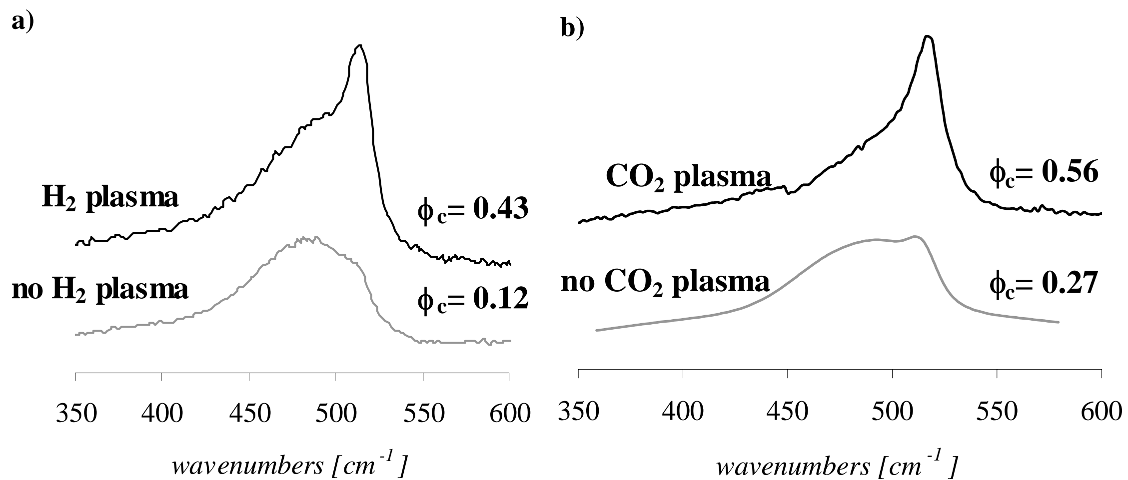

Fig. 2.10: The Raman spectra of 2 TMB-doped p-layers show the change from an amorphous (lower curve) to a microcrystalline layer (upper), when applying a pre-deposition H_2 plasma (a) or CO_2 plasma (b), on the ZnO-coated glass substrate.

On one hand the enhanced Raman crystallinity factor ϕ_c of the TMB p-doped μc-Si:H layer as observed by Raman spectroscopy (Fig. 2.10 a) for the H_2-plasma treatment could be explained by the enhanced fine texture on the pyramid facets yielding an increased nucleation density for the p-doped layer [69]. On the other hand, Zn clusters were found on the ZnO substrate surface after exposition to a hydrogen plasma as reported by Y.M. Strzhemechny et al. [68]. Here, they explain the formation of Zn by interaction of ZnO with CO to form Zn.

In the case of ***CO_2 plasma treatment*** a ***strongly improved Raman crystallinity factor ϕ_c*** of the p-doped μc-Si:H layer is also observed. Nevertheless, the SEM micrograph (Fig. 2.11 b) does not show any change of fine texture on the pyramid facets at a magnification of 40’000. Therefore, we do not suspect a roughening effect – this would be of an even much smaller order than the one observed for the H_2-plasma- but ***rather a chemical modification*** as already

reported by Y.M. Strzhemechny et al. [68] of the ZnO surface by the CO_2 plasma which would favour the crystalline growth of the overlying p-doped μc-Si:H layer.

In our case we bring up a hypothesis of a possible redox reaction, where ZnO is chemically reduced to Zn [70] as described in Equ. 2.2 during the CO_2 plasma exposition.

$$ZnO\ (s) + CO \rightarrow Zn + CO_2 \qquad \text{Equ. 2.2}$$

a) H_2 plasma pre-treatment:

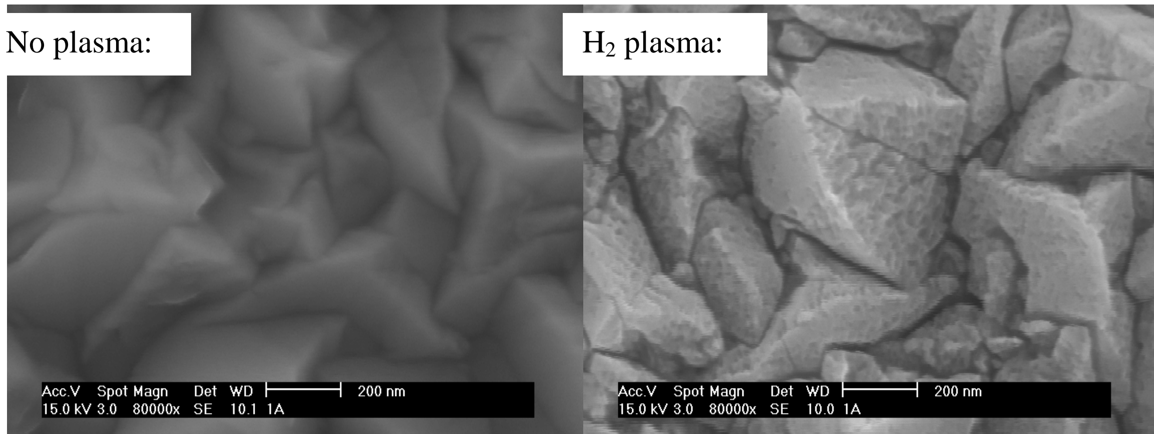

b) CO_2 plasma pre-treatment:

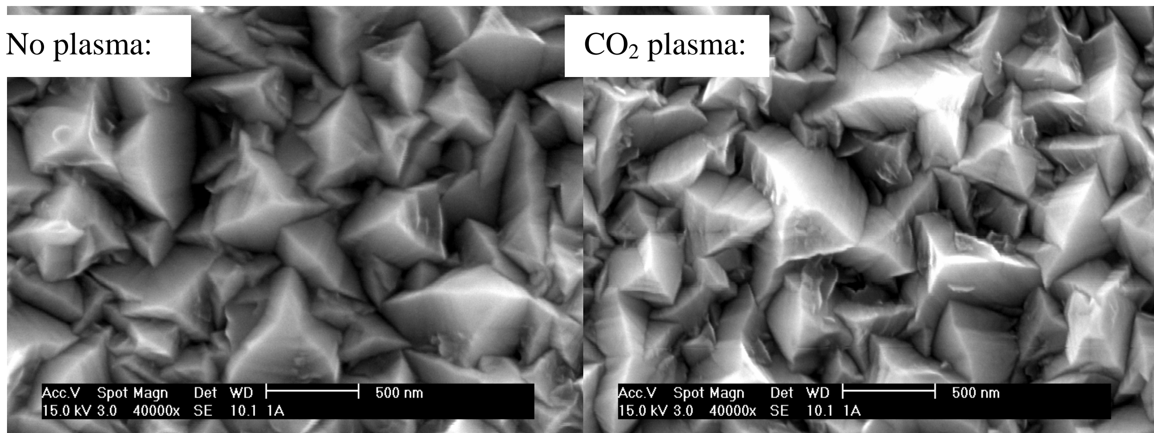

Fig. 2.11: SEM-graphs of untreated (left) and pre-deposition treated (right) ZnO surface: treated by (a) H_2 plasma and by (b) CO_2 plasma.

During the plasma the CO_2 molecule is decomposed to CO which then can reduce ZnO to Zn and itself oxidizes to CO_2. Due to the molecular scale mechanism of the reaction, we can expect the formation of very small sub-nano scale clusters of Zn on the ZnO layer surface, i.e. on the pyramid facets. Crystallisation of p-doped μc-Si:H layers could then be initiated by the Zn-clusters on the surface. However, our limitation in magnification to 80'000 by the SEM did us not allow to see any roughening on the pyramid facets.

This hypothesis, however, would therefore have to be proven by chemical surface analysis

with respect to the presence of ZnO and Zn clusters of the sub-nano scale size.

Unfortunately, the required analysis equipment (such as XPS) to carry out chemical surface analysis was not abailable.

<u>*Conclusions:*</u>

A ***pre-deposition plasma of H_2 as well as CO_2 on the ZnO layer gives a beneficial effect for crystallisation during the subsequent growth of overlying p-doped μc-Si:H layers***.

2.1.4. Conclusions on p-doped μc-Si:H layers

It is of great importance to have a "very microcrystalline" p-doped layer for microcrystalline p-i-n solar cell devices.

A proper ***tuning of the TMB-concentration level*** is, therefore, a must, so as to ensure that the ***TMB-concentration is neither too high – this increases the amorphous volume fraction - nor too low – this leads to an insufficient electrical cark-current conductivity σ_{dark}.***

Ideally, good p-doped μc-Si:H layers have a Raman crystallinity factor ϕ_c of more than 0.3 [45] and an electrical conductivity with a σ_{dark}-value in the order of 10^0 S/cm [56]. Using trimethylboron (TMB) doping gas, such p-doped μc-Si:H layers similar to those achieved as for B_2H_6 could be obtained.

The ***optimisation series for TMB p-doped μc-Si:H layers*** (using a TMB source-gas concentration of 500 ppm TMB diluted in H_2) revealed the ***necessity of an very high plasma excitation frequency of 110.0 MHz*** in order ***to attain a sufficiently high conductivity level and a high crystallinity for μc-Si:H layers.*** The ***best p-doped μc-Si:H layers*** had ***Raman crystallinity factors of 0.5– 0.6*** on ZnO-coated substrates, and a ***conductivity of 2 to 3 S/cm*** for a thickness of about 20 nm on plain glass substrates.

Because we initially had a rather too high source-gas concentration of 2 % TMB diluted in H_2, we could at first not obtain TMB-doped p-type layers with sufficient Raman crystallinity factors (ϕ_c remained below 0.3) and high enough conductivity (σ_{dark} remained below 10^{-2} S/cm). We therefore, searched for other methods for increasing Raman crystallinity factors. The most successful method to increase the Raman crystallinity factor was an pre-deposition plasma applied on the ZnO layer coated glass substrate (see below).

However, gas flow controllers had to be used beyond their garantied minimal and maximal flow rates. Finally, we changed the TMB source-gas bottle from 2 % to 500 ppm TMB-

concentration (factor 40 lower bottle concentration) which significantly facilitated the optimisation of p-doped μc-Si:H layer growth.

For other alternative methods the following was found:

A pre-deposition plasma of H_2 as well as CO_2 on the ZnO layer gives a beneficial effect for crystallisation during the subsequent growth of overlying p-doped μc-Si:H layers.

Hydrogen recrystallisation also induced an improvement of the Raman crystallinity ϕ_c of the initially amorphous p-doped Si:H layers. However, ϕ_c could here not be improved to a value higher than ~0.5; at the same time the hydrogen etching introduced very pronounced inhomogeneity in layer thickness.

The incorporation of an underlying undoped μc-Si:H nucleation layer could improve the Raman crystallinity drastically. However, the nucleation layer needed to be very thick (~70 nm) to have an advantageous impact on ϕ_c. Therefore, we concluded that the use of undoped nucleation layers alone is not suitable for the deposition of highly crystalline and conductive p-doped μc-Si:H layers.

2.2. Development of high-rate deposited intrinsic μc-Si:H layers

A high-quality intrinsic microcrystalline silicon (μc-Si:H) layer is one of the key issue for the development of the microcrystalline solar cells and of "Micromorph" tandem solar cells.

In order to obtain a ***satisfactory absorption of the incident light***, the ***microcrystalline intrinsic layer needs to have a thickness of 2 to 4 μm. Combined with efficient light trapping even less than 2 μm thickness is sufficient in the case of the "Micromorph" tandem solar cell [71]***. Unfortunately, "state-of-the-art" microcrystalline solar cells (IMT Neuchâtel) consist of intrinsic μc-Si:H layers that are deposited at deposition rates of only 1-5 Å/s. Therefore, the μc-Si:H i-layer deposition step is the most time consuming step in the deposition sequence of the solar cell. The slow deposition is an important limiting step for the industrialisation of the "Micromorph" tandem solar cell concept.

For this reason, the present study ***focuses on increased growth-rate of μc-Si:H layers***. This was achieved by: ***1) increasing Very High Frequency-excitation power*** (2.2.1) ***2) using high-pressure regime combined with VHF*** (2.2.2).

The ***first approach*** led to ***μc-Si:H device-grade layers deposited at growth-rates up to 10 Å/s. The second approach*** led to ***growth-rates up to ~25 Å/s.***

In the context of the high-pressure regime, the plasma confinement box had to be adapted so as to ensure sufficient homogeneity of layer thickness homogeneity as well as to reduce formation of silicon powder (see chapter 4).

As an introduction to the methodology used here, we shall consider in the following the demands for a device-grade, high-rate μc-Si:H intrinsic layer deposition.

In principle, a ***high density of growth precursors is needed in order to achieve high rates***, e.g. the density of "microcrystalline growth favouring" precursors obtained from the dissociation of silane must be high compared to the density of the "bad" precursors – favouring silicon powder formation.

The prevailing conditions controlling the plasma are the determining factors for the chemical reactions leading to a high density of "good" growth precursors obtained from the dissociation of silane. A low electron temperature and a higher electron density could be favourable within the neutral plasma [72]. Here, the electron density would be the dominating

factor controlling the formation of the essential growth precursors, e.g. free-radicals[3].

These plasma conditions are controlled, as shown in following diagram, by the process parameters and by the system configuration, and determine the characteristics of the growing Si:H layers.

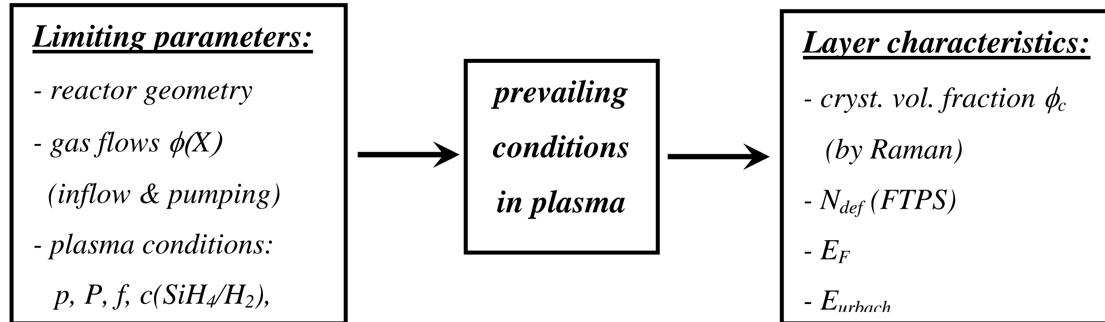

In order to have device-grade intrinsic μc-Si:H layers, the plasma needs to have a sufficient density of "good" silane growth precursors.

However, it has so far not clearly been reported which radical species obtained from the dissociation silane – $SiH_3^{\bullet}$, $SiH_2^{\bullet}$, or $SiH^{\bullet}$- acts as "good" and which act as "bad" growth precursors. For instance, $SiH_2^{\bullet}$ is reported to facilitate polysilane formation, e.g. silicon based powder [73] , while $SiH_3^{\bullet}$ is suspected to be the favourable "good" growth precursor [74]. At any rate, the electrons are known to be the initiators of the free-radical formation reactions, as shown below for some possible reactions forming silane derivatives, such as free-radicals of silane or ionized silane [75].

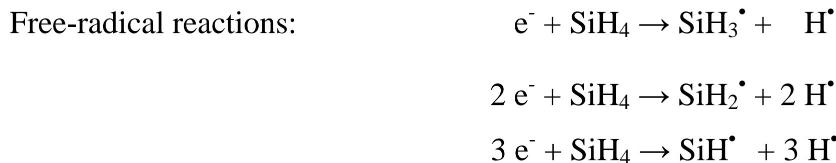

Free-radical reactions:

$$e^- + SiH_4 \rightarrow SiH_3^{\bullet} + H^{\bullet}$$

$$2\,e^- + SiH_4 \rightarrow SiH_2^{\bullet} + 2\,H^{\bullet}$$

$$3\,e^- + SiH_4 \rightarrow SiH^{\bullet} + 3\,H^{\bullet}$$

So far, one does not clearly know which growth precursor species in the above mentioned reactions are favourable and which are unfavourable for the growth of microcrystalline Si:H material of device-grade quality.

Indeed, not only free-radical reactions can be induced by the electrons of the plasma, but also ion-formation reactions. In contrary to the $SiH_x^{\bullet}$, all ions formed by dissociation of silane are basically unfavourable, due to their degrading impact by ion-bombardment during the growth of the microcrystalline Si:H layer. Some ion-formation reactions, as follows will be listed.

---

[3] The chemical nomenclature denotes a free-radical with a superscripted dot; in our case, as follows, $SiH_x^{\bullet}$ and $H^{\bullet}$.

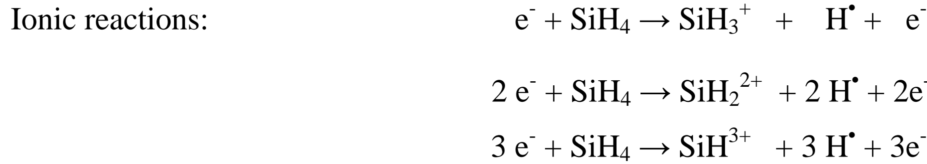

Ionic reactions: $e^- + SiH_4 \rightarrow SiH_3^+ + H^\bullet + e^-$

$$2\,e^- + SiH_4 \rightarrow SiH_2^{2+} + 2\,H^\bullet + 2e^-$$

$$3\,e^- + SiH_4 \rightarrow SiH^{3+} + 3\,H^\bullet + 3e^-$$

It is known that polysilanes which appear as silicon-based powder in the process chamber result from species of “bad” precursors.

In the plasma, H_2 can be ***dissociated directly to free-radical hydrogen ($H^\bullet$)*** - also called atomic hydrogen. Plasma induced hydrogen dissociation values, however, were reported to be rather low (in the case of a pure H_2 plasma) at about 10 % [76].

Therefore, free electron induced reactions (shown above) seem to dominate the plasma chemistry. Nevertheless, ***a high atomic hydrogen density*** is known as being ***crucial for microcrystalline silicon growth [77]***.

So far, only some links between process conditions, plasma prevailing conditions for the growth precursor and Si:H layer characteristics are known.

Polysilanes are formed especially in the high-pressure regime (> 1 mbar) and appear as powder in the plasma zone. Note that powder formation does not necessarily deteriorate device performance, as has been shown at least for amorphous Si:H layers [78]. However, the particle has to remain in the plasma and should not fall on the substrate.

It is known that high density of atomic hydrogen is favourable to obtain μc-Si:H material – too low hydrogen dilution and related low density of atomic hydrogen favours amorphous growth. High density of atomic hydrogen can be achieved with high H_2 dilution. Hereby, an enhanced atomic hydrogen bombardment can be expected. The bombardment energy, however, should not be too high, because there will otherwise be detrimental effects on μc-Si:H characteristics, e.g. defect generation is increased.

In order to attain ***high deposition rates for μc-Si:H material, SiH_4 molecules need to be dissociated into “good” growth precursor free-radicals as completely as possible***. Therefore, a strong dissociation of SiH_4 should be promoted by the deposition conditions, e.g. a high silane depletion is said to be obtain by HPD [77]. .

Higher deposition rates of μc-Si:H material can be obtained by ***increasing excitation power***. Hereby, we can assume that the dissociation of SiH_4 to its growth precursor is increased. But unfortunately, this leads also to increased ion-bombardment; this effect limits the range in which plasma excitation power can be increased and device-grade μc-Si:H layers still obtained.

The growth-rate is determined by the flux density of the growth precursors such as $SiH_x^\bullet$

radicals, and the ***generation rate of radicals*** G_r is given by the following expression,

$$G_r = n_e \times v_e \times N_g \times \sigma_d, \qquad \text{Equ.2.3}$$

where n_e and v_e are the density and velocity of energetic electrons, respectively, with a kinetic energy higher than the dissociation threshold of the source-gas molecule such as SiH_4. N_g and σ_d are, respectively, the density and the dissociation cross section of the source-gas molecule [77].

Very high plasma excitation frequencies were also reported to ***increase the deposition rates for μc-Si:H material***. An enhanced electron impact dissociation of SiH_4 may be expected in this case [26, 79]. The enhanced dissociation then results in a higher surface reactivity due to a coincident increase of the ion flux towards the electrodes. This is facilitated by a decrease of the sheath zone (d_{sheath}) due to the influence of very high frequencies [31].

For the ***case of higher pressures*** (> 1 mbar) one can ***expect*** to have a ***similar effect***, i.e. ***energetically decreased ion-bombardment***, even if the deposition rate of μc-Si:H layers is increased. Higher pressure decreases the sheat-thickness in which the ions are accelerated, e.g. the ions are less accelerated.

However, in the present work the pumping system used for our deposition system (see chapter 2.1) seems to have been one of the most important factors limiting deposition rate. The pumping rate of our pump was 4.2 m^3/ min.; and this value can be considered to be much too large for a chamber volume of about 16 litres (0.016m^3).

2.2.1. Power series at low pressure

The most straight forward approach to increase the deposition-rate is to simply increase plasma excitation power. This was already shown for different VHF excitation frequency for a simple parallel plate design by Pedro Torres [63], but not for the case of a plasma confinement box (see Appendix B).

However, too high VHF plasma excitation power finally leads to an increased defect density of intrinsic μc-Si:H layers, and this certainly has a detrimental effect on devices made with such μc-Si:H material. Defective, intrinsic μc-Si:H layers lead to low V_{OC}-values; in some cases the deposited layers become amorphous instead of being microcrystalline, if the rate is strongly increased.

The most obvious effect of increasing plasma excitation power is a shift of the transition boundary between microcrystalline and amorphous Si:H intrinsic growth towards higher

silane concentrations[4], as observed in the Fig. 2.12.

Experimental:

The following power series for the growth of intrinsic μc-Si:H layers is based on "IMT state-of-the-art" conditions for μc-Si:H layers. The experimental parameters of the series were: p= 0.3 mbar for gas flow rates of 25.0 sccm H_2, with varying SiH_4 flows of 1.0 (3.85 % $\phi(SiH_4)/\phi_{total}$) to 4.0 sccm (3.9 % to 13.8 % $\phi(SiH_4)/\phi_{total}$, respectively), applied for VHF excitation power of 5, 10, 20 and 30 W at an excitation frequency of 70.0 MHz.

The distinction between microcrystalline and amorphous material was obtained from optical absorption measurements performed with Photothermal Deflection Spectroscopy (PDS).

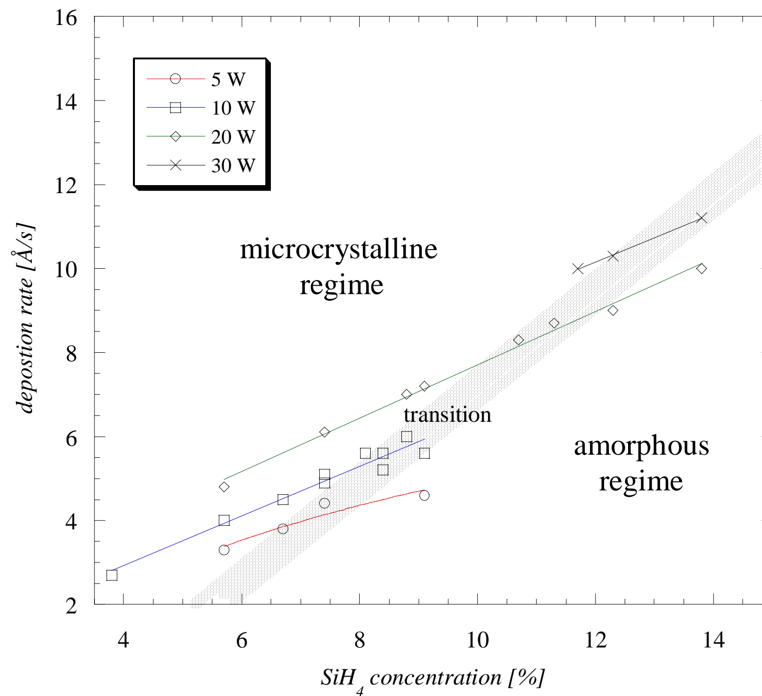

Fig. 2.12: Dilution series of μc-Si:H at varying plasma power. Layers were deposited on LP-CVD ZnO. Deposition rate increases linearly with the SiH_4 concentration. The maximum value of dep. Rate reached is 10 Å/s at P = 30 W. Note the shift of the transition boundary between microcrystalline and amorphous growth to increasingly higher dilution values with the increase of the plasma power (from bottom to top of figure).

Results and discussion:

The ***power series*** (Fig. 2.12) where the VHF power is increased from 5 to 30 W indicates a ***linear shift of the transition point between microcrystalline and amorphous material*** from

[4] The silane/ SiH_4 concentration is defined as ratio of SiH_4 gas flux/total gas flux.

~7 % to ~12 % SiH_4 concentration ($\phi(SiH_4)/\phi_{total}$)). However, it is not clear if the partial pressure of silane in the plasma as well changes or remains stable.

The intermediate series for excitation powers at 10 and 20 W show transitions at ~8.5 % and ~10.5 % SiH_4 concentration ($\phi(SiH_4)/\phi_{total}$), respectively.

Hereby, the μc-Si:H layers of the transition regime – the Raman crystallinity ϕ_c were only about 40 % ($\phi_c \approx 0.4$) on glass- showed reasonably low residual defect absorption values α(~0.8 eV) between 1 and 2 cm^{-1} for the different power, i.e. a reasonably low defect density was obtained.

An increase of the deposition rate for μc-Si:H material from about 3 to more than 10 Å/s was achieved by the power increase from 5 to 30 W.

<u>*Conclusions:*</u>

Increasing power from 5 W to 30 W led to a shift of the transition regime of the μc-Si:H layers from about 7 % to 12 % SiH_4 concentration. Increasing ***the power*** results in an ***increase of the deposition rate from about 3 to above 10 Å/s for μc-Si:H material.***

2.2.2. Pressure series up to 8 mbar for VHF-GD

The main point of the present high-pressure study is that even higher deposition rates can be obtained for intrinsic μc-Si:H material.

In this case, by increasing pressure one avoids the detrimental large ion-bombardment energies otherwise prevailing at high plasma powers. At the same time we suspect that the mean residence time $\tau_{res.}$ of the beneficial (“good”) μc-Si:H material growth precursors is increased (see below). Thus a further increase of the deposition rate of μc-Si:H material can be obtained by the use of higher working pressures (>1 mbar).

Recently, several techniques using higher pressures (> 1 mbar) were reported, i.e. high-pressure RF-PECVD [28] and a kind of combination of VHF and high-pressure, known as HPD (High-Pressure Depletion) PECVD [29, 30]. In the second case the plasma conditions were such that silane was depletion limited by the high growth-rate. One then also speaks of “High-pressure Depletion (HPD)” regime. All these techniques show promising results for μc-Si:H solar cells with conversion efficiencies in the range of 8 - 10 % for deposition rates of 10 Å/s and more.

It is believed that the ***high-pressure conditions (> 1 mbar)*** lead to similar changes in the

plasma impedance as an increase in excitation frequency from the standard 13.56 MHz to frequencies in the VHF (Very High Frequency) range, i.e. to ***reduced ion-bombardment energy***. Therefore, ***VHF combined with high-pressure*** could in principle lead to ***even further*** beneficial effects for the ***increase in deposition rate***. Nevertheless, higher pressures can remain an issue with respect to high plasma excitation powers. Two possibilities will, in general, reduce power-induced ion-bombardment in order that fewer defects are created: On one hand, the use of increased plasma excitation frequencies (VHF) and, on the other hand, the use of higher pressure (> 1 mbar) with an increased collision rate.

We ***suspect*** that ***increased pressures*** (> 1 mbar) can ***lead to*** the following "chain of effects". The ***density of molecules, ions, radicals and electrons in the bulk plasma is increased.*** Consequently, an ***increase of collisions can be expected***. This ***results in a decreasing mean free path*** as well as ***in an increasing mean residence time*** $\tau_{res.}$ ***for the*** corresponding ***growth precursors if they do not collide again.***

In the plasma zone, however, increased collisions with an adapted higher power input could possibly enhance the electron-induced dissociation of SiH_4 to the "good" beneficial growth precursors.

Furthermore, if the ***sheath*** also ***becomes thinner at high-pressures*** an ***increased exposition of the growing surface to "good" growth precursors*** could be expected. Due to the increased collisions, a reduction of ion-bombardment energy can be assumed, which can then lead to decreased defect densities and eventually maintain high electrical performances of the resulting devices.

Therefore, high-pressures can, in principle, lead to increased growth-rates for high quality μc-Si:H layers.

Experimental:

In this work microcrystalline silicon growth using VHF-GD CVD was studied under conditions of high-pressure (> 1mbar) and high VHF-power (at a plasma excitation frequency of 70.0MHz).

In a first approach we studied simply the impact of increasing pressure from about 1 to 3 mbar on a series of layers deposited with otherwise fixed parameters. Then, the deposition parameters were further optimised in a dilution series at the "best" pressure of 3 mbar, with respect to high-rates.

During this development the square-shaped plasma confinement box originally present in our chamber (see Appendix B) had to be adapted to the high-pressure regime conditions and a

new cylindrical confinement box was introduced (see chapter 4).

In a second approach a large pressure regime ranging from 0.5 to 8 mbar was studied with the newly developed cylindrical plasma confinement box, using thereby a variable inter-electrode distance d_{gap}.

In the first series, the following parameters were varied: silane concentration $c(SiH_4)$= 4 - 12 %, for total gas flow rates in the range of about 25 -100 sccm and later even up to 500 sccm with varied plasma excitation power of 30 – 120 W for an excitation frequency of 70.0 MHz. The optimisation was always done with respect to the transition of μc-Si:H to a-Si:H material. The intrinsic layers were co-deposited on plain glass substrates and on LP-CVD ZnO-coated glass substrates.

The Si:H layers were characterized by Raman spectroscopy with respect to their Raman crystallinity ϕ_c on both substrates. For certain Si:H layers on glass, the electrical characteristics σ_{dark} and E_{act}, as well as defect density were measured. Defect density was evaluated by determining defect absorption α(0.8 eV) as measured by the CPM method [80]. Unfortunately, adhesion problems on glass substrates prevented these measurements on most of the layers.

Results and discussion:

Pressure series with square-shaped plasma confinement box

In a first series, a study (Fig. 2.3) was carried out up to pressures of 3 mbar, focussing on the deposition rate of μc-Si:H.

Hereby, we observed an increasing rate for μc-Si:H layers (on glass) when passing from the conventional pressure range (< 1 mbar) to higher pressures (> 1 mbar). The deposition rate above 1.5 mbar does not vary much more with increasing pressure which may be due to an excessive silane depletion condition and could possibly be compensated by a further increase in total gas flow and in plasma power.

Further optimisation at 3 mbar for even higher total gas flow rate and higher silane concentrations between 6.7 and 8.9 % allowed with an increased plasma excitation power (P=40 -100 W) an increase of the deposition rate of μc-Si:H material approaching 14 - 17 Å/sec (Tab. 2.1).

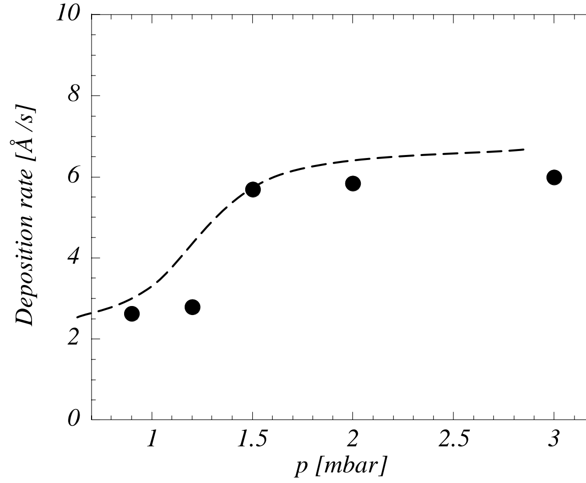

Fig. 2.3. Deposition rate vs. working pressure, starting in the conventional pressure regime and increasing to 3.0 mbar (dashed line is a guide to the eye).

Table 2.1 summarises for the samples with the highest deposition rate the results of these characterisations. First, Raman crystallinity factor ϕ_c of the Raman peaks clearly indicates highly crystalline Si:H material for most of the films. The relatively low sub band-gap absorption at 0.8 eV by CPM as sign for a rather low defect density (not defect density-values are given here, because the corresponding calibration factors are not universally accepted). From the dark conductivity measurements we obtained activation energies of around 0.5 eV with dark conductivities at room temperature (RT) in the range of 10^{-7} S/cm. These conductivity characteristics indicate clearly the "midgap character" (E_F is in the middle of the gap) of these high-rate microcrystalline films on glass. Thus, we consider having obtained device-quality films at rates up to 17 Å/sec, as given in Tab.2.1.

Deposition rate [Å/sec]	Raman cryst. factor ϕ_c	α(0.8 eV) [cm^{-1}]	σ_{dark} @RT [S/ cm]	E_{act} [meV]
13.7	0.656	~3.2	$5.3 \cdot 10^{-7}$	530
15.6	0.733	~2.0	$1.20 \cdot 10^{-7}$	497
16.8	0.639	~2.1	$2.03 \cdot 10^{-7}$	520

Tab. 2.1: Raman crystallinity ϕ_c, sub band-gap absorption and electrical characteristics (σ_{dark} & E_{act}) of high-rate deposited μc-Si:H layers (on glass).

In order to search for a further increase of the deposition rate we investigated the influence of even higher total gas flow rates (up to ~500 sccm) and higher VHF-powers (up to 200 W) on the growth of μc-Si:H.

In Fig. 2.4 a series of high-rate microcrystalline films could be obtained when applying a VHF-power of 120 W and a total gas flow of 100 sccm at working pressures of 3 mbar. As can be seen, the rate continuously increased with higher silane concentrations leading for μc-Si:H layers to remarkably high deposition rates of up to 25 Å/sec.

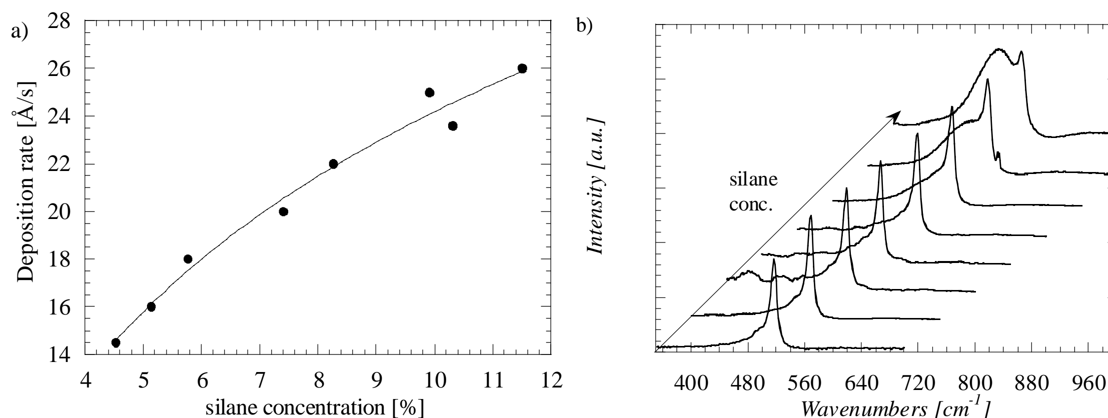

Fig. 2.4.: a) The deposition rate vs. SiH_4 concentration of μc-Si films, with high-pressure (3 mbar), b) corresponding series of Raman spectra, for increasing values of the silane concentration, measured on the surface side of the layer with a Ar laser (514 nm).

However, before going any further one has also to verify if also the initial growth of these layers (from the glass side) is reasonably microcrystalline under these high-rate conditions. Therefore, the microcrystalline structure was analysed by Raman spectroscopy from both sides of the layer (surface and glass side) in order to obtain information on the initial growth zone (glass side) adjacent to the substrate and compare it with the "final" growth zone on the surface (surface side). Raman spectra were measured with an Ar laser (514 nm) Raman Collecting Depth (RCD) 120 – 170 nm for μc-Si:H material [45]. The examined layers were in the thickness range of 2- 3 μm.

This quick check with Raman spectroscopy on the layer surface side (Fig. 2.4 b) indicated, furthermore, that these high-rate Si:H films show microcrystalline ϕ_c-values ($\phi_c > 0.5$) on the surface side. Good microcrystalline Si:H films with a ϕ_c–value of more than 0.5 were achieved up to 10 % SiH_4 concentration (Fig. 2.5) – the transition of microcrystalline to amorphous Si:H material – as shown for the surface side . Only the highest concentration, as shown in Fig. 2.4 a) led to a significant amorphous volume fraction in the material ($\phi_c < 0.5$). At the high-pressure of 3 mbar the transition has moved to a higher SiH_4 concentration of 10 % compared to the low pressure regime (< 1 mbar) where the transition is around 7- 8 %. The reason for this increase is so far not clear and must be further investigated (see end of present chapter).

The shift of the transition to a higher SiH_4 concentration as observed by Raman measurements on the surface side of the layer could perhaps be explained by an increased density of atomic

hydrogen in the high-pressure regime.

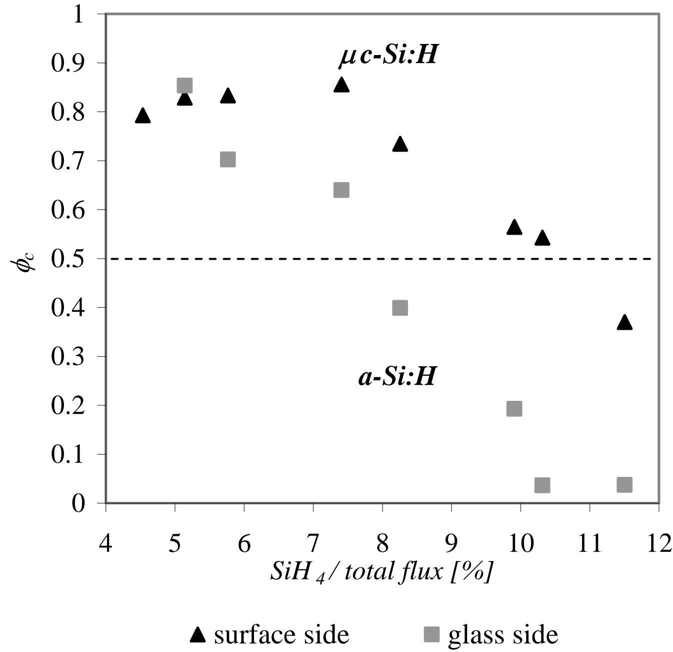

Fig. 2.5: Raman crystallinity factor ϕ_c of the SiH_4 concentration series at 3 mbar on ZnO-coated glass substrates measured from top and bottom side of the layer.

However, the Raman crystallinity factors ϕ_c on the glass side of the Si:H layers show a transition to amorphous Si:H material at lower SiH_4 concentration of about of 7 - 8 % – as known from the low pressure regime. Comparing ϕ_c-values of the surface and the glass side of the SiH_4 concentration series (Fig. 2.5), an increasing ϕ_c-gradient of up to 30 % (ϕ_c-value of about 0.3) is observed.

Such pronounced ϕ_c- gradients within intrinsic μc-Si:H layers were (as far as we can judge) so far not known. One has to assume that a slight, continuous change of growth conditions in the bulk plasma to happen during the deposition. Similar observations of a gradient of crystallinity in intrinsic layers were recently reported for high-pressure regime using RF-PECVD
(13.56 MHz) by M.v.d. Donker et al. [81]. The gradient is explained there by a plasma induced temperature increase of the substrate during the deposition process.

Taking into account the issue of the gradient (see Fig. 2.5) within the intrinsic layer, the series at a ***high-pressure of 3 mbar*** shows in Fig. 2.4 ***entirely μc-Si:H layers***– from bottom side to surface side- grown on ZnO, ***for a deposition rate of about 20 Å/s*** for a SiH_4 concentration of 7.5 %. These rates of μc-Si:H layers on ZnO were even achieved for reasonably low gas flow rates (~100 sccm).

Unfortunately, defect density by low sub band-gap absorptions could not be measured due to

the insufficient thickness of the layers (adhesion problems prevented us from obtaining the needed layer thickness of > 1 μm on glass). However, directly incorporated into a "jumping"[5] p-i-n solar cell, that kind of high-rate deposited μc-Si:H layer revealed problems in current collection (see chapter 3.3).

Finally, the microstructure was studied by means of the incorporation of a first intrinsic high-rate deposited μc-Si:H layer with a deposition rate of 14.5 Å/s (corresponds to the μc-Si:H layer with 4.5 % SiH_4 concentration of Fig. 2.4), into a "jumping" solar cell by TEM (see chapter 3.3).

Using the square plasma confinement box, the series leading to the high-pressure regime (> 1mbar) showed fundamental problems with the homogeneity of the layer thickness and also the a strong formation of powder.

Both problems were eliminated or at least drastically reduced by the optimisation (i.e. modification) of the plasma confinement box design (see chapter 4):

The ***cylindrical plasma confinement box removed the inhomogeneity issue in the high-pressure regime*** (see chapter 4.2). The ***powder formation*** could be ***drastically decreased by decreasing the inter-electrode gap*** d_{gap} from 20.0 mm to 9.5 mm (see chapter 4.3).

The further development on the present deposition system for this work was done with the novel cylindrical design of the plasma confinement box.

Pressure series for cylindrical plasma confinement box for varying d_{gap}

The change to the cylindrical plasma confinement box design demanded a verification of the previous high deposition rates of up to 20 Å/s for intrinsic μc-Si:H layers of the square plasma confinement box in the high-pressure regime.

The new electrode design consists of a cylindrical plasma confinement box. The showerhead electrode has a diameter of 130 mm (surface ≈ 132 cm^2) and the inter-electrode distance or gap (distance from the showerhead to the substrate, d_{gap}) can be set to 20.0, 16.5, 13.0, or 9.5 mm.

In the present series the ***pressure range was enlarged from 0.5 to 8 mbar***. The deposition rate of μc-Si.H material was maximised by systematically varying SiH_4 concentration, plasma excitation power and the total gas flux and ensuring, thereby, a Raman crystallinity factor ϕ_c

---

[5] The term „jumping" applies to a cell which had to be "jumped" from one reactor to the other -under exposure to atmospheric conditions- after deposition of the p-layer.

of around 0.5 (transition regime).

This procedure was carried out for the ***different inter-electrode gaps d_{gap}*** in the range of ***20 to 9.5 mm***.

Hereby, the following main parameters were varied:

The pressure increased from 0.5 to 8 mbar, SiH_4 concentration from 1 to 8 % and d_{gap} from, 20.0, 16.5, 13.0 to 9.5 mm.

d_{gap} [mm]	**deposition rate [Å/s]**	**p [mbar]**	$\Phi(SiH_4)$ [sccm]	$\Phi(H_2)$ [sccm]	$(\Phi(SiH_4)/\Phi_{tot})$ [%]	P_{in} [W]	P-density [W/cm2]	remarks
20.0	2.0	*0.35*	3.5	100	3.4	10	0.07	
	1.9	*0.60*	2.7	100	2.6	20	0.14	
	6.3	*1.50*	3.5	100	3.4	120	0.84	
	12.9	*2.00*	6.1	100	5.8	120	0.84	powder
	17.2	*3.00*	8.0	100	7.4	200	1.40	powder
	10.7	*4.00*	4.8	100	4.5	200	1.40	powder
16.5	2.2	*0.50*	3.6	100	3.5	20	0.14	
	2.4	*1.00*	5.0	100	4.8	30	0.21	
	1.9	*1.50*	2.7	100	2.6	60	0.42	
	5.4	*2.00*	5.4	100	5.1	120	0.84	
	13.3	*2.50*	6.0	100	5.7	200	1.40	powder
	16.9	*3.00*	8.0	100	7.4	200	1.40	powder
	19.4	*3.50*	10.0	100	9.1	200	1.40	powder
	15.9	*4.00*	8.0	100	7.4	200	1.40	powder
	9.7	*5.00*	5.0	500	1.0	200	1.40	
13.0	4.4	*2.00*	2.7	100	2.6	120	0.84	
	11.1	*3.00*	4.0	100	3.8	200	1.40	
	23.3	*3.50*	6.0	100	5.7	200	1.40	powder
	25.0	*4.00*	9.0	500	1.8	200	1.40	
	16.7	*5.00*	5.0	500	1.0	200	1.40	
	12.8	*6.00*	5.0	500	1.0	200	1.40	
9.5	5.3	*1.00*	4.0	100	3.8	60	0.42	
	4.7	*2.00*	2.7	100	2.6	120	0.84	
	5.6	*3.00*	2.0	100	2.0	200	1.40	
	12.2	*4.00*	4.0	100	3.8	200	1.40	
	27.8	*5.00*	10.0	500	2.0	200	1.40	
	24.4	*6.00*	10.0	500	2.0	200	1.40	
	19.4	*7.00*	9.0	500	1.8	200	1.40	
	14.4	*8.00*	5.0	500	1.0	200	1.40	

Tab. 2.1: Deposition parameters for the μc-Si:H layers of the pressure series (shown in Fig. 2.6).

Due to the very high pumping speed of our roots-pumping system, very high gas flow rates (up to 500 sccm hydrogen) were needed to maintain very high-pressures up to 8 mbar –otherwise these pressures could not be attained. In Tab. 2.1 key deposition parameters such as pressure, plasma excitation power (at 70.0 MHz), gas flow rates of SiH_4 and H_2 are

indicated. The corresponding deposition rates for intrinsic μc-Si:H layers, are shown in Fig. 2.6.

For the novel cylindrical designed plasma confinement box, with d_{gap} of 20.0 mm, the previous deposition rate of entirely (from bottom and top side of the layer) μc-Si:H layers with the corresponding growth-rate of 20 Å/s (Fig. 2.4) was not retrieved, as shown in Fig. 2.6 (grey bright line).

Nevertheless, all pressure series in the range between 0.5 and 8 mbar shown in Fig. 2.6, show clear maximum deposition rates of μc-Si:H layers for varying gap values d_{gap}. Furthermore, ***for decreasing d_{gap}, the pressure point of maximal deposition rate is shifted to higher pressures***, e.g. it shifts from 3 to 5 mbar while decreasing the gap from 20 to 9.5 mm, respectively.

The pressure series with d_{gap}= 20.0 mm yields a maximal deposition rate of about 18 Å/s at 3 mbar. Decreasing d_{gap} to 16.5 mm a maximal deposition rate of close to 20 Å/s was obtained at 3.5 mbar. At a d_{gap} of 13.0 mm the maximal deposition rate further increased to about 25 Å/s at 4 mbar. The ***smallest d_{gap} of 9.5 mm results in the highest maximal deposition rate of about 28 Å/s at 5 mbar***.

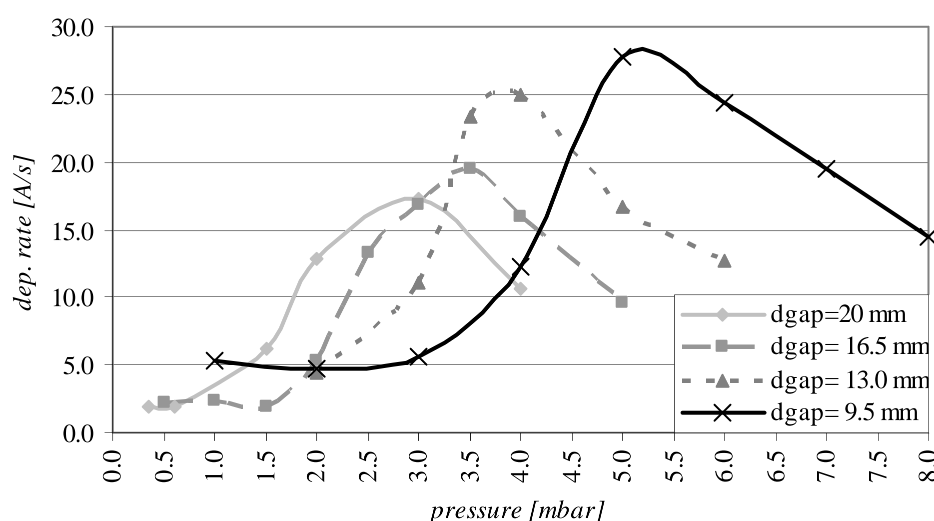

Fig. 2.6: Deposition rate of μc-Si:H layers on ZnO for different inter-electrode gap d_{gap} as function of the working pressure.

Focussing on the decrease of the d_{gap}, a clear increase of the maximal deposition rates of μc-Si:H layers from about 18 Å/s to 28 ***Å/s*** was observed.

The optimisation of the μc-Si:H layers with respect to the ***transition*** from microcrystalline to amorphous Si:H material, showed up ***a shift of the SiH_4 concentration*** for different deposition conditions, as can be concluded from an exact analysis of the deposition

parameters shown in Tab. 2.1.

On one hand a ***decreasing*** d_{gap} has the ***tendency to shift the transition to lower*** SiH_4 concentrations. This general tendency is shown by the SiH_4 concentrations in Tab. 2.1, as the range of the transition changes from the order of 7- 4 % to 4- 1 %, for 20 mm to 9.5 mm, respectively.

On the other hand a ***shift of the transition to a lower*** SiH_4 ***concentration*** was also observed for ***increasing hydrogen dilution*** (this is not shown), e.g. increasing the hydrogen flow rate from 100 to 500 sccm leads to a decrease in the transition SiH_4 concentration from ~ 7 to ~ 2 %. The tendency towards a transition at lower SiH_4 concentrations is also observed for the experimental data of the pressure series, given in Tab. 2.1.

It is known that atomic hydrogen facilitates the microcrystalline growth. Thus, in the case of increased total gas flow rates (very high hydrogen flows), an improved microcrystalline growth has to be expected. However, a shift of the transition to lower silane concentration at higher working pressures using high hydrogen flows means that atomic hydrogen is faster pumped than SiH_4 derivatives in the high-pressure regime (> 1 mbar).

Powder formation was also monitored during the pressure series by visual control. Hereby, a decrease of powder formation was observed when decreasing d_{gap} from 20 to 13 mm. ***At 9.5 mm gap powder formation*** even ***completely vanished*** (see chapter 4.3).

Focussing on the pressure points of the occurrence of powder formation, as noted in Tab. 2.1 powder was observed at a d_{gap} of: 20.0 mm from 2 mbar on, 16.5 mm between 2.5 and 4 mbar, 13.0 mm from 3 to 3.5 mbar, 9.5 mm nowhere in the used pressure regime used (see also chapter 4.3)

Conclusions:

The ***novel cylindrical design of the plasma confinement box*** and a decrease of the ***inter-electrode gap*** down to ***9.5 mm*** allowed us to obtain a deposition regime where not only ***deposition rates of μc-Si:H layers*** on ZnO was ***increased up to about 28 Å/s***, but ***powder formation could be avoided*** at a gap of 9.5 mm; furthermore, the inhomogeneity in thickness was improved (see more chapter 4).

Chapter 3: Development of μc-solar cells in a single-chamber deposition system

The development of μc-Si:H p-i-n solar cells consists in a first step of individual optimisation of all three layers, the p-doped, the intrinsic and the n-doped Si:H layer – as shown in chapter 2. In a second step the assembling of the layers to the solar cell with a further optimisation of the layers within the solar cell structure has to be carried out. In this chapter we focus on the entire solar cell structure with the different layers, their interfaces and the performance of the μc-Si:H solar cell with their problems which are to be resolved.

In the following chapter 3.1 all applied treatments and recipes of the layers will first be introduced.

3.1. Recipes of the Si:H layers and applied treatments of the μc solar cells

The following recipes are the basis for all microcrystalline solar cells that were deposited in the single-chamber deposition system (system "A") used for the present thesis.

3.1.1. ZnO surface pre-treatment

treatment	T_{heater} [°C]	p [mbar]	$\Phi(CO_2)_{ind.}$ [sccm]	$\Phi(H_2)_{ind.}$ [sccm]	$P_{entr.}$ [W]	$f_{excit.}$ [MHz]	t [min.]
CO_2 plasma	200	0.46	10	-	5	70.0	4
H_2 plasma	200	1.0	-	100	50	70.0	10

Tab 3.1: Recipes of ZnO pre-treatment.

Crystallisation favouring treatments had to be introduced due to insufficient Raman

crystallinity factor ϕ_c for the TMB doped p-layers. The application of CO_2 as well as H_2 plasmas allow a subsequently growth of microcrystalline by TMB p-doped Si:H layers of high crystalline volume fraction ϕ_c (> 0.7). Furthermore, higher Raman crystallinity factor ϕ_c allowed a further increase of the doping level towards a higher conductivity.

Similar CO_2- and H_2-interface treatment for growing microcrystalline p-layers within amorphous n-i-p solar cells were described in the Ph.D. thesis of P. Pernet [82]. They are applied there at the i-p interface. Hereby, both interface treatments increase the Raman crystallinity factor ϕ_c of the subsequently grown p-doped μc-Si:H layer.

3.1.2. Recipes of TMB p-doped μc-Si:H layers

p-layer type	T_{heater} [°C]	p [mbar]	$P_{entr.}$ [W]	$f_{excit.}$ [MHz]	$\Phi(TMB)_{ind.}$ [sccm]	$\Phi(SiH_4)_{ind.}$ [sccm]	$\Phi(H_2)_{ind.}$ [sccm]	t [min]	Thickness [Å]
A	200	0.60	20	110	8 - 10	1.00	80.0	3	~200
B	200	0.60	20	110	15.00	1.00	100.0	3	~200
C	200	0.60	5	110	10 – 15	1.0	79 - 74	6	~250

Tab. 3.2: Recipes for p- doped μc-Si:H laye (source-gas: 500 ppm TMB is diluted in H_2).

All these p-doped layers are microcrystalline (verified by Raman spectroscopy for layers grown on ZnO); they show a conductivity which is in the order of 0.5 – 2 S/ cm (measured for layers grown on plain glass substrates). However, an essential handicap of the p-layer deposition is the reproducibility of “IMT standard LPCVD ZnO” (M4). For every run of ZnO the p-layer has to be at least slightly readapted with respect to the thickness. Even standard ZnO seems to vary slightly for its surface roughness. Therefore, comparing μc-Si:H solar cells on ZnO of different runs are not unequivocal and interpretation has to be done cautiously. That’s why a series of solar cells should ideally be deposited on ZnO of the same run.

3.1.3. Treatments after the deposition of the p-doped layer

The treatments listed below focus on the reduction of the crucial cross-contamination of boron at the p-i layer interface (more in chapter 3.2.1). The ***treatments are intended*** to decrease or ***if possible avoid cross-contamination at the p-i layer interface***. Such cross-contamination is suspected to degrade the semiconductor characteristics of the intrinsic μc-Si:H layer.

In the present study we are focussing on two different strategies to avoid boron cross-contamination. In a first approach (treatments a) & b)) the boron is thought to be “eliminated” by “passivation” or covering the previous boron containing layer in the chamber. In a second approach, the p-doped layer is removed from the plasma confinement box by ex-situ gas-etching. However, an ex-situ cleaning process risks introducing further contaminants.

All these treatments can not be applied on the p-layer of the solar cell. Therefore, the substrate has to be stocked during this chamber treatment in the load lock of the system.

3.1.3.1. Chamber passivation by CO_2 plasma passivation:

treatment	T_{heater} [°C]	p [mbar]	$\Phi(CO_2)_{ind.}$ [sccm]	$P_{entr.}$ [W]	$f_{excit.}$ [MHz]	t [min.]
CO_2 plasma	200	0.30	10	20	110.0	3- 30

Tab. 3.3: Recipe of chamber treatment.

The CO_2 plasma is reported to passivate boron. Indeed, no molecular mechanism of the interaction between the plasma decomposed CO_2 and the boron of the p-doped layer was so far proposed in literature. We suspect the carbon during the CO_2 plasma to partially transform the μc-Si:H layer into a Si:C, a silicon carbide. Carbides –silicon carbide as well as boron carbide- are known to have an enhanced mechanical resistance compared to simple silicon. Therefore, the covering p-doped layer (on the box) can be expected to be more resistive to the ion-bombardment -that can affect an off etching.

Note that H_2O is formed during the CO_2 plasma process. In order to decrease H_2O concentration in the chamber – oxygen causes a degradation of the intrinsic layer [34]- the chamber walls were heated and pumped down (after the CO_2 plasma) to a degassing rate of 10^{-5} mbar l/s (reached after ~ 20 min.).

3.1.3.2. Chamber covering layer:

Covering layer	T_{heater} [°C]	p [mbar]	$P_{entr.}$ [W]	$f_{excit.}$ [MHz]	$\Phi(SiH_4)_{ind.}$ [sccm]	$\Phi(H_2)_{ind.}$ [sccm]	t [min]	Thickness [Å]
a-Si:H	200	0.30	10	70.0	10.00	20.0	15	500

Tab. 3.4: Recipe for the covering of the uncharged plasma confinement box.

The amorphous Si:H layer is thought to cover the previously deposited boron doped layer on the plasma confinement box. However, a strong cross-contamination of the amorphous

covering layer itself by etching of the underlying p-layer may not be excluded.

3.1.3.3. Chamber cleaning by SF_6/ O_2 etching gas:

The previously deposited p-doped layer remaining on the plasma confinement box (without the sample) is etched off by ex-situ SF_6/O_2 cleaning in our IPL (Integrated Plasma Limited) 200 E etching system.

Nevertheless, the cleaning gas SF_6 may introduce sulphur contamination. Sulphur easily sublimes at 100°C under high vacuum conditions [57]. Therefore, we can assume that no sulphur contamination would only be obtained for an in-situ etching process in the case of a heated plasma confinement box (T~ 200°C). However, our deposition system did not have any on-line etching gas. We had to clean the plasma confinement box externally. In this case the confinement box is cooled down to room temperature.

Therefore, a sulphur contamination of the cleaned plasma confinement box can be expected (see chapter 3.2).

3.1.3.4. Chamber cleaning by etching gas & covering layer:

1. External SF_6/O_2 cleaning of plasma confinement box (IPL)

2. Covering layer	T_{heater} [°C]	p [mbar]	$P_{entr.}$ [W]	$f_{excit.}$ [MHz]	$\Phi(SiH_4)_{ind.}$ [sccm]	$\Phi(H_2)_{ind.}$ [sccm]	t [min]	Thickness [Å]
a-Si:H	200	0.30	10	70.0	10.00	20.0	15	500

Tab. 3.5: Recipe for the covering of the SF_6 cleaned, unloaded plasma confinement box.

In order to avoid any sulphur cross-contamination at the p-i layer interface, additionally after ex-situ SF_6/O_2 cleaning we cover the unloaded plasma confinement box with an amorphous Si:H layer. Hereby, any potential sulphur contamination is covered.

3.1.4. Recipe of intrinsic μc-Si:H layer in the low pressure regime

T_{heater} [°C]	p [mbar]	$\Phi(SiH_4)_{ind.}$ [sccm]	$\Phi(H_2)_{ind.}$ [sccm]	$c(SiH_4)$ [%]	$P_{entr.}$ [W]	$f_{excit.}$ [MHz]	t [min]	Dep. rate [Å/s]	Thickness [μm]
200	0.70	2.0 – 2.3	25.0	7.4 – 8.4	15	122.04	60	~ 4	1.3 – 1.6

Tab. 3.6: Recipe for intrinsic μc-Si:H layer.

The intrinsic layer is optimized in the μc-Si:H solar cell with respect to the transition to amorphous Si:H; this transition takes place at a SiH_4 concentration between 7.4 and 8.4 % for low pressure regime as specified above.

3.1.5. Recipes of n-doped Si:H layers

p-layer type	T_{heater} [°C]	p [mbar]	$P_{entr.}$ [W]	$f_{excit.}$ [MHz]	$\Phi(PH_3)_{ind.}$ [sccm]	$\Phi(SiH_4)_{ind.}$ [sccm]	$\Phi(H_2)_{ind.}$ [sccm]	t [min]	Thickness [Å]
amorphous	200	0.35	7	70.0	25.0	1.0	25.0	3	~200
μc	200	0.70	10	70.0	36	1.5	58.0	5	~200

Tab. 3.7: Recipes for n-doped μc-Si:H layer (source-gas: 1000 ppm PH_3 is diluted in H_2).

For μc-Si:H p-i-n solar cells both, amorphous as well as μc-Si:H n-doped layers can be incorporated in order to obtain solar cells.

3.2. μc-Si:H solar cells and analysis

The solar cells of the following study were deposited on the basis of the above listed recipes for the different layers and for the special specific treatments.

<u>Results and discussion:</u>

In a ***first phase of development of μc-Si:H p-i-n solar*** cells we achieved the following initial characteristics (Tab. 3.8) .

Hereby, a ***CO_2 plasma treatment (during 3 minutes)*** is used on the empty chamber which is reported to be helpful for a single-chamber process [83] after depositing the p-doped layer. Indeed, ***for amorphous Si:H solar cells*** a ***reduction in collection of blue light in the EQE*** – showing a ***lowered J_{SC}*** - was ***reported for cells having boron contamination at the***

p-i interface, as soon as the strong oxygen contamination is taken away. Hereby, the oxygen acted as compensation-doping to the boron contamination. By the application of a CO_2 plasma passivation of the chamber after deposition of the p-layer the collection of blue light was increased [84]. For μc-Si:H solar cells similar degradation effects of J_{SC} were so far not yet reported.

initial	V_{OC} [mV]	σ_{std}	FF	σ_{std}	J_{sc} [mA/cm^2]	η [%]	σ_{std}
Average of 5 best cells	479	2	0.634	0.010	19.7	6.0	0.1
best cell	481		0.650		19.7	6.2	

Tab. 3.8: Initial characteristics of best μc-Si:H solar cells during the initial development period on the single-chamber system.

After deposition of a ***μc-Si:H solar cell*** a further ***improvement of V_{OC} and FF*** can generally be obtained ***by annealing*** the cell at 180°C for 1h 30 min. under N_2 atmosphere.

However, in the case of the above mentioned solar cell not only an improvement in V_{OC} and FF, but also a ***degradation of the J_{SC} (J_{SC}-degradation)*** is observed (Tab. 3.8), after annealing. Indeed, we can observe on one hand (as expected) an improvement of V_{OC} from 479 to 499 mV and FF from 0.634 to 0.641. On the other hand, very unexpectedly J_{SC} decreases drastically from 19.7 mA/cm^2 down to 13.0 mA/cm^2 (see Tab. 3.8 & Tab 3.9). External quantum efficiency (EQE) measurements show that the ***loss of J_{SC}*** is ***mainly due to a reduction in the collection of blue light.*** Meanwhile, the V_{OC} of these μc-Si:H solar cells seems to be limited to values below 500 mV for i-layers deposited throughout the transition region between microcrystalline and amorphous layers.

annealed	V_{OC} [mV]	σ_{std}	FF	σ_{std}	J_{sc} [mA/cm^2]	η [%]	σ_{std}
Average of 5 best cells	499	4	0.641	0.005	13.0	4.2	0.1
regenerated							
Average of 5 best cells	486	4	0.624	0.009	20.1	6.1	0.1

Tab. 3.9: Annealed and J_{SC}-regenerated characteristics of 5 best μc-Si:H solar cells .

The ***J(V)- and EQE- characteristics*** were ***measured again one month later***.

Hereby, a surprising discovery was made; the degraded ***J_{SC} was regenerated*** during this period of time to 20.1 mA/cm^2. The loss of 6 mA/cm^2 due to the annealing was even more than compensated by 7 mA/cm^2 increase during the course of time (compare Tab. 3.8 & 3.9).

There seems to exist a ***reversible "J_{SC}-degradation ↔ J_{SC}-regeneration" process*** which is

initiated by the annealing process. That kind of reversible process was so far not observed for μc-Si:H solar cells. Its reversibility was confirmed by repeating the annealing on the same sample. Repeated measurements on other μc-Si:H solar cells during the course of time after annealing confirmed as well improvements in J_{SC}.

In order to get an idea of this reversible "J_{SC}-degradation ↔ J_{SC}-regeneration" degradation process we focused on possible problems that are specifically related to our single-chamber process.

The deposition of μc-Si:H solar cells in a single-chamber system seems, thus, to introduce additional problems for the production – compared to cells deposited in multi-chamber systems [11].

In the p-i-n type amorphous-Si:H solar cell especially cross-contamination by boron from the p type doping gas diborane is known to be a serious issue (see also chapter 2.1).

For trimethylboron (TMB) – which is the p type doping gas applied in the present study- potential contamination problems had so far not been reported in relation with μc-Si:H solar cells fabricated in single-chamber deposition systems. Nevertheless, boron cross-contamination basically remains a problem even if TMB is used as doping gas [85]. The treatment of the chamber by a CO_2 plasma passivation is a known method to reduce boron contamination in amorphous Si:H solar cells [83]. It turns out to be only partially successful in our case of μc-Si:H solar cells.

Therefore, ***different chamber treatments are studied in this work***. Hereby, we focused on the following treatments: ***CO_2 plasma passivation*** treatment, ***amorphous Si:H covering layer***, ***in-situ SF_6/O_2 chamber cleaning*** and ***SF_6/O_2 cleaning followed by an amorphous covering layer***.

These processes are applied on the empty chamber and therefore demand to move the substrate out of the process chamber to the load lock. Unfortunately, this is time consuming and therefore an undesirable process step for production.

Other treatments that would basically be possible, but have not been studied in the present work are: (1)Boron passivation by H_2O- [86], (2) NH_3-flush treatments [87] as proposed by UNAXIS for their KAI™ PECVD systems and (3) boron-diffusion barriers [11]. These treatments are applied on the loaded chamber with the solar cell substrate with p-layer and act as interface treatment on the p-doped layer. By this way, the substrate remains heated. No time is needed to heat it up again, when reloading after treatment as in our chamber treatment case. Therefore, these interface treatments are economically more interesting – the whole fabrication process of a solar cell needs less time than the chamber treatments of the present study. Unfortunately, we could not apply these interface treatments during the period of the

study due to hardware limitation on the used single-chamber system.

In a first step, a boron contamination profile of p-i layer interface without any chamber treatment was analysed by SIMS measurements. This was done to obtain an idea of the extent of contamination.

Conclusions:

Annealing revealed ***for μc-Si-H solar cells*** of the first development period not only an ***improvement in V_{OC} to 499 mV and FF to 0.641***, but also a ***degradation of the J_{SC} for the collection of blue light of about 7 mA/cm^2***. However, ***during the course of time the J_{SC} recovers to its initial value***. The present solar cells seem to suffer from a ***reversible "J_{SC}-degradation ↔ J_{SC}-regeneration" degradation process*** which is ***initiated by annealing***. The CO_2 plasma chamber treatment of 3 minutes turns out to be only partially successful.

We do not yet know if a longer CO_2 exposition time gives an advantageous impact on the J_{SC}-degradation behaviour.

-SIMS analysis of untreated p-i layer interface

Experimental:

A sandwich consisting of a of p-doped and an intrinsic μc-Si:H layer was deposited on a mono-crystalline silicon wafer. A p-doped layer of 200 nm was used for this. The p-doped Si:H layer is here 10 times thicker then the one incorporated in the solar cell structure. Therefore, we have the risk of obtaining a higher boron contamination than in the actual μc-Si:H solar cells. In order to avoid any oxygen contamination after deposition, the sandwich was encapsulated by a final amorphous covering layer.

The Secondary Ion Mass Spectrometry (SIMS) depth profiles were performed using a quadrupole instrument (Atomika 4000) at "Institut für Photovoltaik, Forschungszentrum Jülich GmbH" (Germany). Note that the analysis of the SIMS starts from the surface of the sample and continues to the wafer substrate; in our case we see first, the intrinsic layer and second, the p-doped layer. For this reason, one also observes a certain spreading of the boron profile into the following layer after a peak of concentration. This is not an actual indication of boron contamination spreading into the underlying layer, but just a consequence of the SIMS technique (see also chapter 3.2.1 "SIMS Analysis of boron at the p-i interfaces of the different chamber treatments").

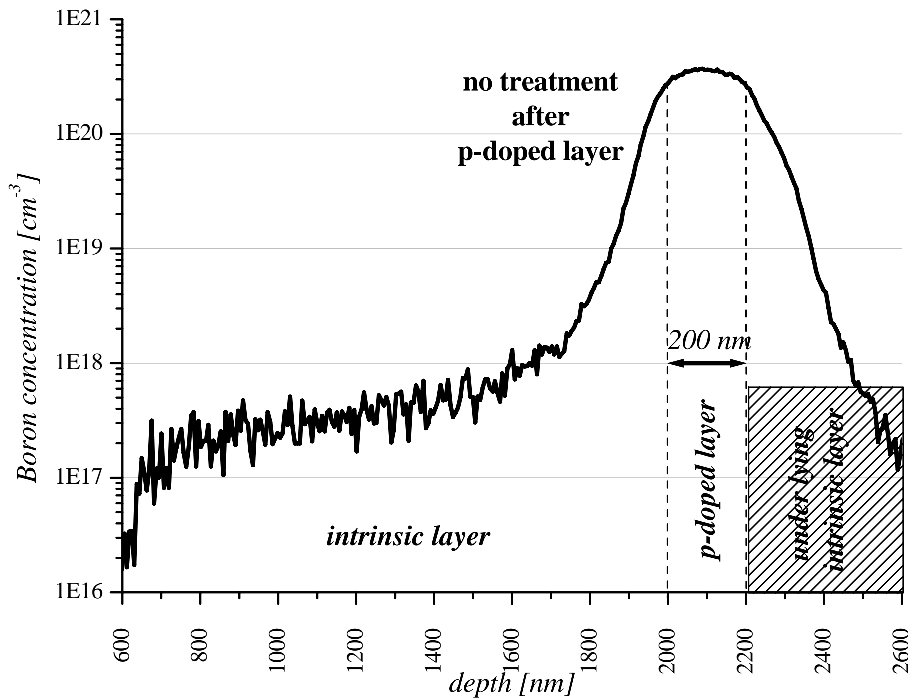

Fig. 3.1: Boron concentration profile by SIMS measurement of p-i layer interface without any chamber treatment.

<u>*Results and discussion:*</u>

The quantified SIMS-profile in Fig. 3.1 reveals a boron concentration of the p-doped layer in the order of 10^{20} cm^{-3}. However, the concentration of boron decreases rather slowly from the p-doped layer into the intrinsic layer down to 10^{17} cm^{-3}. Within the first 400 nm from the interface of the p-doped to the intrinsic layer the concentration decreases only to 10^{18} cm^{-3}. In order to be able to exclude any boron contamination we would need to have a much steeper decrease in concentration – ideally down to 10^{16} – 10^{17} cm^{-3}- already within the first 100 nm from the p-i interface.

Therefore, we can infer, from Fig. 3.1, that we have a crucial boron contamination in the intrinsic layer.

Consequently, a relation between the boron contamination and the observed reversible J_{SC}-degradation phenomenon of the short circuit current (J_{SC}) seems to be quite obvious. A J_{SC}-degradation in external quantum efficiency (EQE) in the blue light was so far not reported for μc-Si:H solar cells. On the other hand, similar effects have been seen in amorphous silicon solar cells (top chapter 3.2).

Another issue for μc-Si:H solar cells seems to be the relatively low V_{OC}. Up to this point of

single-chamber process development, the values obtained for V_{OC} did not exceed 500 mV, whereas from other work 520- 540 mV may be expected. In this connection the boron contamination could possibly play a key role.

In a next step the boron contamination is studied more detailed for the different treatments.

3.2.1. Chamber treatments after the p-doped layer

In this chapter we report on the study of ***different chamber treatments after the deposition of the p-doped layer***; these treatments were carried out in order ***to reduce or even avoid the boron contamination in the subsequent i-layer***.

Hereby, we are focussing on the following processes:

- ***CO_2 plasma passivation treatment***,
- ***Amorphous Si:H covering layer***,
- ***Ex-situ SF_6/O_2 chamber cleaning***,
- ***Ex-situ SF_6/O_2 cleaning followed by an amorphous covering layer***.

In order to check the influence on the subsequent intrinsic μc-Si:H layer, respectively on its boron contamination, we compared the impact of the different chamber treatments on μc-Si:H solar cells. On the other hand, the boron p-i interface profile was checked for every treatment by SIMS analysis (as shown in Fig. 3.1 for the case without any treatment).

3.2.1.1. The impact of different chamber treatments on μc-Si:H solar cell

a) CO_2 plasma passivation treatment

CO_2 plasma passivation of the chamber is known to suppress or at least decrease boron contamination in a subsequently deposited intrinsic amorphous Si:H layer [83]. Therefore, a CO_2 plasma is generally used for single-chamber a-Si:H p-i-n cell deposition.

Applied to μc-Si:H solar cells, a CO_2 plasma of 3 minutes seems not to be that effective for μc-Si:H solar cells (Tab. 3.8 & 3.9) – especially for the J_{SC}- as is reported for amorphous Si:H solar cells. Nevertheless, V_{OC} of close to 500 mV and a FF of 0.641 could be obtained.

The CO_2 plasma chamber treatment of longer exposition times (15 - 30 minutes) turns out

to be quite effective for reducing the J_{SC}-degradation from $\Delta J_{SC} \approx$ 7 mA/cm^2 for 3 minutes down to $\Delta J_{SC} \approx$ 1-2 mA/cm^2 for 15 to 30 minutes. Although the V_{OC} remains below 500 mV the increased CO_2 plasma exposition time (15 – 30 min.) reveals a partial success for the J_{SC}.

In order to check the effectiveness of the CO_2 plasma, we focused on a series in exposition time of the chamber. This is done, by applying it to entire μc-Si:H solar cells, and by SIMS-analysis of the boron depth profiles of the p-i interface (Fig. 3.10 below).

<u>Experimental:</u>

All μc-Si:H solar cells of this series were deposited with the same layers and treatments, except for the CO_2 plasma chamber passivation. Prior to p-i-n cell depositon, the plasma confinement box was externally cleaned by SF_6/O_2 in a IPL (Integrated Plasma Limited) 200 E etching system and afterwards covered with an amorphous Si:H layer of 500 nm thickness to have equivalent initial process conditions.

The ZnO – all ZnO-substrates of the CO_2 series are of type LPCVD M4 36 min. and from the same run to have the same characteristics- was first treated by a CO_2 plasma (Tab. 3.1), followed by an overlaying p-doped μc-Si:H layer (Tab. 3.2 type B). After deposition of the p-doped μc-Si:H layer the substrate was transferred from the process chamber to the "Load Lock".

In a next step, the CO_2 plasma passivation was applied. The parameter varied in this series was the CO_2 plasma exposition time. Hereby, the empty chamber was exposed to a CO_2 plasma at 0.3 mbar with a gas flow of 10 sccm at a plasma excitation power of 10 W for a frequency of 110.0 MHz. The exposition time of the chamber to the CO_2 plasma was varied between 3 and 30 minutes (3/ 15/ 30 min.). A solar cell without (0 min.) any CO_2 treatment after the p-doped layer was deposited, as well as, "reference".

As photoactive layer an intrinsic μc-Si:H was deposited (Tab. 3.6, low pressure, c(SiH_4)= 7.4 %, thickness≈ 1.5 μm at ~ 4 Å/s). The cell was finished with an amorphous n-doped Si:H layer (Tab. 3.7) which then was contacted at the back with a LPCVD-ZnO layer.

After deposition of the μc-Si.H solar cells, they were initially analysed with respect to their J(V)- and EQE-characteristics before being annealed at 180 °C for 1 h 30 minutes. After annealing J(V)- and EQE-measurements were repeated. Due to the discovery of the reversible J_{SC}-degradation phenomenon (see below) the measurements were repeated one month later again. The characteristic values V_{OC}, FF and η shown in the table (Tab. 3.10) correspond to the average value of the five best μc-Si:H solar cells out of a total of 16 cells on a substrate.

Light-soaked degradation of μc-Si:H solar cells then was carried out in our degradation system (Solaronix) under 1 sun A.M. 1.5 for 1400 hours, but only for the cells of 15 minutes CO_2 plasma exposition. Their J(V)- and SR-characteristics (V_{OC}, FF, J_{SC}) were measured initially, after ~100 hours and after 1400 hours.

Further information about the material characteristics (E_{Urbach} and residual absorption α(at 0.8 eV)) of the intrinsic layer within the solar cells was obtained by FTPS measurements (measured after annealing & regeneration).

Results and discussion:

Initially, all solar cells of the series have about the same $V_{OC} \approx$ 400 mV. However, as the CO_2 exposition time increases, the initial J_{SC} increases from 18 to 20 mA/cm^2 (3, 15, 30 min.). Thus, we can initially observe an improvement of J_{SC} for increasing CO_2 exposition time. By the application of a CO_2 plasma the FF increases as well from 0.42 (0 min.) to ~ 0.52 (3, 15, 30 min.).

After annealing and an J_{SC}-regeneration time (see Fig. 3.4 a) of one month duration the μc-Si:H solar cells without (0 min.) any CO_2 plasma treatment still reveal very poor characteristics (Tab. 3.10). The V_{OC} is below 360 mV and the fill factor (FF) is inferior to 0.40. Nevertheless, the external quantum efficiency reveals a reasonable short circuit current density (J_{SC}) of 19.3 mA/cm^2 (for 0 V bias voltage).

Measured directly after the annealing, the performance of the cells without CO_2 plasma treatment was even worse: V_{OC} < 200 mV, FF < 0.40 and J_{SC}< 11 mA/cm^2. Especially, the J_{SC} decreased during the annealing by 8 mA/cm^2 down to 10.4 mA/cm^2. One month later the regenerated J_{SC} was 19.3 mA/cm^2.

A ***μc-Si:H solar cell without any chamber treatment after the p-doped layer suffers from poor V_{OC} and FF values as well as under*** a so far not known ***J_{SC}-degradation phenomenon*** provoked by subsequent annealing (and partially recovered after regeneration over the course of time at room temperature).

t_{CO2} [min.]	state (mean values 5 best cells)	Voc [mV]	FF	J_{sc} [mA/cm^2]	η [%]	E_{Urbach} [meV]	α (0.8 eV) [cm^{-1}]
0	initial	392	0.422	18.6	3.08	40.1	0.00829
	annealed	183	0.353	10.5	0.67		
	regenerated	358	0.385	19.4	2.67	48.5	0.02083
3	initial	426	0.539	19.2	4.41		
	annealed	402	0.472	15.0	2.86		
	regenerated	440	0.579	19.8	5.03	46.6	0.01708
15	initial	414	0.521	18.9	4.09		
	annealed	451	0.570	17.0	4.38		
	regenerated	453	0.604	18.8	5.17	47.4	0.01292
30	initial	390	0.527	20.6	4.24		
	annealed	452	0.584	19.5	5.16		
	regenerated	440	0.586	20.7	5.33	40.6	0.00894

Tab. 3.10: Characteristics of μc-Si:H solar cells for the CO_2 plasma passivation series.

After annealing the μc-Si:H solar cells revealed for an increasing exposition time of the CO_2 plasma , as shown in Fig. 3.2, a significant improvement of the V_{OC} from ~200 mV towards 450 mV and for the FF from ~0.4 towards 0.58 ; the latter values being obtained for a CO_2 plasma of 30 min. By increasing the CO_2 exposition time, the values of V_{OC} and the FF slightly improved (see Fig. 3.2).

The influence of the annealing on the values of J_{SC} is drastic. Immediately after annealing an influence of the increasing CO_2 plasma exposition time was obvious; the of the J_{SC} ranges from ~11 mA/cm^2 for zero minutes of CO_2 plasma towards 20 mA/cm^2 for 30 minutes of CO_2 plasma (see also Fig. 3.5). In comparison, the initial as well as the regenerated J_{SC} values only vary in the range between 19 and 20 mA/cm^2. Even though, the regenerated values of J_{SC} seem not to be strongly influenced by the CO_2 plasma, the best current is achieved for a plasma exposition time of 30 minutes.

Focussing on the regenerated characteristics – measured one month later- the V_{OC} remained stable at ~450 mV for the CO_2 treatments of 15 and 30 minutes (Tab. 3.10). On the contrary, an increase was observed for no CO_2 treatment as for and 3 minutes of CO_2 plasma. However, in the case of no CO_2 treatment these values remained below their initial values.

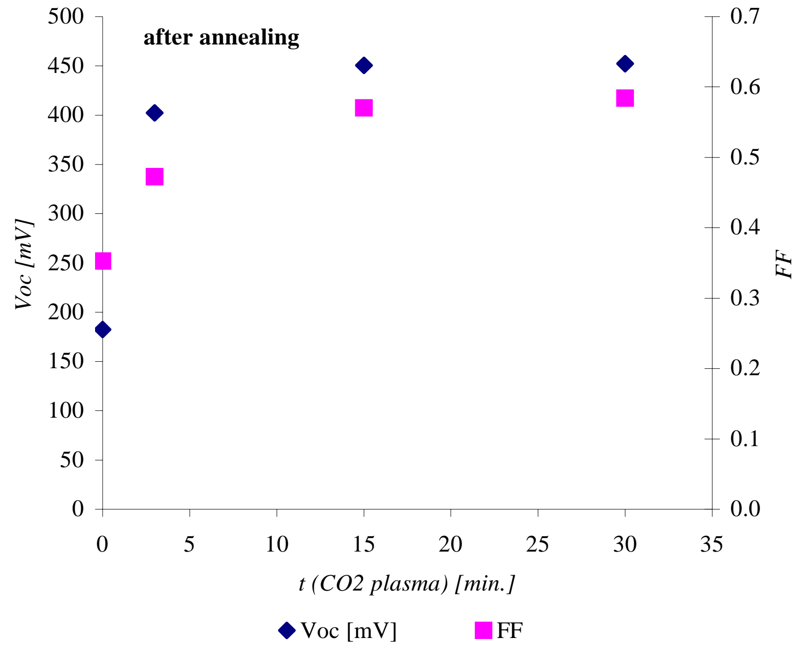

Fig. 3.2: Influence of the exposition time of the CO_2 plasma on V_{OC} and FF values immediately after annealing (see also Tab. 3.11).

Longer CO_2 treatment of (≥) 15 minutes seems to be crucial for µc-Si:H solar cells deposited in single-chamber so as to attain stable values of V_{OC} and FF.

Nevertheless, the V_{OC} remained below 500 mV even though we deposited the microcrystalline intrinsic Si:H layer in the transition regime ($c(SiH_4)$= 7.4 %). Higher SiH_4 concentrations suddenly revealed amorphous V_{OC} values above 600 mV, but no values between 500 and 600 mV - transition zone between µc- and a-Si:H- could be obtained.

In order to understand the loss in V_{OC}, FTPS measurements were carried out on the solar cells of the CO_2 exposition series (see Tab. 3.10). Hereby, the series reveals for µc-Si:H solar cells after annealing and regeneration an improvement of the residual absorption α(0.8 eV) from 0.02 to 0.009 cm^{-1} for increasing CO_2 plasma exposition time from 0 to 30 minutes. The evolution in Fig. 3.3 b) reveals for increasing exposition time a linear decrease in defect density – represented by the residual absorption α(0.8 eV). A decrease in defect density signifies less recombination centres and therefore can reduce the loss in short circuit current density J_{SC}. The evolution of the Urbach Energy (E_{Urbach}) shows as well a strongly decreasing tendency from 50 to 40 meV for an increasing CO_2 plasma exposition time. In other work at our institute, good µc-Si:H solar cells with V_{OC} > 500 mV were only reported for E_{Urbach} < 38 meV [50]. E_{Urbach} is an indicator of band tail states and is increased, as the atomic disorder increases. Indeed, the disorder strongly increases E_{Urbach} when rising from 40 to 50 meV.

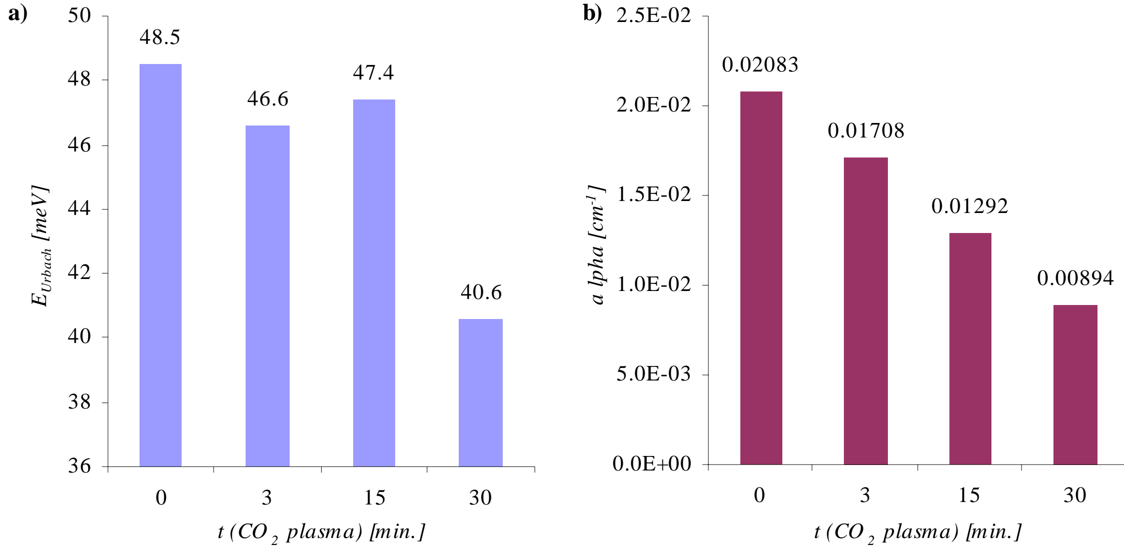

Fig. 3.3: Characterisation by FTPS: a)E_{Urbach} b)residual absorption α(at 0.8 eV) measured after annealing & regeneration.

Initially, the µc-Si:H solar cells without CO_2 plasma revealed surprisingly low defect and band tail state characteristics before annealing (Tab. 3.10). The defect density reveals an increase, observed by the absorption α(0.8eV), from 0.0083 cm^{-1} to 0.0208 cm^{-1} by annealing. ***That kind of increase which even remains for the defect density after regeneration was also observed for the band tail states.*** E_{Urbach} increased from 40 meV to 48 meV (Tab. 3.10) by annealing and remained however that high even after regeneration. So these are the defects determining the efficiency.

The solar cells attained for 30 min. of CO_2 plasma exposition a value of E_{Urbach} of 40.6 meV after annealing and regeneration; these cells clearly have within the CO_2 series the best performance of 5.2 % efficiency with a V_{OC} of 452 mV, a FF of 0.58 and a J_{SC} of 19.5 mA/cm^2 - even after annealing. After their regeneration the J_{SC} re-increased to 20.7 mA/cm^2 and the FF went on improving up to 0.59.

However, the values of V_{OC} for these cells still do not exceed 500 mV, as indeed it does not, either, for any solar cell of this study so far.

Initially, the µc-Si:H solar cells without any treatment attained a surprisingly good E_{Urbach} of 40.1 meV. Indeed, V_{OC} and FF values are already very poor initially (Tab.3.10) and even degrade much more by annealing to an efficiency of 0.7 % with a V_{OC} of 183 mV, a FF of 0.35 and an J_{SC} of 10.4 mA/cm^2. By regeneration, the J_{SC} increased again to 19.3 mA/cm^2 as well as V_{OC} and FF which were slightly improved again – however, the E_{Urbach} remained high at 48 meV (Tab. 3.10).

In order to obtain low defect density and little band tail states even after annealing, 30 minutes – or maybe even longer- of CO_2 plasma is needed.

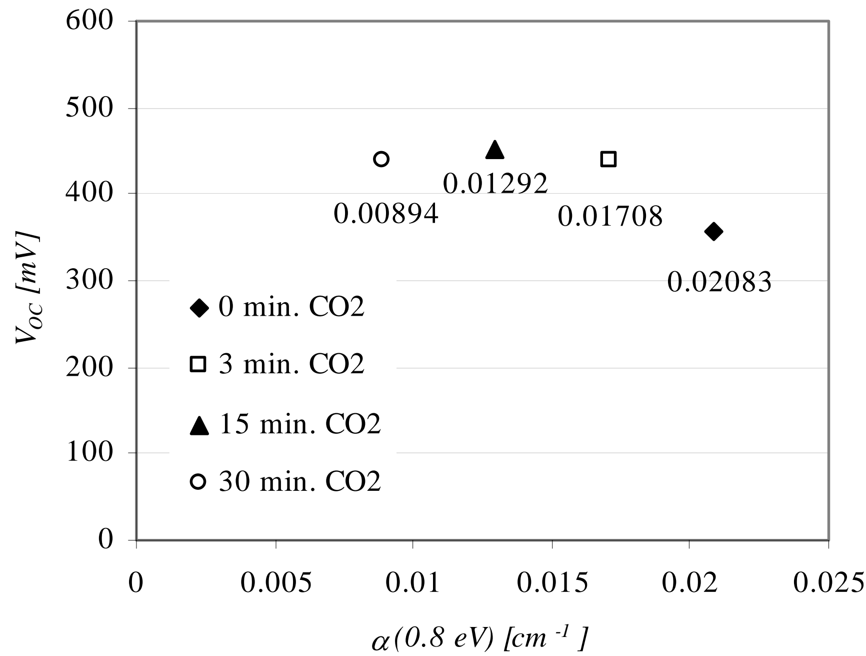

Fig. 3.4: V_{OC} vs. α(0.8eV) for the CO_2 plasma series (after annealing and regeneration).

Although a CO_2 plasma was applied, boron contamination at the p-i interface into the intrinsic layer is suspected to be still too high (see chapt. 3.2.1.2). Hereby, the boron might play a key role in the limitation of the V_{OC}- value.

In Fig. 3.4 we have plotted the values of V_{OC} obtained after annealing and regeneration as a function of defect-related absorption α(0.8eV). Exposure to CO_2 plasma decreases the value of α(0.8eV), i.e. decreases the density of defects acting as recombination centres, with increasing deposition time. V_{OC} is also increased by exposure to CO_2 plasma, but remains more or less constant for exposure times between 3 and 30 minutes. This means that other factors (not assessed by evaluating α(0.8 eV) by FTPS) are probably now limiting V_{OC}. One of these factors could be the defect density near the p-i interface. These defects are suspected to be created by boron impurity.

The phenomenon of J_{SC}-degradation by annealing and subsequently J_{SC}-regeneration is well illustrated by the external quantum efficiency curves of Fig. 3.5. Here, EQE is shown for three samples (without/ 0 min., 3 min. & 15 min.) of the CO_2 plasma chamber passivation series.

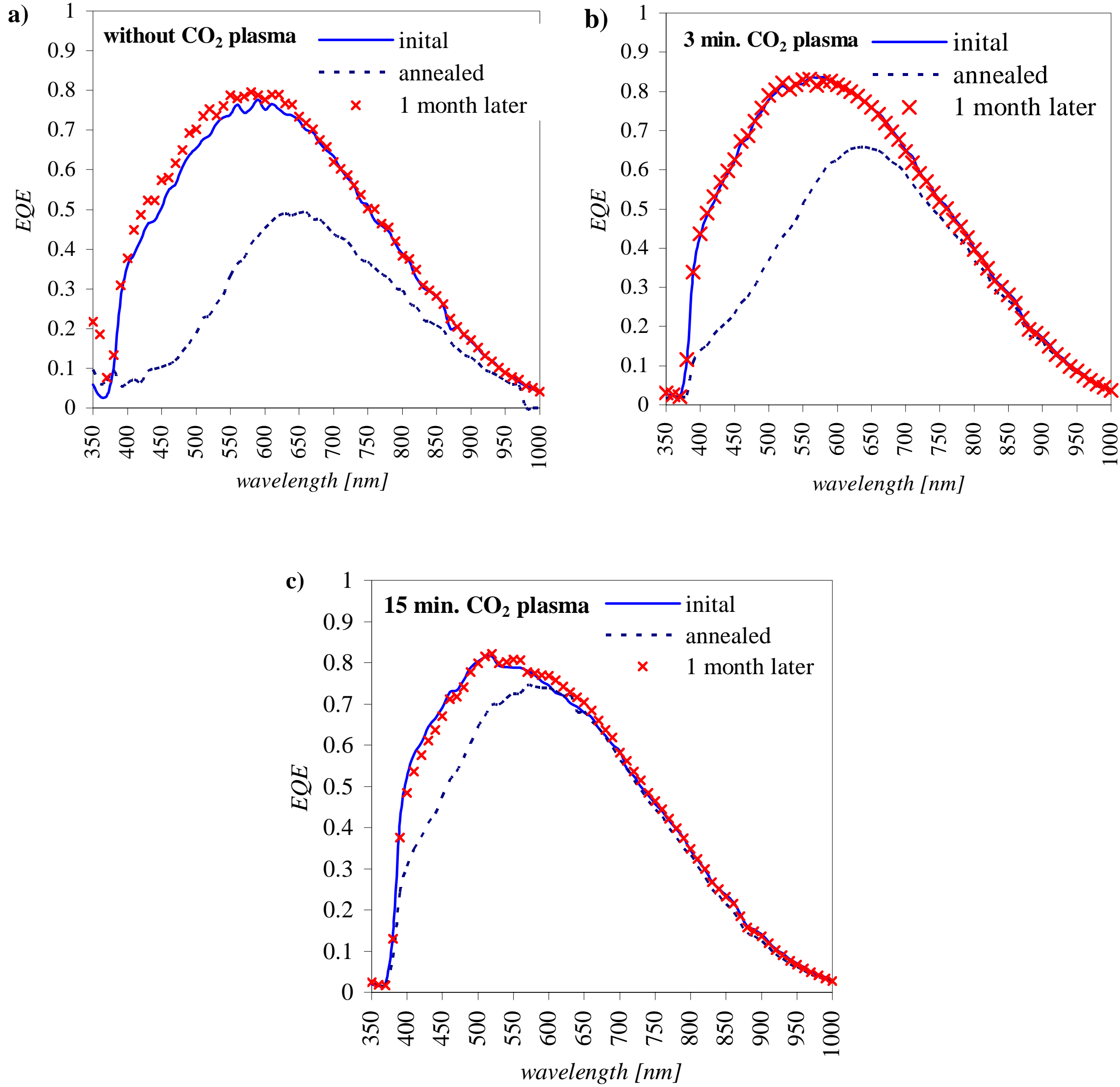

Fig. 3.5: External Quantum Efficiency of μc-Si:H solar cells a) without, b) with 3 min., and c) with 15 min. CO_2 plasma chamber passivation.

Illuminated from the p-doped side, the initial EQE revealed J_{SC} values of about 19 mA/cm^2 for all cells in this series (Tab. 3.11). However, after annealing of the solar cells, the J_{SC} decreased from $J_{SC\ initial} \approx 19$ mA/cm^2 down to $J_{SC\ annealed} \approx 11 – 19$ mA/cm^2 (Tab. 3.11).

The different degradation behaviours can be clearly seen in the EQE curves. The longer the exposition time of the chamber to the CO_2 plasma was, the less is the degradation. For the case without CO_2 plasma the degradation of the EQE spectrum ranged over the whole spectrum from 350 to 950 nm. However, the most important loss in current density (of totally ~ 8 mA/cm^2) is observed herein the range of blue to green light. Increasing CO_2 exposition time to 3 or even 15 minutes reduced the losses to the spectral range of 350 to 600 nm and ΔJ_{SC} to 4 and 2 mA/cm^2, respectively.

The opposite evolution introduced by annealing on V_{OC} and FF which were partly improved (Tab. 3.10) and on J_{SC} that strongly degraded, pointed to a crucial, common issue for all the solar cells that were so far produced in the single-chamber system of this work.

The cells were stocked then in their closed plastic boxes under atmospheric conditions in the dark. One month after annealing, the J(V)- and EQE-characteristic measurements were repeated.

As stated, the repetition of the EQE-measurements after a month of stocking, revealed a re-increase of J_{SC}. The $J_{SC\ annealed}$ of 11 – 19 mA/cm^2 increased to 19 -20 mA/cm^2 (Tab. 3.11 $J_{SC\ regenerated}$). The values of $J_{SC\ regenerated}$ attained again the initial J_{SC}-values of our μc-Si:H solar cells before annealing.

$t_{CO2\ exposition}$ [min.]	$J_{SC\ initial}$ [mA/cm^2]	$J_{SC\ annealed}$ [mA/cm^2]	$J_{SC\ regenerated}$ [mA/cm^2]
0	18.6	10.4	19.3
3	19.2	15.0	19.8
15	18.9	17.0	18.9
30	20.6	19.5	20.7

Tab. 3.11: J_{SC} evolution for "J_{SC}-degradation ↔ J_{SC}-regeneration" behaviour, for different CO_2 plasma exposition times (0/ 3/ 15/ 30 min.).

Illuminated from the p-doped side, the EQE reveals a drastic loss in current collection after annealing compared to the initial collection. In the course of the time in the dark at RT this loss in J_{SC} was then regenerated without doing anything but stocking the solar cell. This observation leads us to the suspicion that we have a reversible process which is activated by the high temperature (180°C) of the annealing and undergoes a back reaction at room temperature.

We were interested to see whether similar degradation behaviour takes place under illumination as under annealing. In order to verify this we exposed the μc-Si:H solar cells with the 15 minutes CO_2 plasma treatment to a "1 sun light-induced degradation test" (A.M. 1.5) for 1400 hours. The light-induced degradation (Tabl. 3.12) confirmed for the first 140 hours a behaviour as already known from the annealing process; the V_{OC} and FF were increased while J_{SC} decreased from ~19 down to ~16 mA/cm^2. However, after 1400 hours of degradation the J_{SC} had been regenerated again to ~18.5 mA/cm^2. V_{OC} and FF stabilized after 1400 h at values which are 5 - 10 % above the initial values before degradation.

The phenomenon of J_{SC}-degradation is therefore not only a key issue which is introduced by annealing, but it is observed also by the exposition to the sun, as shown by the light-induced degradation experiment of table 3.12. For long time exposition (1400 h) the J_{SC}-degradation

seems to stabilize the J_{SC} value to a value which nearly corresponds to the initial current.

state	V_{OC} [mV]	σ_{std}	FF	σ_{std}	J_{sc} [mA/cm^2]	η [%]	σ_{std}
initial	443	7	0.558	0.025	**19.0**	4.69	0.25
138 h degradation	476	5	0.605	0.009	**16.2**	4.67	0.06
1400 h degradation	465	8	0.603	0.014	**18.4**	5.17	0.19

Tab. 3.12: J(V)- and SR-characteristics of A.M. 1.5 degraded μc-Si:H solar cell (15 min. CO_2 plasma)

However, the daily cycle of less than 12 hours sun light exposition would maintain the J_{SC}-degradation under real day light conditions.

Conclusions:

Summarizing we can observe that a CO_2 plasma passivation of the chamber improved the J_{SC}-degradation due to the annealing but could not completely avoid it. The residual absorption α(0.8 eV) reveals a decreasing defect density -fewer recombination centres- as well as E_{Urbach} which shows less band tail states for increasing CO_2 plasma exposition time. Nevertheless, V_{OC} stabilized at low values (400 – 450 mV) under the influence of increasing CO_2 plasma exposition time. J_{SC}-degradation by light induced degradation by one sun at A.M.1.5 is as well observed in the initial phase. Therefore, the CO_2 plasma alone can not be the solution to overcome the J_{SC}-degradation issue.

b) Comparison of different chamber treatments after the p-doped layer

After the previous, unpromising study on the influence of CO_2 plasma treatments –neither the J_{SC}-degradation phenomenon nor the issue of V_{OC} limitation could be completely resolved – a comparison between the CO_2 plasma treatment and three further, different chamber treatments was run directly with μc-Si:H solar cells.

These four different chamber treatments applied after the deposition of the p-doped layer were, thus:

- ***CO_2 plasma passivation treatment of 30 min.***
- ***Deposition of amorphous Si:H covering layer***
- ***Ex-situ SF_6/O_2 chamber cleaning***
- ***Ex-situ SF_6/O_2 chamber cleaning & amorphous covering layer***

Experimental:

The series of comparison of the different treatments is based on μc-Si:H solar cells which were deposited with the same layers and treatments, except for the chamber treatment mentioned above.

The ZnO (type LPCVD M4 36 min., all of the same run) was first treated by a CO_2 plasma (Tab. 3.1), followed by an overlaying p-doped μc-Si:H layer (Tab. 3.2 type C). After deposition of the p-doped μc-Si:H layer the substrate was transferred from the process chamber to the "Load Lock" chamber.

In a next step, either a CO_2 plasma (Tab. 3.3), an amorphous Si:H layer covering layer (Tab. 3.4), an ex-situ SF_6/O_2 cleaning in a IPL (Integrated Plasma Limited) 200 E etching system or the combination of ex-situ SF_6 cleaning and a-Si:H covering layer was applied to the chamber, followed by chamber pumping and heating of the sample.

As photoactive layer an intrinsic μc-Si:H layer was then deposited (Tab. 3.4, $c(SiH_4)$= 7.75 %). The p-i structure was completed with a microcrystalline n-doped Si:H layer (Tab. 3.5) which then was back contacted with a LPCVD-ZnO layer.

As already done for the previous CO_2 series, the μc-Si:H solar cells were measured by determining their J(V)- and EQE-characteristics: initially, after annealing and one month later. The characteristic values V_{OC}, FF and η shown in the tables (Tab. 3.13- 3.14) correspond to the average value of the five best μc-Si:H solar cells out of 16 cells on a substrate; the standard deviation (σ_{std}) of the corresponding parameter is also given (for the 5 best cells). Finally, the solar cells were also characterized by arising defect density (residual absorption α(0.8 eV)) and their disorder of the band tail states (E_{Urbach}) of the intrinsic layer, by FTPS.

Results and discussion:

The plasma confinement box certainly needs an additional treatment after the deposition of the p-doped layer so as to avoid boron contamination of the i-layer and obtain reasonable IV- and EQE-characteristics for a μc-Si:H solar cell. This was shown above in the CO_2 series (previous section). We can assume that boron contamination of the i-layer has two impacts on the solar cell. On one hand we observe a reversible degradation of the J_{SC} in the blue light in the EQE curves, and, on the other hand, the V_{OC} value was so far limited to values under 500 mV. Therefore, we will focus on V_{OC} and J_{SC} when evaluating the different treatments. Initially (dark grey bars in Fig. 3.6), for neither treatment the μc-Si:H solar cells exceed 500 mV. Nevertheless, clear differences can be seen for the V_{OC} (Fig. 3.6, top). The two SF_6/O_2 treatments seem to be of advantage to attain high V_{OC} of 480 to 490 mV.

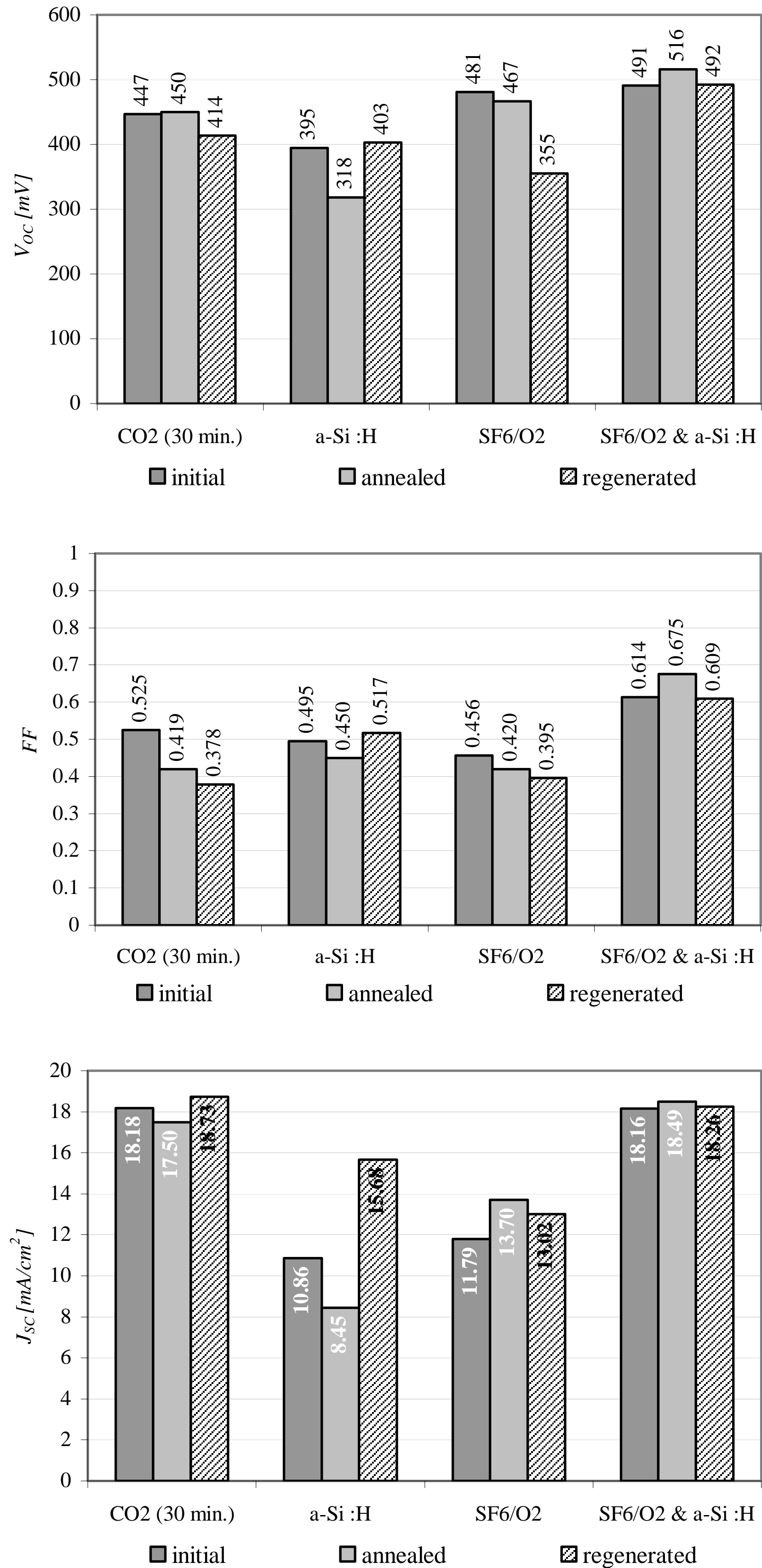

Fig. 3.6: Values of V_{OC} (top), FF (middle) and J_{SC} (bottom) for the different chamber treatments initially (dark grey), after annealing (grey) and after regeneration (hushed).

The CO_2 treatment as well as the amorphous Si:H covering layer lead to rather low V_{OC}- values of ~450 mV and ~400 mV, respectively.

However, by comparing FF (Fig. 3.6 middle) and J_{SC} (Fig. 3.6 bottom) for the two SF_6/O_2 treatments one clearly sees the advantage of combined SF_6/O_2 treatment with an additional a-Si:H covering layer.

The best initial values of 491 mV for the V_{OC}, a FF of 0.614 and a J_{SC} of 18.16 mA/cm^2 obtained thereby lead to an average efficiency of the five best μc-Si:H solar cells of 5.5 ± 0.1 % for the "SF_6/O_2 & a-Si:H covering layer" treatment.

The FF and J_{SC} of the simple SF_6/O_2 treatment without a-Si:H covering layer lead to the lowest initial FF values as well as to a very poor J_{SC} of only ~12 mA/cm^2 – in the initial state. In a first assumption based on the initial values of V_{OC} and FF values we can already guess that the combination of "***SF_6 & a-Si:H covering layer treatment" is the best treatment*** followed by the CO_2 plasma of 30 min. On the other hand, neither the simple SF_6-treatment nor the a-Si:H covering layer alone seem to be very promising treatments due to their poor performance especially for FF (Fig. 3.6 middle) and J_{SC} (Fig. 3.6 bottom).

In general, annealing (grey bars in Fig. 3.6) is expected to improve V_{OC} and FF, as well as the J_{SC} of a μc-Si:H cell.

In our case, we can ***only observe an improvement of V_{OC} to 516 mV, of FF to 0.675 and of J_{SC} to 18.49 mA/cm^2 for the combination of SF_6/O_2 cleaning & a-Si:H treatments***.

In the case of the CO_2 plasma treatment the V_{OC} remained after annealing stable at ~ 450 mV; however, a decrease in FF of ~20 % from 0.525 to 0.429 and in J_{SC} from 18.2 to17.5 mA/cm^2 were observed during annealing. The FF (Fig. 3.6 middle) and J_{SC} (Fig. 3.6 bottom) for the simple SF_6/O_2 treatment as well as for the a-Si:H covering layer revealed after annealing both very poor FF of less than 0.45 and weak J_{SC} below 14 mA/cm^2.

The most extreme degradation by annealing was observed in the case of the amorphous Si:H covering layer alone. The V_{OC} decreased below 320 mV and the initially weak J_{SC} even decreased further to 8.5 mA/cm^2.

The μc-Si:H solar cells of the simple SF_6/O_2 treatment showed also slight decrease in V_{OC} and FF due to annealing. J_{SC} increased here during annealing to 13.7 mA/cm^2, a value which is, however, still very low for a μc-Si:H solar cell. Only the V_{OC} remained at reasonable value of ~ 470 mV after annealing.

treatment	state	V_{OC} [mV]	σ_{std}	FF	σ_{std}	J_{sc} [mA/cm^2]	η [%]	σ_{std}
CO_2(30min.)	initial	447	9	0.525	0.053	18.2	4.27	0.47
	annealed	450	12	0.419	0.059	17.5	3.30	0.54
	regenerated	414	18	0.378	0.045	18.7	2.94	0.44
a-Si :H	initial	395	18	0.495	0.022	10.9	2.12	0.19
	annealed	318	69	0.450	0.010	8.5	1.21	0.28
	regenerated	403	30	0.517	0.043	15.7	3.28	0.51
SF_6/O_2	initial	481	11	0.456	0.011	11.8	2.58	0.06
	annealed	467	19	0.420	0.006	13.7	2.69	0.10
	regenerated	355	6	0.395	0.004	13.0	1.83	0.04
SF_6/O_2 & a-Si :H	initial	491	7	0.614	0.005	18.2	5.48	0.09
	annealed	***516***	*4*	***0.675***	*0.008*	***18.5***	***6.44***	*0.06*
	regenerated	492	7	0.609	0.015	18.3	5.48	0.16

Tab. 3.13: Summary of J(V)- and EQE-characteristics of μc-Si:H solar cells for the different chamber treatments (initially, after annealing & after regeneration).

In the course of time we observe two different behaviours for the regenerated μc-Si:H solar cells (hashed bars Fig. 3.6). On one hand we can observe the recovering of the J_{SC} and on the other hand we have again a degradation of V_{OC} and FF. The first observation confirms the reversible J_{SC}-degradation phenomenon for all treatments except the "SF_6/O_2 cleaning & a-Si:H covering layer" which does not suffer from the reversible "J_{SC}-degradation ↔ J_{SC}-regeneration" phenomenon. The degradation in V_{OC} and FF after annealing is an already known behaviour of the influence of atmospheric conditions to a not encapsulated μc-Si:H solar cell. Surprisingly ***in the case of SF_6/O_2 etching alone, solar cell characteristics are poorer after regeneration***. We ***attribute this to sulphur contamination***, a process that appears to have a long-term detrimental effect. This is seen as a strong effect in the case of SF_6/O_2 etching alone.

In order to have an idea about the ***defect density***, i.e. about the ***density of the recombination centres*** (i.e. states with energies in the centre of the band gap), ***FTPS analysis*** was carried out on initial (Fig. 3.7 grey bar) solar cells as well after annealing (Fig. 3.7 hatched bar).

Comparing the initial V_{OC} values for the different chamber treatment the corresponding E_{Urbach} as well as the residual absorption α at 0.8 eV revealed the same tendencies (Tab. 3.13). The ***lowest defect density*** represented by a ***residual absorption of 4.73 ×10^{-3} cm^{-1}*** was ***obtained for the combination treatment "SF_6 & a-Si:H covering layer"***, while the highest

defect density by 4.13 $\times 10^{-2}$ cm^{-1} was found for the simple a-Si:H covering layer. The CO_2 treatment revealed in correspondence with the V_{OC}–values (Tab. 3.13) a slightly lower defect density (Fig. 3.7 b) compared to the simple SF_6 treatment. The ***lowest disorder in the band tail*** defined by a ***E_{Urbach} of 38.0 meV*** is achieved as well ***for the combination treatment "SF_6 & a-Si.H covering layer"***, while the CO_2 treatment reveals a slightly higher degree of disorder with 39.4 meV. The simple treatments of the "a-Si:H covering layer" as well as the "SF_6/O_2" however revealed the highest disorders with 43.8 meV and 44.8 meV, respectively. For
μc-Si:H solar cells with V_{OC} > 500 mV, α (0.8 eV) < 0.01 cm^{-1}, E_{Urbach} of 35 – 38 meV have generally reported, for other series of μc-Si:H cells [50].

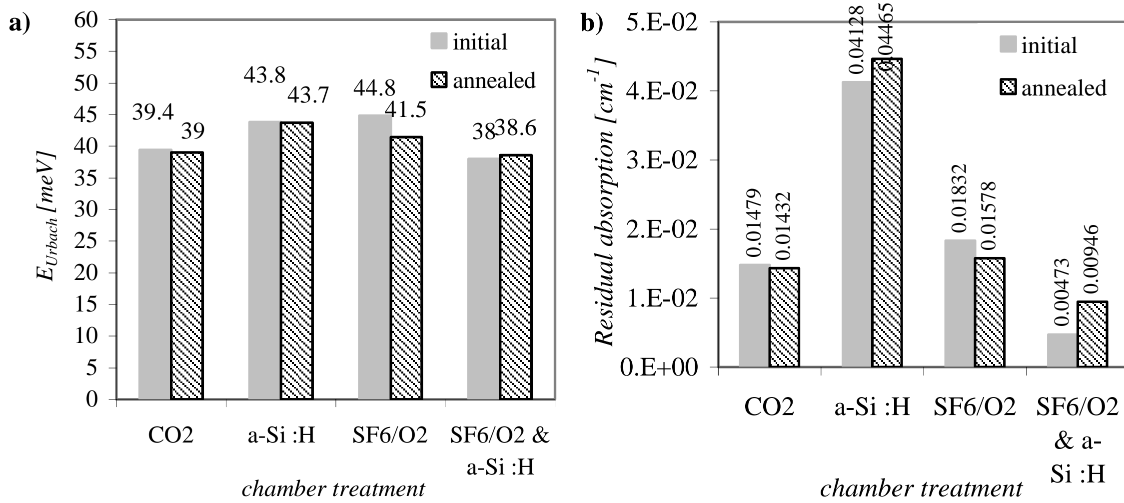

Fig. 3.7: a)Defect characteristics E_{Urbach} and b) residual absorption α(0.8 eV) for the different chamber treatments at initial state (grey bar) and after annealing (hatched bar).

During annealing, as shown by FTPS measurements, there are only slight variations of E_{Urbach} and of residual absorption α(0.8 eV), and these variations are within the measurement errors. The order of efficiency for the chamber treatments remains the same.

In order to search for a relation between V_{OC} and α(0.8 eV), the V_{OC} of the μc-Si:H solar cells is plotted in Fig. 3.8 as function of the defect density α(0.8 eV) for the different chamber treatments, for the annealed state. We see here that, ***the best V_{OC} of 516 mV of the "SF_6 & a-Si:H covering layer" treatment is related to the lowest defect density of 0.0095 cm^{-1}***.

Fig. 3.8 clearly ***assigns the highest V_{OC} to the lowest defect density***. The V_{OC} then linearly decreases with increasing defect density, e.g. the worst V_{OC} of 318 mV obtained with the "a-Si:H covering layer" treatment is linked to the highest defect absorption of 0.04465 cm^{-1}. Hereby, we observe a linear dependence of high V_{OC} values and low defect absorption values, as known from literature [50].

In this case, we assume the increase in defect density has to be somehow related to an increase in impurities in the intrinsic Si:H layer. The defects which act as recombination centres are here very probably related to the boron contamination. The boron contamination of the intrinsic Si:H layer as shown for the p-i interface without any chamber treatment (Fig. 3.1) corroborates this suspicion.

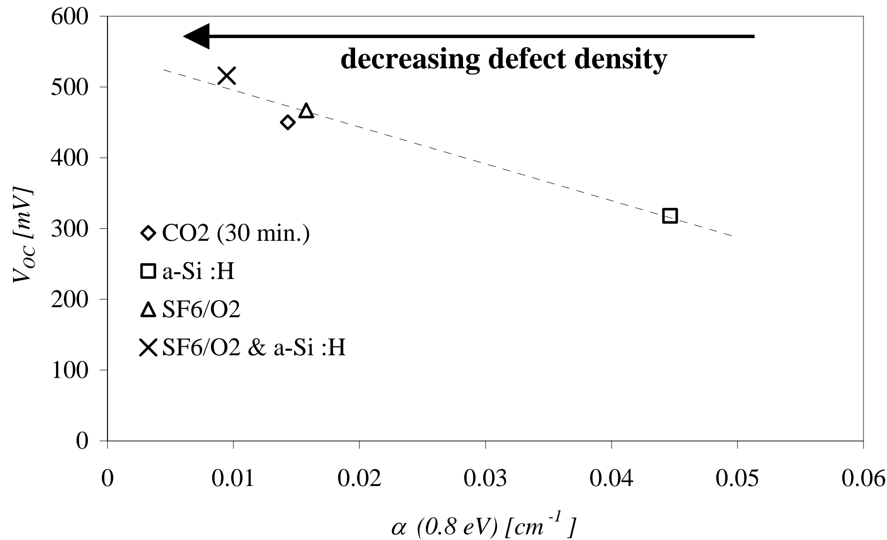

Fig. 3.8: V_{OC} vs. residual absorption α(0.8 eV) for the different chamber treatments after annealing.

The relation of V_{OC} vs. α(0.8eV n Fig. 3.8 allows us to attest a ranking of the chamber treatments with respect to V_{OC} and defect density: the best treatment is the "SF_6 cleaning & a-Si:H" followed by the "CO_2 plasma of 30 minutes" and the "SF_6/O_2 cleaning"- they have the same effect on the V_{OC}- and the least effective treatment is the simple "amorphous Si:H covering layer".

Conclusions:

The ***"SF_6 & a-Si:H covering layer"*** after the deposition of the p-doped μc-Si:H layer is the ***only treatment*** of this series which ***fulfils the requirement of obtaining a V_{OC}-value higher 500 mV and of almost completely avoiding the reversible "J_{SC}-degradation ↔ J_{SC}-regeneration" phenomenon.***

For all other treatments ("SF_6 cleaning", "CO_2 plasma" (15/ 30 min.) and simple "a-Si:H covering layer"), V_{OC}–values remain below 500 mV and the J_{SC}-degradation is not avoided. However, the J_{SC}-degradation can be decreased – but unfortunately, not avoided- by the application of a CO_2 plasma of 15 - 30 min.

In the case of the ex-situ "SF_6 cleaning" of the plasma confinement box done here, only unfavourable conditions (T< 100°C during the cleaning process) could be chosen (see chapter 3.1 c). Therefore, an additional sulphur contamination of the box has to be expected here.

We focus now in the next section on the analysis of boron contamination at the p-i interface.

3.2.1.2. SIMS-analysis of boron at the p-i interfaces for the different chamber treatments

The previously shown solar cell characteristics strongly vary for the four different chamber treatments applied after the deposition of the p-doped layer. The ***only effective treatment to avoid "J_{SC}-degradation ↔ J_{SC}-regeneration"*** behaviour and to ***obtain a V_{OC} of more than 500 mV is the "SF_6/O_2 chamber cleaning & amorphous covering layer"***. Due to the boron SIMS-profile shown in Fig. 3.1 we do suspect boron to play a key role as impurity for the existing issues.

In order to have an idea of the influence of the various chamber treatments on any ***boron cross-contamination*** a boron concentration ***profile of the p-i interface*** was ***examined by SIMS*** for all applied treatments.

Chamber treatments applied after the deposition of the p-doped layer were (the recipes are given in chapter 3.1):

- ***no chamber treatment***
- ***CO_2 plasma passivation treatment of 3 and 30 min.***
- ***amorphous Si:H covering layer***
- ***ex-situ "SF_6/O_2 chamber cleaning"***
- ***ex-situ "SF_6/O_2 chamber cleaning & amorphous covering layer"***

Experimental:

The p-i interfaces of the Si:H layers were always deposited as double p-i sandwich structure on mono-crystalline silicon wafer (wafer-p-i-p-i). After the deposition of the p-doped layer one of the chamber treatments was applied. However, even though the p-i structure corresponds in all steps to a μc-Si:H solar cell, the applied p-doped Si:H layer is here 10 times thicker (200 nm) than the p-layer incorporated in an actual solar cell device.

Therefore, we run the risk of finding here higher boron contamination than in actual μc-Si:H solar cells.

In order to avoid any oxygen contamination after deposition, the layer structure was encapsulated by a final amorphous Si:H covering layer of 500 nm thickness.

Our main interest in the SIMS-analysis is focussed on the variations in the boron concentration profile at the p-i interface.

The analysis of the samples was done at "Institut für Photovoltaik" of the "Forschungszentrum Jülich GmbH" in Germany. Secondary Ion Mass Spectrometry (SIMS) depth profiles were performed there using a quadrupole instrument (Atomika 4000). The residual gas pressure in the SIMS analysis chamber was $< 2 \times 10^{-10}$ Torr. Primary Cs^+ and O_2^+ ions at near-normal incidence with an energy of 6 keV were used. Electron beam bombardment has been used for charge compensation during the O_2^+ bombardment. Stylus surface profile meter (Dektak 6M) was used to measure the sputtered crater depths.

In order to compare the different treatments, the decay of the boron concentration at the p-i interface was studied. Hereby, two different approaches were used.

In the first, the geometric distance for a reduction of boron concentration of three magnitudes ($d_{decr.B}$ (10^3)) is determined by evaluating the boron profile (dotted lines in figures) and its decrease within the intrinsic layer. The second approach focuses on the gradient in boron concentration at the interface itself.

The steeper the gradient of the profile at the p-i interface is, the less the cross-contamination is in the intrinsic Si:H layer. The gradient was then related to V_{OC}–values of the μc-Si:H solar cells, as obtained with the different treatments.

Results and discussion:

In order to have an idea of the boron impurity in the intrinsic layer, we previously deposited a p-i structure without any treatment on the empty chamber after the p-doped Si:H layer.

In Fig. 3.9 the ***"no treatment"*** case is shown on the left. The boron concentration of the p-doped layer is about 3×10^{20} cm^{-3}. The ***decrease*** of three magnitudes (from the dashed line) down to 10^{17} cm^{-3} takes place ***through the whole intrinsic layer*** (> 1000 nm). That kind of shallow continuous decrease from the p-i interface through the whole layer is certainly unfavourable – a steep and abrupt step-like decrease is what one wants at the beginning of the i-layer.

An ideal ***boron profile of a p-i interface*** - without any boron contamination- is expected to

show a ***steep, abrupt step-like decrease from the maximum concentration down to the minimum concentration of the intrinsic layer- the stronger the gradient the better***. If the decay happens in a shallow exponential like or even linear like manner, as shown in Fig. 3.9 for the "no treatment" case (left), the intrinsic layer has to be considered as contaminated by boron.

Therefore, the ***p-i interface without any treatment revealed*** (as shown in Fig. 3.9 left) ***a boron contamination for the whole intrinsic layer.***

Based on the known boron contamination (Fig. 3.9 left) in the case of "no treatment", we then examined the treatments mentioned above to check their utility to avoid or reduce boron contamination.

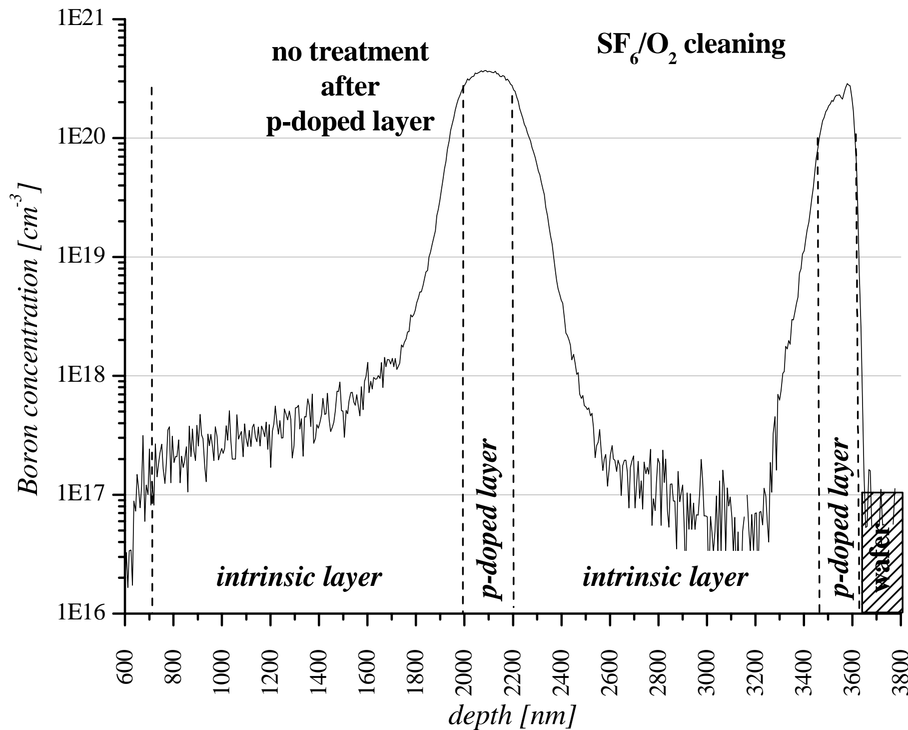

Fig. 3.9: Boron concentration depth profile of a double p-i structure for the case of "no treatment" (left) and "SF_6/O_2 cleaning" treatment (right). (sandwich-structure: intrinsic layer/ p-doped layer/ intrinsic layer/ p-doped layer/ wafer).

In a next step the boron contamination was studied by SIMS depth profile (Fig. 3.10) for the application of ***CO_2 plasma treatments*** of 3 and of 30 minutes duration.

The boron concentration of both the p-doped layer is about 1×10^{20} cm^{-3}. Comparing the CO_2

plasma of 3 (left) and 30 minutes (right) duration a first impression reveals a slightly lower minimal boron concentration of ~1×10^{17} cm^{-3} in the intrinsic layer for 30 minutes.

For the "3 minutes CO_2 plasma" a decrease by a factor of 10^3 to its lowest boron contamination is only attained for 1000 nm of intrinsic layer – the whole intrinsic layer is needed- in contrast to the plasma of 30 minutes which attains a stabilisation at a boron concentration of ~1×10^{17} cm^{-3} after 500 nm in the intrinsic layer – half of the intrinsic layer (Tab. 3.14).

Briefly, a ***long CO_2 plasma (≥ 15 min)*** seems to be ***advantageous in reducing boron cross-contamination***.

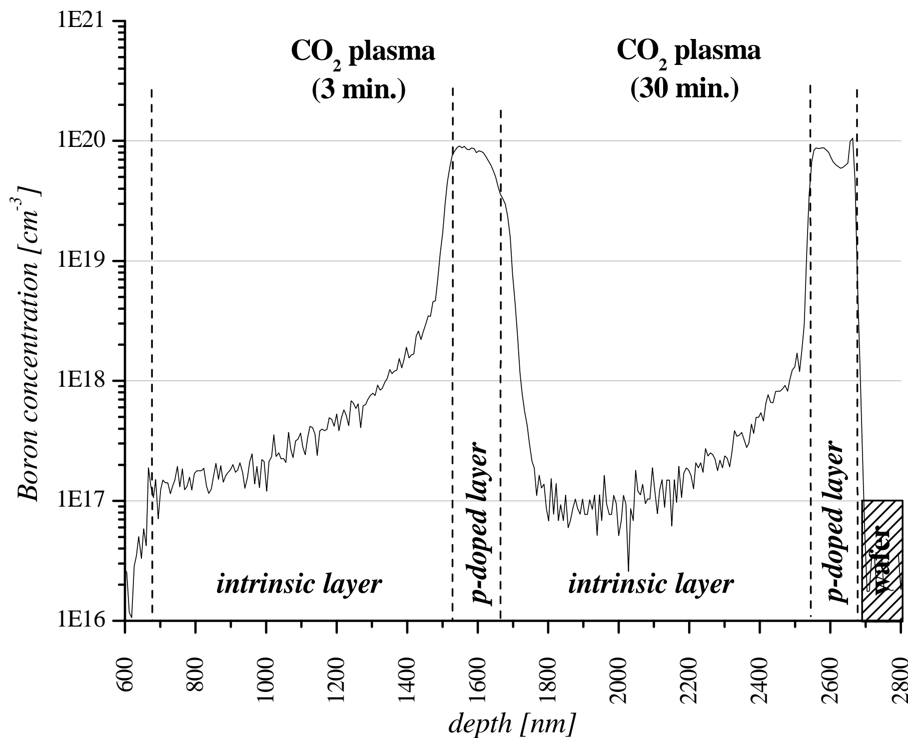

Fig. 3.10: Boron concentration depth profile of a double p-i structure for CO_2 plasma treatments of 3 min. (left) and of 30 min. (right). (sandwich-structure: intrinsic layer/ p-doped layer/ intrinsic layer/ p-doped layer/ wafer).

Nevertheless, the boron concentration decrease remains for 3 (Fig. 3.10 left) as well as 30 minutes (Fig. 3.10 right) rather shallow as shown by the gradients in Fig. 3.13. The boron gradients of the boron concentration only increased from 0.021 to 0.039 cm^{-3}/nm for the increase in time from 3 to 30 min and the boron decrease still ranges into half of the intrinsic layer. Comparing the defect density α(0.8 eV) for 3 and 30 minutes of exposition times

(Fig. 3.3), 30 minutes CO_2 treatment leads to α(0.8 eV) values of 0.0143 cm^{-1} i.e. to a lower defect density than for 3 minutes, where α(0.8 eV) is 0.0171 cm^{-1}. The defect density reveals the same tendency as observed for the decrease in boron concentration over three magnitudes and the increase in the gradient.

A CO_2 treatment of 30 minutes duration is favourable.

Nevertheless, the ***CO_2 plasma treatment does not allow us to completely avoid a boron cross-contamination*** even with 30 min. exposition time.

In a next step the influence of an ***amorphous Si:H covering layer*** to cover the boron-doped Si:H layer on the plasma confinement box is examined. The SIMS-profile of Fig. 3.11 (on the left) shows the p-i interface with an applied a-Si:H covering layer of ~500 nm thickness on the chamber after deposition of the p-doped layer.

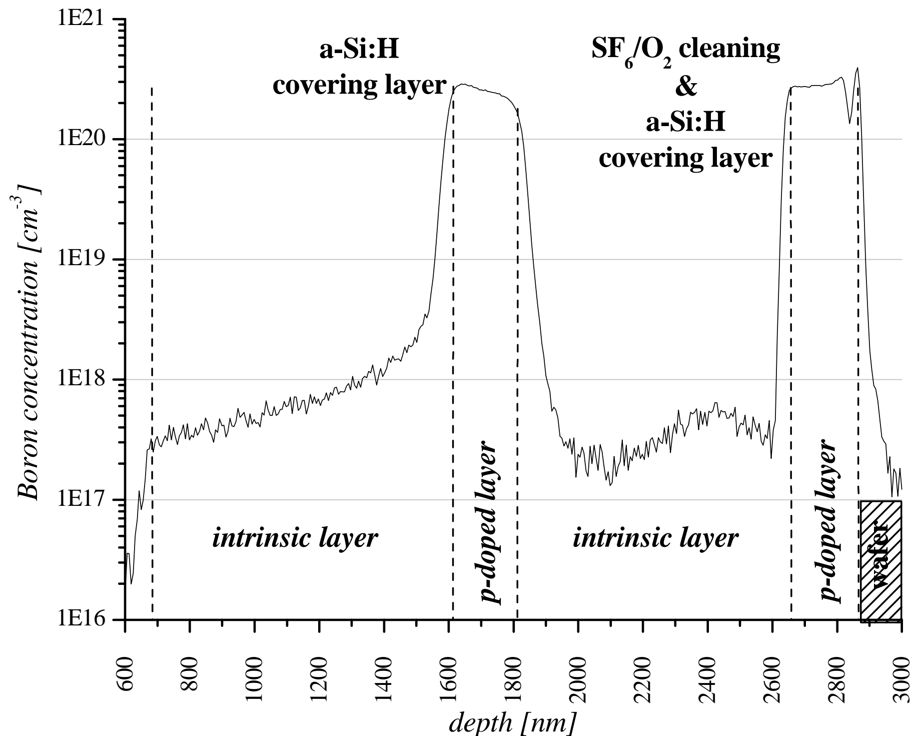

Fig. 3.11: Boron concentration depth profile of a double p-i structure for "a-Si:H covering layer" (left) and "SF_6/O_2 & a-Si:H covering layer" treatment (right). (sandwich-structure: intrinsic layer/ p-doped layer/ intrinsic layer/ p-doped layer/ wafer).

The maximum boron concentration of the p-doped layer is ~3×10^{20} cm^{-3}. The boron concentration gradient at the interface of 0.020 cm^{-3}/nm seems to be quite steep for the first 100 nm. However, the decrease over three magnitudes only takes place trough the whole intrinsic layer of 1000 nm. The decay of boron concentration down to 3×10^{17} cm^{-3} only

decreases exponentially (Fig. 3.11 left). There is no step-like boron profile at the p-i interface.

Therefore, an ***a-Si:H covering layer of ~500 nm thickness can not be considered as a suitable chamber treatment to avoid boron cross- contamination***.

However, a thicker covering layer -which was not examined in this study - might be able to avoid boron cross-contamination.

The previous two chamber treatments were thought to passivate or cover the boron to avoid any boron cross-contamination.

In the ***following treatment the p-doped layer on the plasma confinement box is etched off*** by an ex-situ treatment.

In a first approach the plasma confinement box is ***cleaned ex-situ by SF_6/O_2***. Hereby, the SIMS boron concentration profile of Fig. 3.9 (right) was obtained. The boron concentration decreases exponentially (or linearly in the log. plot), from the maximum concentration of 2×10^{20} cm^{-3} to a minimum concentration of 5×10^{17} cm^{-3} in the intrinsic layer, within the first 300 nm at the p-i interface – corresponding to a reduction of boron concentration by a factor of almost 10^3. Although, the boron concentration shows in Fig. 3.9 step-like profile for the first 300 nm after the p-i interface, the initial zone – ~1/3 of the total thickness of the intrinsic Si:H layer- remains contaminated by boron. The SIMS profile reveals the so far strongest boron concentration decrease at the p-i interface to the lowest boron concentration-value in the intrinsic layer. However, the corresponding boron gradient at the p-i interface is only 0.013 cm^{-3}/nm (Tab. 3.14) and from that point of view this is the least effective of all treatments. Thus, strong boron contamination at the interface has to be presumed in this case.

Furthermore, an additional sulphur contamination which can be incorporated due to unfavourable "SF_6/O_2 cleaning" conditions (see 3.1 c & chapter 2.3) might also have a negative influence on solar cells.

A contamination of the interface may also be suspected if one looks at the poor performance of the corresponding μc-Si:H solar cells (see previous paragraph). However, it is so far not known if this poor performance is caused by boron contamination or by sulphur contamination or by any other unknown effect. Therefore, further investigations would be necessary to search e.g. for sulphur which could so far not be detected by the mass spectrometer used for our SIMS-Analysis.

The simple ***"SF_6/O_2 cleaning" treatment is, thus, also not the adequate chamber treatment to avoid boron cross-contamination at the p-i interface completely***.

The last treatment applied in this series is a ***combination of the ex-situ SF_6/O_2 cleaning and the a-Si:H covering layer***. The idea of the combination is on one hand to ***etch off boron***

from the walls and then on the other hand ***to cover any other impurities which might be introduced by the cleaning process***, e.g. sulphur (see chapter 2.3).

The SIMS-profile of Fig. 3.12 (on the right) shows the p-i interface with the applied treatment of ***"SF_6/O_2 cleaning & a-Si:H covering layer"***.

The boron concentration of the p-doped layer is about 3×10^{20} cm^{-3}. The boron concentration profile reveals an abrupt and steep decrease by a factor of 10^3 down to the minimum concentration of ~3×10^{17} cm^{-3} within only ~50 nm from the p-i interface. This steep step-like decrease of the boron concentration reveals the best p-i interface of the series. The steep linear decrease points to a situation where there is no cross-contamination into the intrinsic layer. In that case boron does not disturb the initial part of the intrinsic layer. The combination of "SF_6/O_2 cleaning & a-Si:H covering layer" seems to be the adequate treatment that should be used to overcome a boron cross-contamination.

However, at the depth of 2400 nm in the intrinsic layer a very feeble hump reveals a brief boron concentration increase. We suspect here a slight lift off of boron from the p-doped layer of the substrate by hydrogen etching followed by a reincorporation during the initial growth of the intrinsic layer. Nevertheless, the boron concentration of ~5×10^{17} cm^{-3} remains very low and even decreases further within the i-layer.

The chamber treatment by "SF_6/O_2 cleaning & a-Si:H covering layer" reveals to be the best method of this series to avoid boron cross-contamination into the intrinsic layer.

Chamber treatment	$c_{min.}(B)$ [cm^{-3}]	$d_{decr.B}$ (10^3) [nm]	gradient of c(B) @ p-i interface [cm^{-3}/nm]	Fig.(side)
without	2×10^{17}	>1000	0.080	3.9 (left)
CO_2 3 min.	1×10^{17}	>1000	0.021	3.10 (left)
CO_2 30 min.	1×10^{17}	500	0.039	3.10 (right)
a-Si :H	2×10^{17}	>1000	0.020	3.11 (left)
SF_6	5×10^{16}	300	0.013	3.9 (right)
SF_6 & a-Si :H	2×10^{17}	**50**	0.058	3.11 (right)

Tab. 3.14: Summary of p-i interface characteristics by SIMS-Analysis for the different chamber treatments.

In Table 3.14 all applied chamber treatments are summarized for its boron concentration

profiles. The characteristics are, the minimum concentration of the intrinsic layer $c_{min.}(B)$ and the distance $d_{decr.\ B}$ ranging from the p-i interface into the intrinsic layer to attain a decrease of a factor of 10^3 - in general down to the lowest boron concentration.

The second approach focuses on the gradient of the boron concentration at the p-i interface.

The summary in table 3.14 of distance $d_{decr.B\ min.}$ (10^3) clearly shows that the most abrupt decrease of boron concentration within a distance of only ~50 nm is obtained for the combined treatment of "SF_6 & a-Si:H covering layer". All other treatments show an exponential boron decrease into the intrinsic layer stretching over several hundreds of nanometers before they reach the minimum boron concentration. Among these other treatments, the simple "SF_6/O_2 cleaning" and the CO_2 plasma treatment of 30 minutes led to the most reasonable cross-contamination distances into the intrinsic layer $d_{decr\ B}$ of 300 and of 500 nm, resp. Nevertheless, they seem to be insufficiently efficient to overcome the boron contamination issue as shown by the unsatisfactory μc-Si:H solar cell characteristics obtained with them.

Conclusions:

The ***analysis of the SIMS*** examinations reveals that the ***combined chamber treatment "SF_6/O_2 & a-Si:H covering layer"*** is the only treatment in this series to fulfil the requirement of ***avoiding boron cross-contamination***.

3.2.1.3. Correlation of defect density determined from μc-Si:H solar cell characteristics with the results of the SIMS-analysis

As previously shown for the μc-Si:H solar cell characteristics and the SIMS p-i interface analysis the different chamber treatments reveal similar tendency for the different chamber treatments.

In a last approach, the results of the SIMS-Analysis were correlated with the corresponding defect absorption α(0.8e V) obtained within μc-Si:H solar cells.

In Fig. 3.13, the defect density α(0.8 eV) of each μc-Si:H solar cell is plotted as function of the corresponding boron gradient (Tab. 3.14) for the various treatments. For the "SF_6/O_2 cleaning & a-Si:H covering layer" treatment, this correlation diagram clearly reveals the highest boron gradient and the lowest defect absorption. All other treatments show shallower boron gradients as well as higher defect densities.

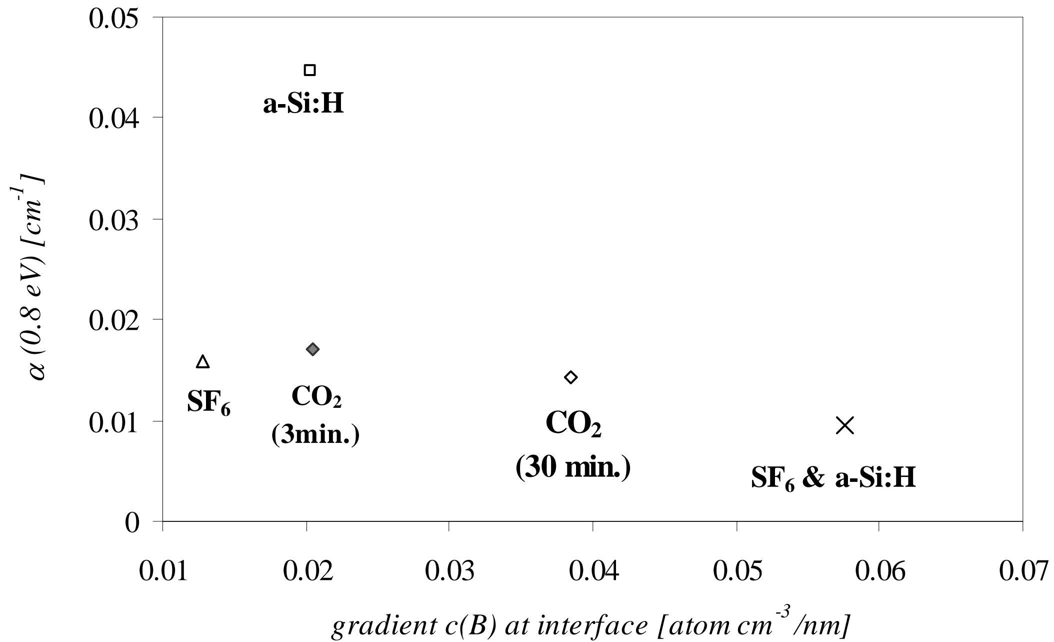

Fig. 3.13: Correlation of defect absorption α(0.8 eV) of μc-Si:H solar cells (after annealing) with the boron gradient obtained from the SIMS-Analysis on the p-i interfaces, for all chamber treatments applied here.

The boron gradient at the p-i interface may therefore be considered to be a qualitative indicator which gives a general tendency for a good or poor interface, but not a quantitatively precise prediction factor for solar cell performance. Indeed, boron contamination is not the only factor that influences i-layer quality but only one of them.

3.2.1.4. Proposed mechanism for the "J_{SC}-degradation ↔ J_{SC}-regeneration" phenomenon and V_{OC} limitation

In the following paragraph we try to explain a ***"J_{SC}-degradation ↔ J_{SC}-regeneration" phenomenon*** as well as the observed limitation in V_{OC} by proposing a reasonable microscopic mechanism.

The reversible "J_{SC}-degradation ↔ J_{SC}-regeneration" phenomenon was so far seen as a ***deterioration of the external quantum efficiency (EQE) curve in the blue wavelength range and as reduction of short-circuit current-density J_{SC}***, observed ***immediately after the annealing step*** (Fig. 3.5 a- c). In the course of time (some days or weeks later after storage in the dark, at room temperature) however, J_{SC} had recovered and the initial external quantum efficiency curve in the blue wavelength range was re-established.

Almost all μc-Si:H solar cells made in the present work (shown in Tab. 3.10 & 3.13-15) suffer from the following ***meta-stable, reversible cycle***:

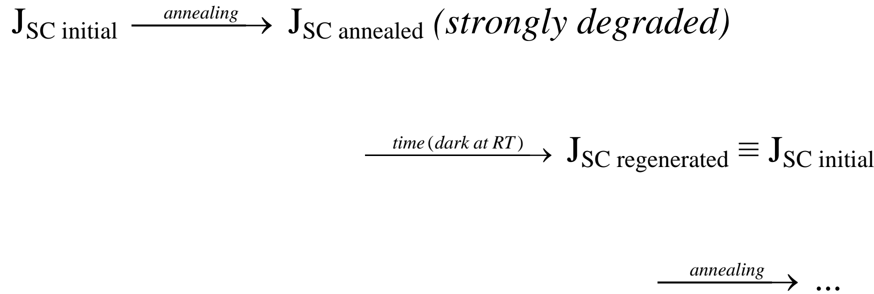

The fact, that the degradation is measured only after an annealing process at 180°C of 1h 30 minutes leads us to the suspicion that the annealing is the initiating process. The reason of the degradation behaviour is, however, so far not known. Nevertheless, the annealing temperature seems to be a key parameter.

The observed phenomenon appears for the blue light when illuminating from the p-doped side for the external quantum efficiency-measurement (EQE). On the other hand, illumination from the n-doped side reveals no or only little loss in EQE for blue light (400- 550 nm), i.e. the current collection behaviour remains in this case the same before and after the annealing process.

Up to now, this kind of phenomenon had not been reported in literature for μc-Si:H solar cells, and we only know that it must be based on a "self curing effect" at room temperature.

We may therefore assume to have a ***reversible reaction with a thermal equilibrium*** (Equ. 3.1) that favours a neutral state – where J_{SC} is not degraded- at room temperature and in the course of the time. Furthermore, the effect must be related to the p-i interface due to its strong effect on EQE only when measured in the case of the illumination from the p-doped side.

Obviously, ***boron seems to play a key role in this issue of "J_{SC}-degradation ↔ J_{SC}-regeneration" behaviour***. The only μc-Si:H solar cell without any substantial J_{SC}-degradation is obtained for the ***"SF_6/O_2 & a-Si:H covering layer" chamber treatment*** (Tab.3.13 -15). The ***SIMS boron profile*** of that treatment reveals indeed for this case a ***steep linear decrease in boron concentration within 50 nm at the p-i interface*** (Fig. 3.12 right).

Note that p-i interfaces of amorphous Si:H solar cells are also reported to be problematic, although no reversible degradation effects of this type are mentioned [88].

For monocrystalline p-n junction silicon solar cells (wafer-based solar cells), however, this kind of a reversible degradation process is reported. [89].

In this case, an ***iron-boron (FeB) complex equilibrium reaction*** (Equ.3.1) is the origin of the problem. The ionized, dissociated form of the interstitial iron (i), $Fe_i^{0/+}$ acts as recombination centre for the carriers, e.g. electons. The complex formation depends on a thermal equilibrium (see also Equ. 3.2) for the following reaction.

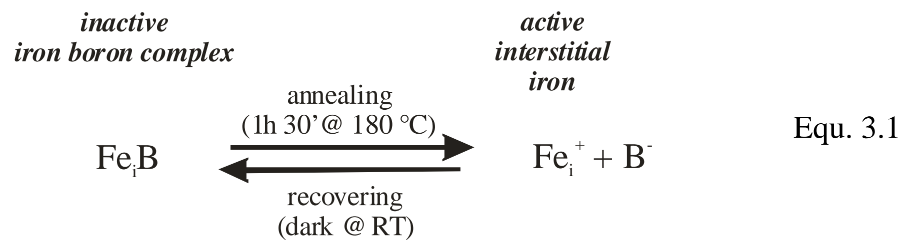

Equ. 3.1

At room temperature the thermodynamic equilibrium (Equ. 3.1 and 3.2) ***of monocrystalline solar cells is dominated by the recovering process***. Therefore, the reversible degradation effect is a minor effect for the monocrystalline Si solar cells. On the other hand, it is a major effect for μc-Si:H solar cells, because of the much higher boron concentrations of the intrinsic layer.

For the μc-Si.H solar cells the degree of dissociation of the inactive FeB complex that occurs at 180 °C – during the annealing process- producing active Fe_i^+ and B^- is not known. However, it seems to have a very strong effect on the efficiency of μc-Si:H solar cells, as shown in this work.

In our case of the single-chamber μc-Si:H cell deposition the boron concentration in the intrinsic μc-Si:H layer is of the order 10^{17}- 10^{18} cm^{-3}. Amorphous Si:H solar cells are known not to be as sensitive to impurities, while μc-Si:H solar cells seem to be much more sensitive to impurities such as oxygen, as already documented by Torres et al. [34] or boron, as shown in this work.

The impact of the FeB contamination on monocrystalline solar cell performance is reported to depend on boron concentration and temperature [90]. They suggest a mechanism of thermally activated dissociation of an impurity-boron pair – in our case the impurity is Fe-; the impurity being much more effective at causing electron-hole recombination once it dissociates from the boron.

In thermal equilibrium:

$$\frac{N_{FeB}}{N_{Fe}\,N_B} = C_{diss}\exp\left(\frac{E_b}{kT}\right) \qquad \text{Equ. 3.2}$$

where $N_{FeB} = N_{total} - N_{Fe}$ is the complex concentration, N_B the boron concentration, E_b the binding energy of the FeB complex and C_{diss} is a constant factor. The binding energy (E_b) of the FeB complex is reported to be in the range of 0.58 eV to 0.65 eV. [91] The dissociation degree of the FeB complex is reported to be for monocrystalline silicon up to 30 % at 200°C [90]. However, this process, "leading to a few % degradation of the efficiency of the device", is reversible even within 12 h at room temperature. Therefore, for monocrystalline Si solar cells this must be considered only as a weak, minor effect.

Furthermore, there is strong evidence for the ***existence of two charge states of the FeB complex in silicon***, as summarized by Istratov et al. [92]. One state of FeB occurs as an acceptor level at $E_V + 0.1$ eV, and the other as a donor level at E_C -0.29 eV.

In boron-doped p-type silicon of a monocrystalline ***p-n junction silicon solar cell two different acceptor levels for iron*** have been reported to play a role in this thermal equilibrium. On one hand, the acceptor level lies at $E_V + 0.1$ eV in the case of an inactive FeB complex and on the other hand for the dissociated states of Fe_i^+ and B^- an acceptor level $Fe_i^{0/+}$ lies at $E_V + 0.4$ eV corresponding to an active, ionized interstitial iron (Fe_i^+).

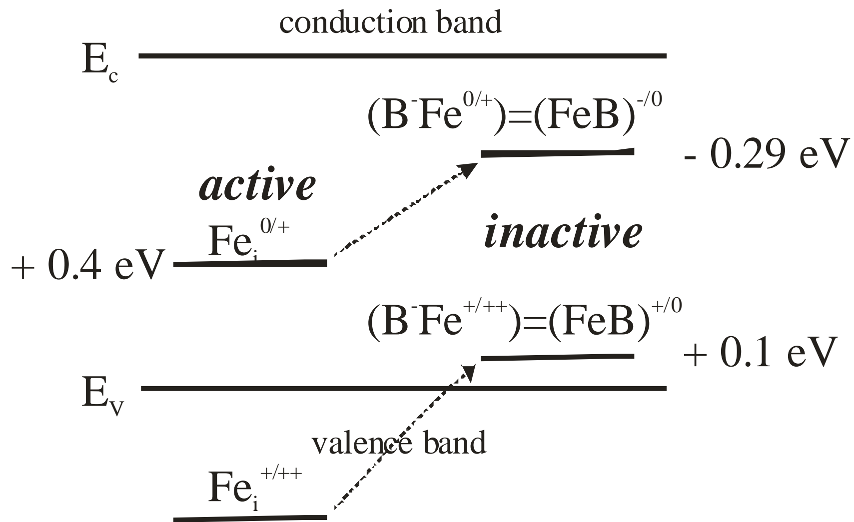

Fig. 3.14: A diagram of the energy levels of interstitial iron (active as recombination centre) and of the FeB complex [93],[94],[95]. This diagram is based on the ionic model of iron-boron pairs.

In our case we ***suspect*** a ***Fe_iB-complex to be formed by coulomb interaction of the boron impurities at the p-i layer interface*** during the initial deposition of the intrinsic μc-Si:H layer at ~200°C. The presence of boron could provoke polarisation and even ionisation of

interstitial iron Fe_i within the μc-silicon matrix.

The origin of the iron impurity is likely the production equipment. It is very difficult or even impossible to completely eliminate iron contaminants, especially due to the fact that the deposition system consists of iron containing parts, e.g. of gas lines, vacuum-chamber made of stainless steel.

The boron source, however, is in our case (μc-Si:H solar cells) either the p-doped layer itself or a boron cross-contamination of the p-doped layer covered plasma confinement box walls. Hereby, an incorporation of boron into the intrinsic layer occurs by desorption – boron lift-off during the initial i-layer growth by reaction with atomic hydrogen to B_2H_6 (see 2.1) or a physically etching of boron might be possible.

During the annealing process at 180 °C the FeB complex dissociates then into its ionic compounds boron (B^-) and interstitial iron (Fe_i^+). From then on, the Fe_i^+ acts as a quencher of incident photons by its introduced acceptor level at $E_V + 0.4$ eV (Fig. 3.14) [96] [92].

The thermal equilibrium (Equ. 3.1) favours the Fe_iB complex formation at room temperature. Consequently, the active quenching Fe_i^+ ions react in the course of the time after annealing – by Coulombic attraction- with B^- ions to form again the inactive Fe_iB complex. Meanwhile, the deep acceptor level of $Fe_i^{0/+}$ at $E_V + 0.4$ eV disappears, while the Fe_iB complex introduces an acceptor level $FeB^{+/0}$ at $E_V + 0.1$ eV, and a shallow donor level $FeB^{-/0}$ at E_C -0.29 eV (see Fig. 3.14).

Both interstitial iron atom Fe_i^+ and FeB complex pairs are considered to be recombination centres in the case of monocrystalline Si. However, the recombination activity of FeB pairs at low injection levels is about 10 times lower than that of interstitial iron Fe_i^+ [97],[98]. In the ***ionized active state Fe_i^+ one of the three spin unpaired electrons is in a bonding orbital*** (Fig. 3.15 left), while the ***unpaired electrons in the inactive FeB complex state are only in the anti-bonding orbitals of the iron*** (Fig. 3.15 middle). Due to the much ***higher electron affinity of bonding orbitals*** compared to anti-binding orbitals, ***Fe_i^+ is a much stronger recombination centre*** than the iron within the complex FeB.

Assuming that FeB pair lead to recombination, the J_{SC} and the EQE measured in our cell might be only slightly influenced by undissociated FeB pairs. Indeed the J_{SC}, as observed before annealing and after regeneration, might also be somewhat lowered by the recombination-generation current J_{rg}. In p-i-n solar cells J_{rg} plays an important role in increasing the dark-current J_{dark} and specially by increasing the diode reverse saturation current I_0, which, on its turn influences V_{OC}.

In the ideal diode V_{OC} is given by:

$$V_{OC} = \frac{nkT}{q} \ln\left(\frac{I_{ph}}{I_0} + 1\right) \qquad \text{Equ. 3.3}$$

where I_0 is increased if I_{rg} becomes higher. Thus, the V_{OC} limitation to < 500mV might be caused by a weak recombination-generated current I_{rg} that still could be due to the presence of the inactive FeB complex (Fe_i^0). In the active state of the iron ion Fe_i^+ the V_{OC} is then strongly reduced by the strong recombination effect of the dissociated iron ions, i.e. by a high value of I_{rg}. This could explain a continuous limitation in V_{OC} (Equ. 3.3) to < 500 mV.

Why do we not observe any J_{SC} degradation for the “boron impurity free” interface even though iron is certainly also present on this side?

In the case of the joint presence of iron and boron, a pairing reaction is observed due to the Coulombic interaction between these two reactants creating an ionic bound complex FeB. ***In the FeB complex***, the interstitial iron Fe_i can be of a ***d-orbital electron configuration*** of either ***$3d^8$*** in its ***inactive state*** (Fig. 3.15 left) or ***$3d^7$*** in its ***active state*** (Fig. 3.15 middle). In the inactive state the total spin of the two unpaired electrons in the anti-bonding orbitals is S=1. In the active state, however three unpaired electrons – two of anti-binding and one of a bonding orbital- with a total spin of S= 3/2 are present. The electron affinity for an unpaired electron of a bonding orbital – to complete the orbital with an electron of the opposite spin- is much stronger than it is for an unpaired electron of an anti-bonding orbital. Therefore, the occupation of a bonding orbital by an electron is energetically favoured to the anti-bonding orbital. That’s why the active, dissociated Fe_i^+ ion of the complex equilibrium reaction is a much stronger acceptor.

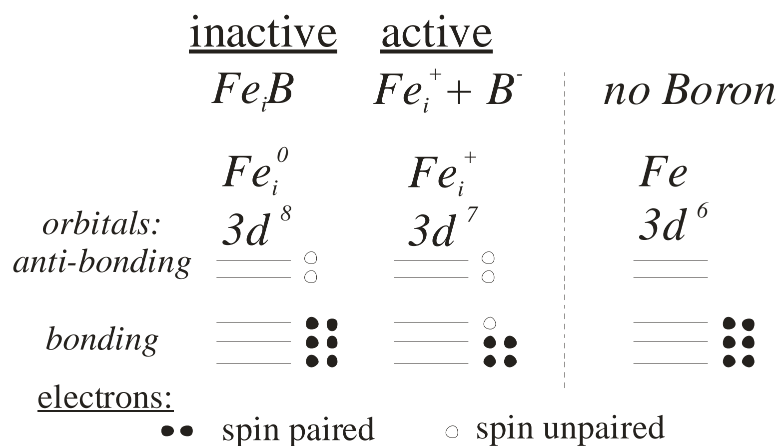

Fig. 3.15: Possible orbital states Fe_i^0 (left) and Fe_i^+ (middle) of iron for the FeB equilibrium reaction and neutral iron Fe (right).

In its ***neutral state*** – when no boron is present- the ***iron Fe*** has an electron configuration of

$3d^6$ (Fig. 3.15 right) and all electrons are spin paired in the d-orbitals (S= 0). The iron shows then no electron affinity. That is why a contamination by iron – as it must be presumed for the μc-Si:H solar cell after the "SF_6 & a-Si:H covering layer" treatment- does not quench the photon collection in the EQE, if no supplementary contaminant such as boron is present.

"How does this hypothesis correspond to the observed experimental characteristics of the μc-Si:H solar cells and of the SIMS-Analysis?"

The hypothesis of the quenching effect by the active Fe_i^+ seems to be indirectly confirmed by the "SF_6 & a-Si:H covering layer" treatment and by the CO_2 plasma series (Fig. 3.5 a-c). The boron-profiles by ***SIMS-Analysis*** revealed ***no cross-contamination into the intrinsic layer for the "SF_6 & a-Si:H covering layer" chamber treatment*** and ***less boron contamination*** in the intrinsic layer ***for a increasing CO_2 exposition time*** (Fig. 3.11). Nevertheless, boron contamination could only be avoided completely, by the "SF_6 & a-Si:H covering layer". treatment. The μc-Si:H solar cells of the "SF_6 & a-Si:H covering layer" treatment revealed no degradation in J_{SC} by annealing (ΔJ_{SC}= 0 mA/cm^2) and a V_{OC} of > 500 mV. For increasing CO_2 plasma exposition time the μc-Si:H solar cells revealed a decreasing ΔJ_{SC} of "J_{SC}-degradation ↔ J_{SC}-regeneration" phenomenon. However, the degradation ΔJ_{SC} could not be completely removed by the CO_2 plasma treatment, even for treatments up to 30 minutes. The V_{OC}–value remained < 500 mV but increased from 200 mV, for the case of no chamber treatment, to 400 – 450 mV for the various CO_2 treatments.

Simultaneously, a decrease of the quenching effect (J_{SC}-degradation) is observed (in the EQE curve) for increasing CO_2 plasma exposition times. We can assume that a lower boron contamination at the p-i interface reduces the number of FeB complexes which can act as deep gap recombination centres. The current loss ΔJ_{SC} which is caused by recombination-regeneration J_{rg} is reduced for increasing CO_2 plasma chamber passivation times.

Hereby, a change in boron contamination changes the quantity of the disturbing interstitial iron Fe_i^+ recombination centres with their strong recombination active donor level $Fe^{0/+}$. The higher or lower the boron concentration is, the higher or lower respectively the J_{SC}-degradation due to these recombination centres is to be expected. Thus, a V_{OC} of > 500 mV which depends on the I_0 (see 1.2.2.1) can only be achieved if no boron cross-contamination into the intrinsic μc-Si:H layer is present, as seen in the SIMS-profile on the right in Fig. 3.12 for the "SF_6/O_2 & a-Si:H covering layer" treatment and confirmed by the values obtained for corresponding μc-Si:H solar cells as given in tables 3.13.

The link between the hypothesis of the FeB complex and the degradation behaviour observed for our μc-Si:H cells is only based on the SIMS-Analysis with its observed boron concentration gradient at the p-i interface.

Due to the observed drastic changes in photon collection after annealing at 180 °C, temperature indeed seems to play a key role in this reaction. However, we do not have any data on the influence of substrate temperature on the thermodynamics of this reaction.

In order to prove directly the presence of a reversible FeB complex reaction in the μc-Si:H solar cells and determine the dominant direction of the reaction at room temperature, we would need to measure the dissociation as well as the re-association (recovering) reaction (Equ. 3.1). The activation energy of the dissociation reaction (E_b in Equ. 3.2) then would have to be determined by a temperature series, where the change of EQE would be continuously observed as function of the temperature during the annealing process.

Temperature [°C]	1/T [1/K]	J_{SC} [mA/cm2]
50	0.020	19.5
56	0.018	19.4
63	0.016	19.4
71	0.014	19.6
83	0.012	19.7
100	0.010	19.7
125	0.008	19.3
167	0.006	16.8
180	0.002	17.2
200	0.002	15.7

Tab. 3.15: Short circuit current J_{SC} of the annealing temperature series measured directly after the annealing by External quantum efficiency measurement.

A first series of varied annealing temperatures (30 minutes exposition) should show the initiation temperature of the J_{SC}-degradation reaction. This was studied for the μc-Si:H solar cell with a CO_2 passivation plasma of 3 minutes. For higher annealing temperatures than 125 °C J_{SC}-degradation is triggered, as shown by the drop of logarithm naturalis of J_{SC} and J_{SC} itself in Fig. 3.16 and Tab. 3.15, respectively.

From that temperature, J_{SC} starts decreasing by the annealing process –for increasing temperature-, from about 19.5 mA/cm^2 down to about 16 mA/cm^2 for 200 °C. The activation energy then could be determined by Equ. 3.2 from the gradient in Fig. 3.16. However, in our case this was not done due to the inconsistent decrease of J_{SC}. The problem by this measurements is, that once the J_{SC} of the μc-Si:H solar cell was degraded very quick by annealing. The recovering of J_{SC}, however, took up to one week, before a next annealing could be run. Therefore, a continuous observation of EQE during increasing annealing temperature would be needed, to be able to determine the exact activation energy of the

FeB-complex dissociation reaction. The back reaction of Fe_i^+ and B^- re-association to form the inactive Fe_iB complex after annealing (1h 30 min. @ 180°C) would then have to be determined by a continuous observation by EQE-measurement at a series of stabilized temperatures (range: 180°C ≤ $T_{solar\ cell}$ ≥ 50°C) during the storage time of, say, one week.

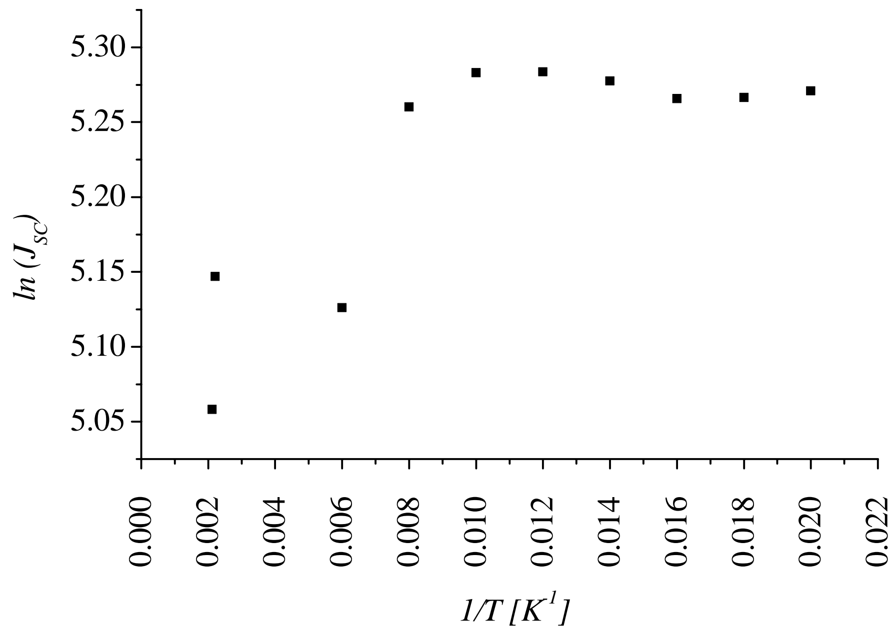

Fig. 3.16: Logarithm naturalis plot of J_{SC} against 1/ annealing temperature.

In order to obtain an idea of a suspected link between light-induced degradation effects and the FeB dissociation reaction the solar cells should also be continuously observed by EQE- and J(V)-measurement during 1000 hours 1 sun degradation by illumination for a stable substrate temperature of 50 °C.

Unfortunately, we do not have the needed equipment to carry out EQE- and J(V)-measurements directly on heated substrates.

Conclusions:

The "***J_{SC}-degradation ↔ J_{SC}-regeneration" phenomenon*** seen in the EQE spectra of our cells can be explained by the ***reversible dissociation reaction of an inactive FeB complex to the active interstitial iron ion Fe_i^+ and a boron ion.*** Hereby, we observe a ***change in recombination characteristics from a possible weak recombination induced by the "inactive" iron in the FeB complex to a very strong recombination effect the dissociated active Fe_i^+.*** This can be linked to the change in photon collection in the blue wave length

range of the EQE spectra: full collection for the inactive FeB complex and drastic losses for the active Fe_i^+ ion.

Nevertheless, the V_{OC}-values remained limited to < 500 mV for the CO_2 chamber treatment even after regeneration; we believe this is because V_{OC} is reduced by the remaining, weak recombination activity of the FeB complex orbitals.

There is a second problem linked to the microstructure with respect to the LPCVD ZnO [99].

3.2.2. A novel p-i-n structuring method

Thanks to the introduction of a novel ***ZnO lift-off structuring*** for p-i-n solar cells, the ***uniformity of the solar cell characteristics*** was ***drastically improved*** compared to the previous "state of the art" structuring by Plastic 70 (P70).

Experimental:

Half of a μc-Si:H solar cell sample was structured with the previous IMT "state-of-the-art" method (P70) after the deposition of the LPCVD ZnO back contact. In the previous method, the entirely deposited solar cell was structured by painting with the P70 paint by a pencil circular cells on the top of the sandwich structure deposited films (glass/TCO/Si:H/TCO). Afterwards, the cells are structured in a two-step process; first the ZnO layer is lifted off by a HNO_3 dip and second the Si:H layers are etched off by a SF_6/O_2 plasma in the IPL (Integrated Plasma Limited) 200 E etching system. A major disadvantage is the variation in cell surface due to the painting by hand.

The other half of the cell was structured with the novel structuring method, which is based on a lift-off technique: The solar cell is marked by a marker with a "masking" tool before the deposition of the LPCVD ZnO back layer (see Appendix A). The novel structuring tool enables the reproduction of solar cells of the same surface size, which is of major advantage.

The μc-Si:H solar cells were measured for their J(V)- and EQE-characteristics, initially, after annealing and after the "regeneration", i.e. one month later (Tab. 3.15 and 3.18 show only the immediate values after annealing).

In order to ***compare statistically*** and visually the two structuring techniques, the ***box plot*** (Fig. 3.16) will be used:

Each box encloses 25% of the data above and below the median displayed as a line. The lines

extending from the top and bottom of each box mark the minimum and maximum values within the data set that fall within an acceptable range. Any value outside of this range, called an outlier, is displayed as an individual point.

- Median - The middle value, such that half of the values are lower than the median and half the values are higher.
- Upper Quartile (UQ) - The data-values, such that 25 % of the total data-points of them are higher than the median.
- Lower Quartile (LQ) - The data-values, such that 25 % of the total data-points of them are lower than the median.
- Interquartile Distance (IQD) - The distance between the Upper and Lower Quartiles (UQ - LQ), enclosing 50 % of the total data-values.
- Outliers - Points whose value is either: greater than UQ + 1.5 × IQD or less than LQ - 1.5 × IQD. (The outliers have been used in the calculation of the box plot).

The IQD will therefore be used as a measure of the spread of the data.

Finally, to be consistent with the statistics of the previous μc-Si:H solar cells we also summarized the characteristic values with standard deviations (σ_{std}) of V_{OC}, FF and η as well in the tables 3.16 and 3.17: as average of all 16 solar cells of the substrate (except the excluded defective cells) in the first row and as average of the five best solar cells with its σ_{std} in the second row. Furthermore, the best μc-Si:H solar cell is added in the 3rd row of the table.

Results and discussion:

The box plot of FF and V_{OC} immediately demonstrates how much better is the novel lift-off technique. The median as well as the data spread were drastically improved.

The statistical analysis by box plot (Fig. 3.17) reveals for the novel lift-off method an essential improvement of the uniformity of the cell characteristics over the whole substrate for V_{OC} as well as for FF. Not only the median of V_{OC} as well as for that of FF drastically increased but the IDQ of the data is spread on a ~4 times smaller range for the novel lift-off structuring method.

In the case of the V_{OC} the median increased from 467 mV to 514 mV while the spread interquartile distance decreased from 45 mV to 6 mV. The same is to be observed for the FF which improved its median from 0.54 to 0.66 for a decreasing IDQ from 0.23 down to 0.03.

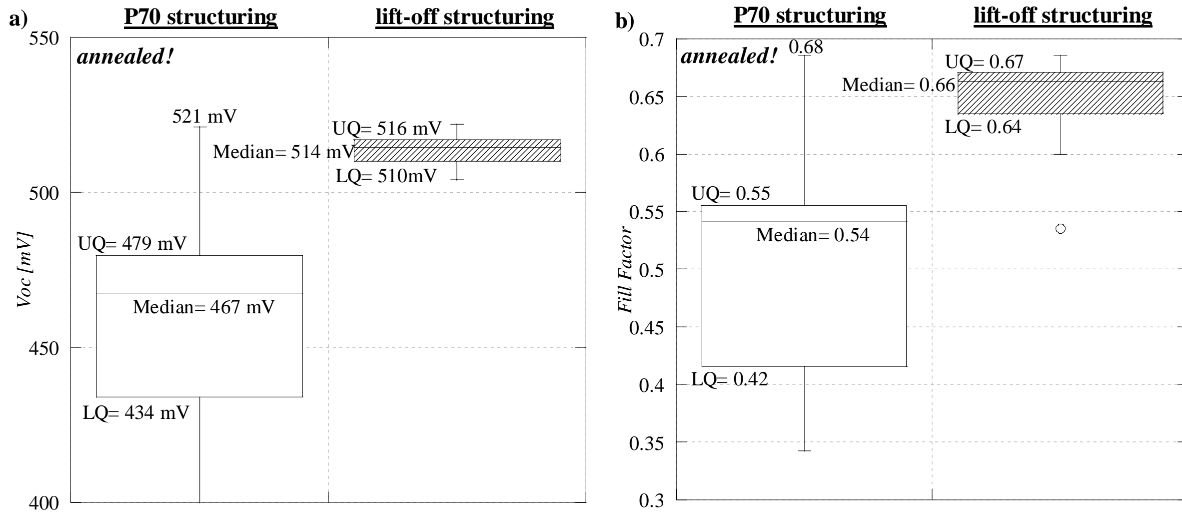

Fig. 3.16: Statistical analysis of V_{OC} and FF by Box Plot for the two structuring methods P70 and lift-off.

Using average values and their standard deviation $\sigma_{std.}$ for V_{OC} and FF revealed a similar difference between the two structuring methods.

The standard deviation σ_{std} given in the row "Average all" is very high for P70 structuring compared to the novel lift-off method. It is decreased by the lift-off structuring by a factor ~ 6 in the case of V_{OC} and by a factor ~ 3 in the case of FF.

P70 "state of the art"	V_{OC} [mV]	σ_{std}	FF	σ_{std}	J_{sc} [mA/cm^2]	η [%]	σ_{std}
Average all (excl. 1 cell)	464	**34**	0.512	**0.117**	17.26	4.1	**1.1**
Average of best 5	485	**42**	0.628	**0.067**	17.26	5.3	**0.7**
best cell	521		0.680		17.26	6.1	

Tab. 3.16: Sample structured by the "old" P70 "state of the art" method.

Novel lift-off	V_{OC} [mV]	σ_{std}	FF	σ_{std}	J_{sc} [mA/cm^2]	η [%]	σ_{std}
Average all (excl. 3 cells)	514	**5**	0.646	**0.041**	18.49	6.1	**0.4**
Average of best 5	516	**4**	0.675	**0.008**	18.49	6.4	**0.1**
best cell	516		0.685		18.49	6.5	

Tab. 3.17: Sample structured by the novel lift-off structuring method.

The ZnO lift-off structuring drastically improves the uniformity of the parameter V_{OC} and FF

on a μc-Si:H solar cell substrate with its structured cells compared to the old P70 structuring method, as shown both by the box plot in Fig. 3.17 as well as by the $\sigma_{std.}$-values in Tab. 3.16 and 3.17. It also improves the average values obtained for V_{OC}, FF and J_{SC} (already mentioned above).

3.2.3. Conclusions on single-chamber μc-Si:H solar cells

Summarizing the all the treatments of this μc-Si:H solar cell series, there is a single treatment that works out the boron issue: ***"SF$_6$ & a-Si:H covering layer". This treatment*** comes up to our expectations of $V_{OC} > 500$ mV and, at the same time, it ***avoids the reversible "J$_{SC}$-degradation ↔ J$_{SC}$-regeneration" phenomenon***;

In a first approach of the work we applied the different chamber treatment of this series on μc-Si:H solar cells.

By this means best μc-Si:H solar cell characteristics lead ***to a V$_{OC}$= 516 mV and to a FF= 0.675***. Furthermore, the ***"SF$_6$ & a-Si:H covering layer"treatment completely avoids*** the phenomenon of ***"J$_{SC}$-degradation ↔ J$_{SC}$-regeneration"*** by annealing.

No other treatment was as efficient for the V_{OC} issue, the CO_2 plasma helped to decrease the loss of photon collection by annealing. A ***CO$_2$ plasma of ≥ 15 minutes duration helps to limit the loss ΔJ$_{SC}$ by annealing to ~ 1- 2 mA/cm^2*** (Tab.3.11). For the a-Si:H covering layer as well as for the simple "SF_6/O_2 cleaning" the photo collection was initially just as good, but it was very poor in the annealed state (J_{SC}< 14 mA/cm^2). The best V_{OC} values attained thereby varied in the range of 450 – 490 mV but did not exceed 500 mV.

FTPS measurements on the μc-Si:H solar cells confirmed the tendency: the ***lowest defect density*** was obtained ***for the "SF$_6$/O$_2$ cleaning & a-Si:H covering layer" treatment*** (Fig. 3.8 right).

Nevertheless, the CO_2 plasma treatment gave rise to improvements especially for the "J_{SC}-degradation ↔ J_{SC}-regeneration" issue. However, none of the CO_2 treatments could completely avoid the J_{SC}-degradation. Furthermore, the V_{OC} limitation to < 500 mV remained. The defect densities as evaluated by residual absorption α(0.8eV) varied by a factor ~4 between the best and the worst of the CO_2 treatments (Fig. 3.8 right).

The ***correlation between defect density and V$_{OC}$ reveals*** the tendency to obtain ***higher V$_{OC}$ for lower defect density***. In this series the highest V_{OC} and the lowest defect density was achieved for the "SF_6/O_2 cleaning & a-Si:H covering layer" treatment while the lowest V_{OC} with the highest defect density was achieved for the simple "a-Si:H covering layer".

In a second approach we then examined the ***influence of boron contamination at the p-i interface by SIMS-Analysis***. Hereby, we corroborated our suspicion that boron contamination at the interface – most probably caused by cross-contamination from chamber walls – ranging into the intrinsic Si:H layer plays a key role for the issues mentioned above. The ***"SF_6/O_2 cleaning & a-Si:H covering layer"*** treatment revealed itself to be the best treatment of this study to avoid boron cross-contamination into the intrinsic layer. With this treatment, the ***steepest step-like decay in boron concentration of 10^3 cm^{-3} within only 50 nm from the p-i interface*** was achieved.

It is very important to obtain in the SIMS boron profiles a steep linear step-like decrease of the boron concentration over 3 orders of magnitudes within less than 100 nm. The "SF_6/O_2 & a-Si:H covering layer" treatment is the only treatment to provide such a steep decrease in boron concentration and is therefore the only treatment of the series to avoid boron cross-contamination.

Connecting the first approach of looking at ***solar cell characteristics with*** the second approach of looking at the ***boron contamination at the p-i interface reveals*** a dependence between ***low defect density for high solar cell performance and low boron contamination***. Hereby, the best values are achieved for the "SF_6/O_2 & a-Si:H covering layer" treatment.

The fact that all treatments except the "SF_6/O_2 cleaning & a-Si:H covering layer" reveal a shallow exponential decrease in boron concentration lead us to the ***suspicion that boron plays a key role for the "J_{SC}-degradation ↔ J_{SC}-regeneration" and V_{OC}-limiting issue***.

The strong increase in defect density in the μc-Si:H solar cells in the case of the least effective chamber treatments may be explained by a strongly increased boron contamination at the p-i interface. Thus, the boron could directly or indirectly be responsible for a decrease in photon collection after annealing.

The ***"J_{SC}-degradation ↔ J_{SC}-regeneration" phenomenon*** that reveals itself in the in EQE spectra can be explained by the ***reversible dissociation reaction of the inactive FeB complex to the active interstitial iron Fe_i^+ and the boron contaminant***. Hereby, one probably observes a ***change in recombination*** characteristics from the ***weak recombination role of the "inactive" iron in the FeB complex to the very strong recombination role of the dissociated active ion Fe_i^+***. This can be linked to the change in photon collection in the blue wave length range of the EQE spectra: full collection for the inactive iron in the FeB complex and drastic losses for the active iron.

Nevertheless, the V_{OC} remained limited to < 500 mV due to the J_{SC} which we think is reduced by the J_{dark} respectively J_{rg} of the weaker recombination activity of the FeB complex orbitals.

The introduction of a ***novel p-i-n structuring*** method ***by ZnO lift-off*** (see Appendix A)

drastically ***increased the uniformity*** (as contributed by the standard deviation σ_{std}) of the solar cell characteristics (V_{OC} and FF) compared to the previous IMT "state-of-the-art" (P70) method.

3.3. μc-Si:H solar cells incorporating i-layers deposited close to the high-pressure regime

The development of "IMT state-of-the-art" microcrystalline solar cells of laboratory size in VHF-GD reactors has so far generally been made in a pressure regime below 1 mbar for deposition rates of 1- 5 Å/s.

In the previous chapter 2.2 the deposition series of intrinsic layers, extending to higher pressures showed that "device-grade intrinsic" ***μc-Si:H layers*** can, in principle, be ***deposited at rates up to about 25 Å/s***. In order to reach such a high deposition rate, ***increased deposition pressures (up to 8 mbar)*** were used.

In the present study, this kind of intrinsic μc-Si:H layers have been incorporated into p-i-n solar cell devices. At the same time a microcrystalline trimethylboron doped p-layer was incorporated into these solar cells, whereas our earlier μc p-doped layers were based on use of B_2H_6 doping gas. This was a further difficulty for our work. Furthermore, the need of an effective chamber treatment after the deposition of the p-doped layer to avoid cross-contamination, of the subsequent i-layer and so as to achieve satisfactory μc-Si:H solar cell performance (see chapter 3.2) was discovered only recently. Thus all the high-rate deposited cells presented here, had been fabricated before the introduction of the chamber treatments. We must therefore assume that they have strong cross-contamination (boron contamination) in the beginning of the i-layer.

Furthermore, the deposition of a highly microcrystalline p-doped layer –using trimethylboron - could not yet be achieved during of the present high-pressure study due to hardware limitations. Therefore, the microcrystalline p-doped layer had to be made in other deposition systems or by an alternative process (see 2.1). Hereby, the p-doped layer (that is sensitive to post-oxidation) was exposed to air during its transfer from one chamber to the other. All these "historical" factors explain (at least partly) the relatively poor results obtained in this part of our work.

3.3.1. Pressure series ranging from 0.5 to 3 mbar with rates up to 14.5Å/s

Based on the series on the high-rate deposited intrinsic μc-Si:H layers (chapter 2.2) a first p-i-n solar cell with a high-rate (14.5 Å/s) intrinsic μc-Si:H layer was deposited at 3 mbar. Because of its relatively bad electrical performance, we carried out a full investigation on the influence of the working pressure, with a series of such cells deposited at pressures between 0.5 and 3.0 mbar.

Experimental:

The p-i-n solar cells were entirely deposited in the single-chamber system with the cylindrical plasma containment box at an inter-electrode gap d_{gap} of 16.5 mm. Unfortunately, the TMB p-doped layer could not be optimized at that moment because of hardware limitations. The p-doped layers were deposited at 1.0 mbar under a flux of 150 sccm H_2 and 1.5 sccm SiH_4 with 0.5 sccm TMB (2 % diluted in H_2) under an applied VHF-power of 6 W at 70.0 MHz.

The series consisted of intrinsic layers deposited at 0.5, 1.0, 2.0 and 3.0 mbar. The SiH_4 concentration was kept constant at 2.9 % with a gas flow rate of 100 sccm H_2 and 3.0 sccm SiH_4. The VHF plasma excitation power at 70.0 MHz, however, was optimised in the range of 20 to 120 W. Finally, the n-doped layers were deposited with parameters given for the amorphous layer in Tab. 3.7 for 70.0 MHz.

Solar cells characteristics were determined by J(V)-curve measurements under a solar simulator (WACOM WXS-140S) at AM 1.5 and by external quantum efficiency (EQE) measurement (all EQE curves shown here were measured with an applied bias voltage of -0.5 V, necessary because of the weak solar cell performance) to verify the presence of a "microcrystalline –type response" in the red and near-infrared spectral range.

Further information about the material characteristics (E_{Urbach} and residual absorption α(at 0.8 eV)) of the intrinsic layer within the solar cells were obtained by FTPS measurements [49].

<u>*Results and discussion:*</u>

Microcrystalline Si:H solar cells deposited under standard (low-pressure) conditions (< 1 mbar) in the same "crystallinity range" (i.e. near the μc-Si/ a-Si transition point) show a typical microcrystalline-type external quantum efficiency (EQE) in the red and near-infrared part of the spectrum. Typically, a good μc-Si:H solar cell incorporating a low pressure deposited i-layer has a EQE $\geq$ 0.3 at λ= 800 nm. In Fig. 3.17, one can note that the cell incorporating the intrinsic layer deposited under high-pressure (3.0 mbar) conditions has almost no more EQE in the red and near-infrared. The EQE curve measured for the i-layer deposited at 3 mbar is amorphous-like.

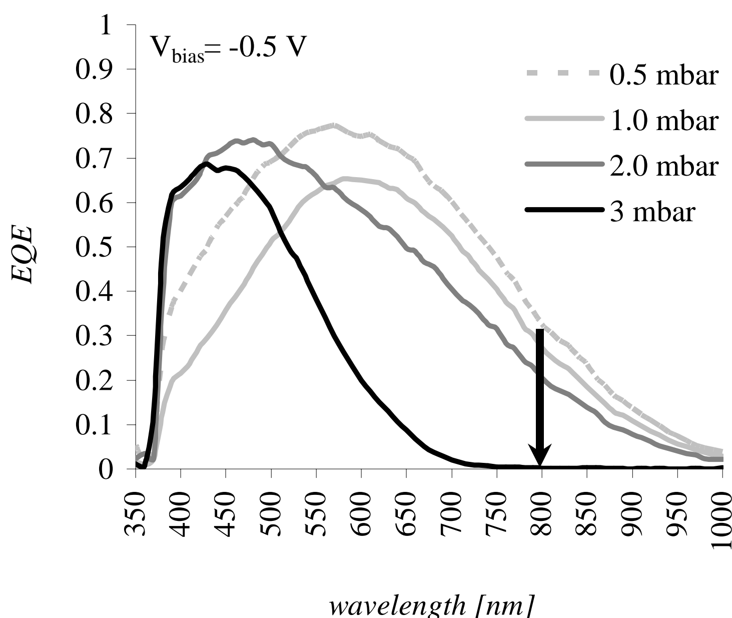

Fig. 3.17: External quantum efficiency curves of μc-Si:H solar cells deposited at varying pressures between 0.5 and 3.0 mbar. Note the decreasing EQE of the red and near-infrared for increasing pressure (up to 3 mbar).

Recently M. Tanda and A. Matsuda reported about similar deficiencies in the external quantum efficiency when using the Triode Reactor Configuration [100] also for a combination of VHF-PECVD and HPD.

Fig. 3.17 shows the external quantum efficiency curves for cells deposited at 0.5, 1.0, 2.0 and 3.0 mbar. Even though the external quantum efficiency decreases in the red and near-infrared range, when going from 0.5 to 3 mbar, the Raman crystallinity factor ϕ_c emphasizes microcrystalline material measured on the top of the solar cell surface (from n-layer side). Raman crystallinity factor , however, only represents the last 120-170 nm of the total thickness of the solar cells. Therefore, the crystallinity at the p-i interface is not known, e.g. one could have an amorphous initial nucleation layer.

Focussing on the microcrystalline p-i-n solar cell deposited at high-pressure (3.0 mbar) with a rate of 14.5 Å/s, Raman spectroscopy shows a Raman crystallinity factor ϕ_c of 0.62 at the top of the solar cell surface –which can also be found for “state-of-the-art” μc-Si:H solar cells deposited at low pressure. However, the Raman crystallinity factor ϕ_c of only 0.13 measured from the glass p-side shows a mostly amorphous characteristic. An amorphous incubation zone of a thickness of at least 50 nm is, thus, presumably limiting the EQE above 800 nm. These experimental observations may give a hint about the origin of the amorphous-like character of the EQE-curve, e.g. no or decreased response in the red and near-infrared range. In contrary, for the pressures 2.0, 1.0 and 0.5 mbar, Raman crystallinity factor ϕ_c show values between 0.85 and 0.80 on the surface and 0.67 on the glass side (for the three pressures) of the layer. The gradient of Raman crystallinity factor is much lower within these microcrystalline Si:H layers which were deposited at decreasing pressures of 2.0, 1.0 and 0.5 mbar, as compared for the layers deposited at 3 mbar. The fact that an application of a bias voltage (-0.5 V) for the external quantum efficiency measurements was needed gives a hint that high defect densities are present in these high-pressure deposited intrinsic layers leading to crucial collection problems. Furthermore, very low V_{OC} values of 200 to 300 mV (not shown) also point to problems within the device (unsatisfactory p-i interface, poor i-layer quality).

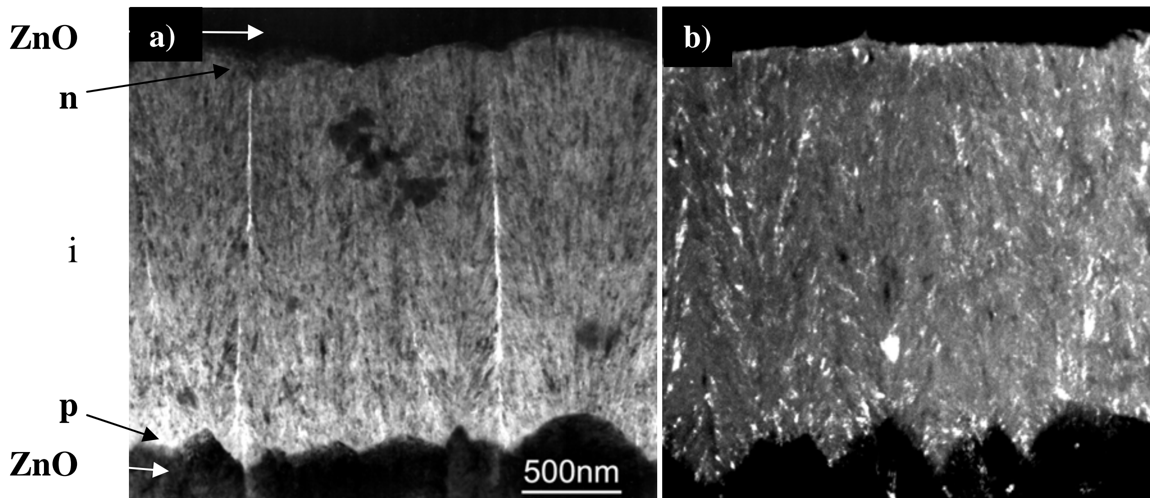

Fig. 3.18: Micrographs cross-sections of a) a high-rate deposited μc-Si:H solar cell (rate of intrinsic layer = 14.5 Å/ sec) and b) a low rate deposited μc-Si:H solar cell (rate of intrinsic layer ≈ 3 Å/ sec) taken by a Transmission Electron Microscopy (TEM).

After having observed the loss in external quantum efficiency at $\lambda > 800$ nm, the microstructure of the solar cell with an intrinsic μc-Si:H layer deposited at 3 mbar at a deposition-rate of 14.5 Å/s was studied by TEM (Fig.3.18 a) to investigate further its micro-structural properties. As reference a TEM micrograph of a fully μc-Si:H solar cell fabricated at IMT in the “standard” pressure and deposition rate regime is shown in Fig. 3.18 b.

Compared to layers deposited at lower pressures and low rates (considered as "standard" condition), on the same substrates the present solar cell (deposited at 14.5 Å/sec in Fig. 3.18) shows a remarkably high crystallinity. The crystallinity is surprisingly complete and uniform from the bottom to the top of the device, i.e. on the micrometer scale. On the other hand, relatively long cracks appear within the device which consists, of looser material or voids. This direct comparison shows that the material deposited at lower pressure is denser. Nevertheless, no other significant differences in crystallinity can be observed on these high-rate μc-Si:H films compared to previous studies on growth of μc-Si:H films and cells under "standard" condition (as shows Fig. 3.18 b). However, we have to keep in mind that the examinations by Raman spectroscopy and TEM-Micrograph (Fig. 3. 18 a) as mentioned previously are of two different depth scales 50 nm for Raman at an excitation wavelength of 514 nm and 1 μm for TEM, respectively.

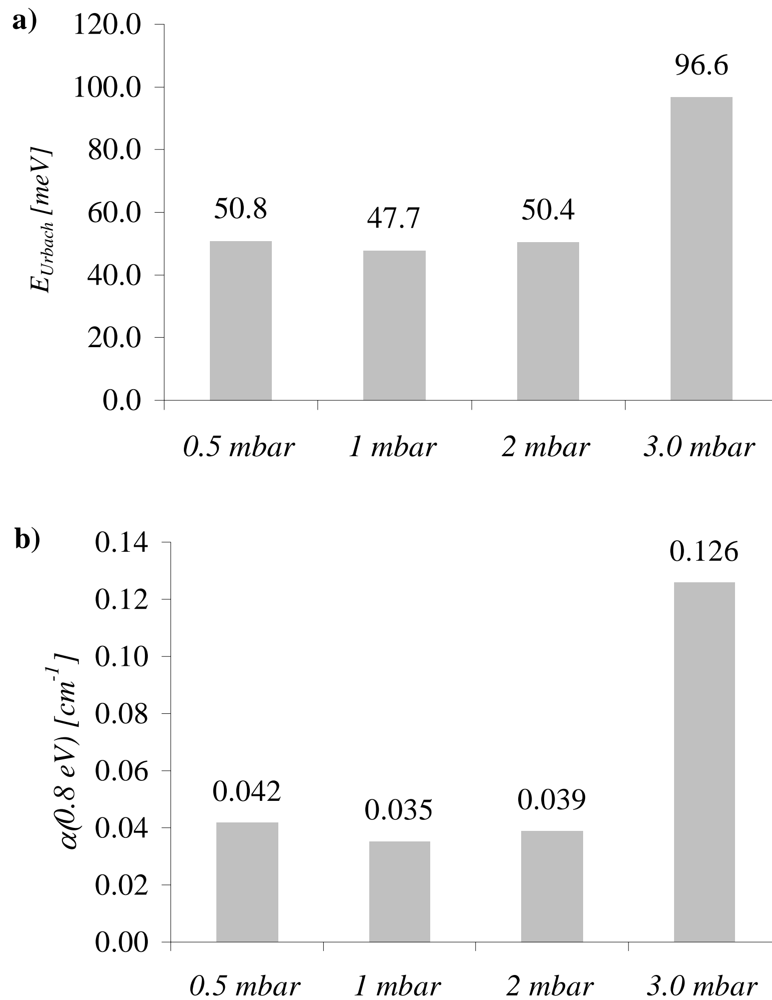

Fig.3.19: Defect characterisation by FTPS: a) E_{Urbach} and b) residual absorption $\alpha(0.8\ eV)$ for μc-Si:H solar cells of the pressure series.

The high crystallinity is thought to be caused by the fact that the incorporated intrinsic layer

was not very well optimised with respect to the amorphous/ microcrystalline transition occurring at varying silane concentration. The presence of these long cracks may on one hand increase the sensitivity to post-oxidation of the μc-Si:H layer – this is known to decrease the external quantum efficiency in the red and near-infrared range. On the other hand the μc-Si:H layer may risk to be short-circuited via the loose material in the cracks. All three observations (post-oxidised material, low ϕ_c at the p-i interface and high defect density) can explain the decrease of collection in the red and near-infrared range. In reality, we have to suppose that post-oxidation, short-circuiting, a high defect density of the intrinsic μc-Si:H layer, cross-contamination by boron (see chapter 3.2), as well as some further non-detected issues interact and are the origin of the poor μc-Si:H solar cell performance.

FTPS-Analysis on the solar cells of the pressure series show marked differences in i-layer material quality, as evidenced by E_{Urbach} and by the residual absorption $\alpha(0.8\ eV)$ in Fig. 3.19.

E_{Urbach} is an indicator of the band tail states that increase as the short range disorder increases. The residual absorption $\alpha(0.8\ eV)$ is related to the sub band-gap defects, e.g. in μc-Si:H material an increased absorption at 0.8 eV refers to an increased recombination centre density.

Good μc-Si:H solar cells are reported to have E_{Urbach}-values of 35- 38 meV [50] and a low residual absorption α at 0.8 eV in the range of 10^{-2} cm^{-1}. In the case of our pressure series, E_{Urbach} shows, for all solar cells, rather high values. This is an indicative of an important density of band tail states, e.g. an increasing atomic-scale disorder. The sub band-gap defect density, as evaluated from the $\alpha(0.8\ eV)$-values of the order of 10^{-2} cm^{-1}, however, is similar to device grade material.

These material quality parameters are drastically higher in the i-layer deposited at 3 mbar.

The high defect density contributes on one hand to the poor solar cell characteristics as mentioned above. However, this is not the only problematic issue for the solar cell performance, as we have already seen (chapter 3.2). The strong impact of the boron cross-contamination at the p-i interface has also a detrimental effect on the μc-Si:H solar cell characteristics.

So far, we have seen that even though the i-layer deposited on glass had device-grade quality as monitored by optical measurements, their incorporation into p-i-n devices lead to unsatisfactory results. As far as the present process parameters and system configuration is concerned, the use of rather high plasma excitation power (>1 W/cm^2) as well as the very high pumping speed (4.2 m^3/min. for a chamber volume of 0.016 m^3) are suspected to have a

crucial detrimental impact on the defect density. Too high plasma excitation power is reported to drastically increase defect density, while too high pumping speed could lead to a too low partial pressure of hydrogen, resulting in low atomic hydrogen density – leading to a defective μc-Si:H growth.

<u>*Conclusions:*</u>

The solar cell pressure series for the deposited intrinsic μc-Si:H layers shows a drastic decrease of the external quantum efficiency in the red and near-infrared range for an increased deposition pressure. FTPS measurements show a tremendous increase of the band tail states and the defect density of the intrinsic layer deposited at a rate of 14.5 Å/s at 3 mbar. Furthermore, an amorphous incubation layer is observed by Raman measurement at the p-i interface for these solar cells. None of the incorporated intrinsic high-pressure, high-rate μc-Si:H layers lead to solar cells with acceptable performances.

3.3.2. Introduction of nucleation-layer for the high-pressure regime

A μc-Si:H nucleation layer, deposited under soft conditions (low plasma excitation power, and low pressure) right on top of the p-layer, was introduced to counteract the bad

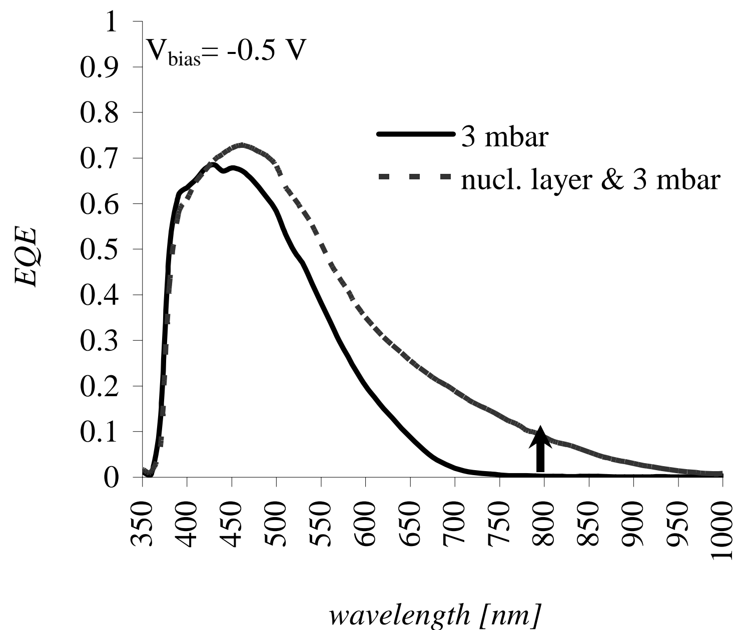

Fig. 3.20: External quantum efficiency curves of two solar cells with intrinsic layers deposited at 3 mbar (deposition rate ~14.5 Å/s) with and without a nucleation layer.

crystallisation [101] right from the beginning of the deposition process, so as to avoid an amorphous incubation layer at the p-i interface.

When measuring the external quantum efficiency curve of two solar cells deposited under identical conditions, except for the initial nucleation layer, a clear difference in the external quantum efficiency in the red to near-infrared range is seen (Fig. 3.20). In that way the Raman crystallinity factor ϕ_c on the glass side could be increased from 0.13 to 0.37.

Nevertheless, even though an improvement was achieved with this method, the resulting EQE is not satisfactory and, further optimisation would be necessary to achieve acceptable external quantum efficiency ($EQE_{@800nm} > 0.3$) in the red and near-infrared range. Furthermore, it is not known, if the observed gain in external quantum efficiency (Fig. 3.20) is due to an improved growth of the high-rate deposited intrinsic layer or results directly from an improved p-i interface.

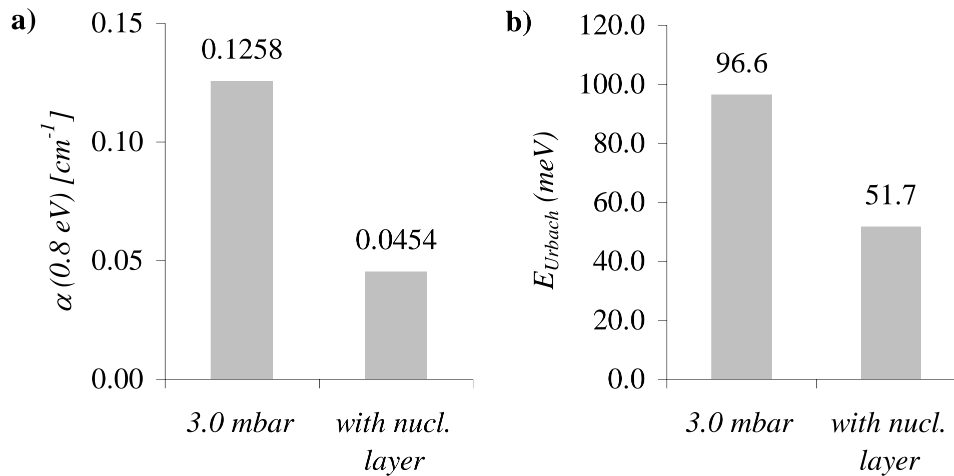

Fig. 3.21: Defect characterisation by FTPS: a) E_{Urbach} and b) residual absorption α(0.8 eV) for μc-Si:H solar cells with and without a nucleation layer.

The introduction of a highly microcrystalline nucleation layer, led to an improved value for E_{Urbach} and to a decrease of residual absorption α(0.8 eV), as shown in Fig. 3.2.1. The band tail states, as well as the deep sub band-gap defects density (as evidenced by α(0.8 eV)) were drastically decreased to the level of the other solar cells of the present pressure series. Still, the density of deep sub band-gap defects remained too high. Another potential solution to overcome the presence of an amorphous incubation layer is the application of a so-called

hydrogen profiling technique[6] during the growth of the intrinsic Si:H layer.

Conclusions:

The ***introduction of a highly μc-Si:H nucleation layer*** led to a ***slight improvement of the external quantum efficiency*** in the red and near-infrared range, as well as to an improvement of Raman crystallinity on the bottom side of the layer. The defect density decreased to more reasonable values, but the ***overall performances*** of the devices incorporating such intrinsic layers are ***still unsatisfactory*** ($EQE_{@800nm} < 0.3$).

[6] The term „hydrogen profiling" is used for a continuous, slight adaptation (decrease as well as increase) of hydrogen dilution (or inversely of silane concentration) during the deposition, thus, so as especially important during the initial growth phase, to avoid an amorphous incubation layer.

Chapter 4: Optimisation of homogeneity and plasma confinement box design

IMT has introduced a square plasma confinement box (Fig. 4.1) in 1998 in order to obtain a well defined space for the plasma. The electrodes of the plasma confinement box configuration – not to be mistaken for the Plasma Box^{TM} of Unaxis KAI reactors – consist of a gas showerhead and of the plasma confinement box. The process gases are fed over the gas showerhead and pumped over small gas outlet holes in the box walls into the vacuum chamber. The VHF–power is, as well, coupled into the plasma by the showerhead electrode.

In a conventional reactor, electrodes are just put inside a vacuum chamber (Fig. 4.1 a) from which process gas is pumped. The plasma burns between the electrodes. Hereby, the gas and its derivates (ions, radicals) can be expected to be found in the whole chamber volume – not only between the electrodes. There are no barriers which reduce or limit the free movement of these molecules, atoms and particles. Hereby, contamination can be adsorbed on the chamber walls.

The ***plasma confinement bo***x (Fig. 4.1 b) introduces a ***well defined space for the plasma***, whilst outside no plasma is present. The introduction of a plasma confinement box is not thought to avoid contamination, but to reduce or to limit contamination within the plasma confinement box. Even if the chamber walls – not the plasma confinement box walls- are contaminated, the presence of the plasma confinement box reduces, or possibly even avoids back diffusion of wall desorbed cross-contaminants into the plasma. However, the plasma confinement box has to be cleaned by an in-situ cleaning-process with an etching-gas, e.g. SF_6/O_2 or NF_3, to reduce contamination.

So far, no investigations have been made on the influence of the geometry of the square plasma confinement box of the IMT on the deposition behaviour.

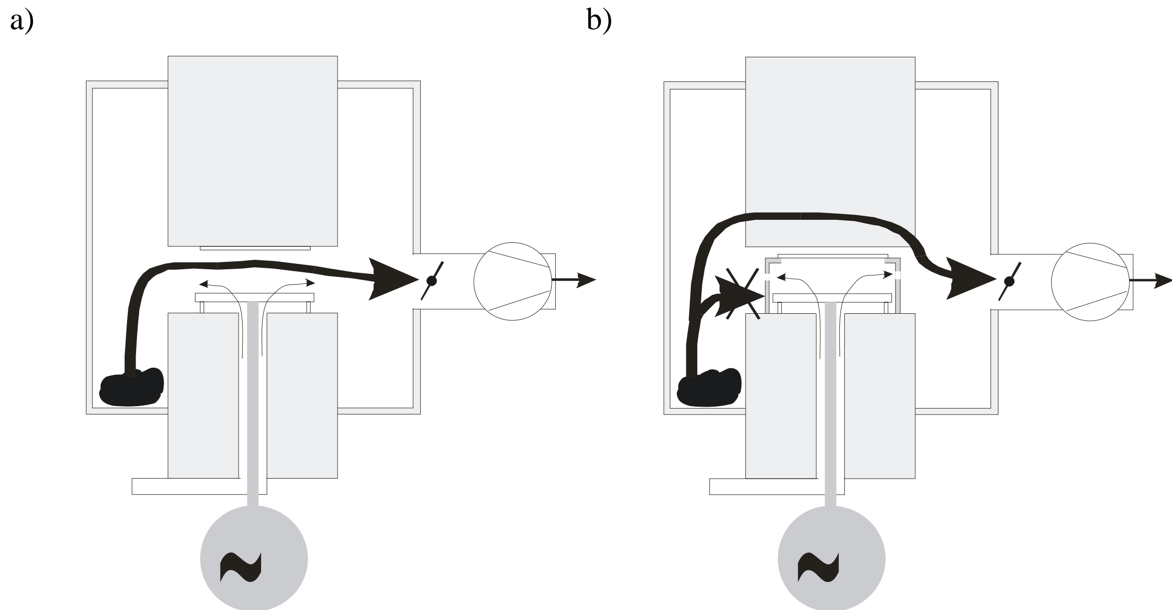

Fig. 4.1: Comparison of the design of (a) a conventional reactor with parallel plate electrodes, and (b) a reactor with a plasma confinement box: with respect to impurity flow. The arrows represent the impurity flows.

It is known that very high frequencies (VHF) introduce inhomogeneity for large electrode size [102]. Using VHF at 135.6 MHz in the low pressure regime, the square geometry together with IMT's small laboratory size electrodes (~10 × 10 cm^2) so far did not reveal any problems in homogeneity for the deposition of solar cells.

However, inhomogeneity appears when further increasing the pressure (> 0.5 mbar) for 135.6 MHz. With respect to the high-rate high-pressure (> 1 mbar) regime for µc-Si:H layers a strong inhomogeneity has to be avoided. Using a frequency of 70.0 MHz leads to a much better homogeneity at high-pressure (here 3 mbar). But in all cases ***the best homogeneity at an excitation frequency of 70.0 MHz is only obtained for the redeveloped round plasma confinement box***.

4.1. Improvement of homogeneity with respect to VHF-frequency and VHF-power at higher pressures

The subject of the present study focuses on the homogeneity of the deposited layers at VHF.

During the first part of this study, homogeneity was studied only by visual observation with respect to interference fringes. Thereby two plasma excitation frequencies were compared: 135.6 MHz and 70.0 MHz. Only in a second part crystallinity was determined by Raman

spectroscopy and represented by the Raman crystallinity factor ϕ_c. This was examined for the favoured frequency of 70.0 MHz – where reasonable homogeneity can be obtained at higher pressures.

Experimental:

In a first series the influence on deposition homogeneity of the increasing pressure from 0.3 – 1 mbar was studied for 135.6 MHz. This was then compared to a similar pressure series for 70.0 MHz.

The experimental conditions were chosen in the same order as for intrinsic "state-of-the-art" low pressure µc-Si:H layers (recipe 3.1 Tab. 3.6), while the VHF-power was only 10 W (this is a reasonable value given for the smaller electrode surface of the square design) and the pressure was varied. In addition, a higher total gas flux (factor 3 for H_2 and SiH_4 compared to low gas flux) was also examined.

Because of the observed inhomogeneity, the influence of the VHF-power at higher pressures (0.9 mbar) was then examined with a power series of 10 to 40 W for low gas flux at 135.6 MHz and at 70.0 MHz (Fig. 4.2).

The description of the homogeneity was, on one hand, carried out by visual observation of the interference fringes. The photos were taken by a CCD-camera and the images were processed with respect to their contrast and shading to enhance the visibility of the interference fringes. On the other hand, a thickness profile with its relative standard deviation (σ_{std}) was determined for six points (1 in an edge, 2 at border, 1 in centre, 2 at half distance from centre to border) by a step profiler.

Finally, the pressure was even further increased up to 3 mbar causing serious problems in homogeneity for the square shaped plasma confinement box. Here, the Si:H layers were examined with respect to their Raman crystallinity factor ϕ_c at different points on the substrate (Fig. 4.1 centre & spot in the edge).

All layers were deposited on AF45 Schott glass in order to obtain a better visibility of the interference fringes.

The initial system configuration was equipped with a "state-of-the-art" plasma confinement box of IMT small surface research reactors – square shape (Fig. 4.5 a) and an inter-electrode gap distance d_{gap} of 20 mm.

<u>*Results and discussion:*</u>

For 135.6 MHz the increase of pressure from 0.3 to 0.9 mbar introduces a strong increase in inhomogeneity (Tab. 4.1 left) as documented by the increasing number of interference fringes, i.e. σ_{std} increased from 5.5 % to 35 %. At 70.0 MHz we observe, however, an opposite trend: an improvement of the homogeneity for increasing pressure. The inhomogeneity decreased from a $\sigma_{std.}$ of 14 % to 5 % when increasing the chamber pressure from 0.3 mbar to 0.9 mbar.

Dep. cond.:	VHF **135.6 MHz**	VHF **70.0 MHz**	Dep. cond.:	VHF **135.6 MHz**	VHF **70.0 MHz**
Total gas flux:	*"low"*		Total gas flux:	*"high"*	
p= 0.15 mbar			p= 0.3 mbar		
p= 0.3 mbar			p= 0.6 mbar		
p= 0.9 mbar			p= 0.9 mbar		

Tab. 4.1: Pressure series for low and high total gas flow rates at the excitation frequencies of 135.6 MHz and 70.0 MHz.

Comparing the series of "low" and "high" total gas flow rates, no significant differences in thickness-inhomogeneity were observed visually for 70.0 MHz (Tab. 4.1). For 135.6 MHz, however, the inhomogeneity is slightly reduced for a higher total gas flux, i.e. there are only two instead of three interference fringes. We observed that, ***at higher pressures (around 1 mbar) the homogeneity with its $\sigma_{std.}$ of 5 % for 70.0 MHz is much better than it is for 135.6 MHz with a $\sigma_{std.}$ of 35 %***. Further observations (not given here) show this holds true also for the range of 1-1.5 mbar.

Because of the increased thickness-homogeneity at 70.0 MHz, this is the frequency value we chose for the further development of intrinsic μc-Si:H layers in the high-pressure regime.

A further observation is that ***depositing μc-Si:H layers on IMT standard LPCVD ZnO-coated*** (process: M4, 36 min.) glass substrates, ***shows a less pronounced thickness-inhomogeneity than on plain glass*** was observed.

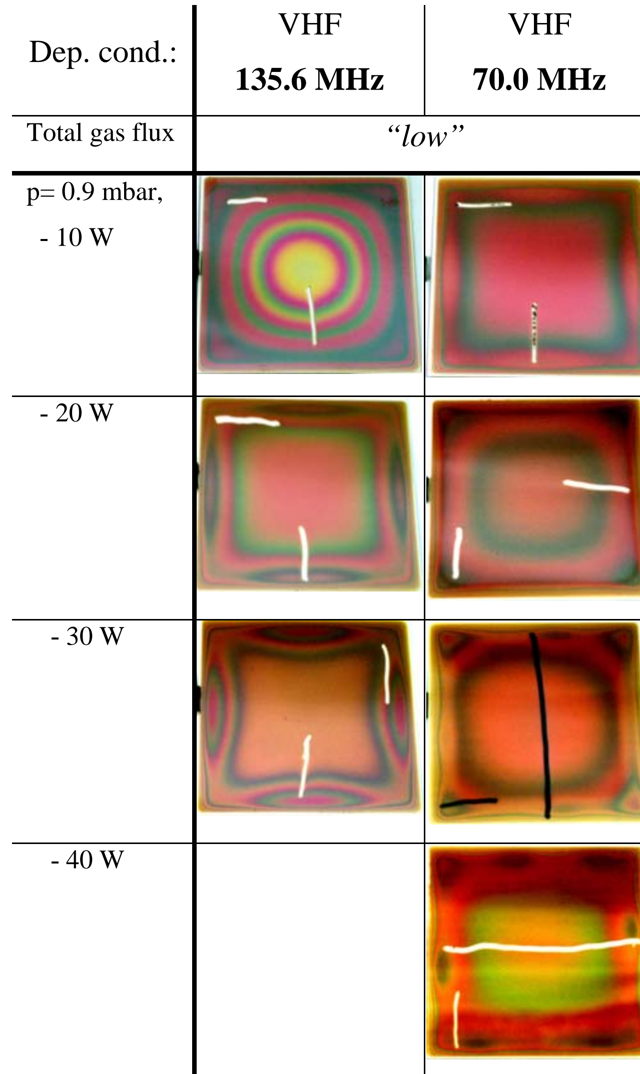

Dep. cond.:	VHF **135.6 MHz**	VHF **70.0 MHz**
Total gas flux	*"low"*	
p= 0.9 mbar, - 10 W		
- 20 W		
- 30 W		
- 40 W		

Tab. 4.2: Power series for low gas flow applying excitation frequencies of 70.0 MHz and 135.6 MHz.

Due to the fact that microcrystalline growth of Si:H layers is favoured at 135.6 MHz, as compared to 70.0 MHz, improvements in homogeneity at high-pressure remain of high importance for 135.6 MHz. Therefore, the influence of the VHF-power is studied with respect to an elevated pressure of 0.9 mbar. The deposited layers of the ***power series (Tab. 4.2) for the excitation frequency 135.6 MHz reveal an improvement*** of homogeneity: the standard deviation σ_{std} of the thickness values was reduced ***from 35 % down to about 13 %***, when ***increasing the VHF-power from 10 W to 30 W***. (Fig. 4.2). For an excitation frequency of 70.0 MHz, however, the $\sigma_{std.}$ of the thickness values increased from 5 % to ~11 % when increasing power in range of 10 to 40 W.

For higher working pressure the decrease of the excitation frequency to 70.0 MHz improves the thickness-homogeneity of deposited μc-Si:H layers to a $\sigma_{std.}$ of ~5 %.

The decrease of the excitation frequency from 135.6 MHz to 70.0 MHz for further studies is a compromise between homogeneity and higher deposition rates.

Based on the previous series, the ***further development of intrinsic μc-Si:H layers*** in the high-pressure regime (> 1 mbar) was done ***with the excitation frequency of 70.0 MHz***.

So far, the deposited μc-Si.H layers on plain glass showed a reasonable homogeneity, for a SiH_4 concentration which was not completely in the transition of the microcrystalline to amorphous Si:H. Further layer optimisation with respect to the transition, however, showed an increasing thickness-inhomogeneity as we increase the SiH_4 concentration (Fig. 4.2 a-c at 3 mbar). This inhomogeneity shows up as in the shape of enlargening spots at the edges of the substrate. Additionally to the inhomogeneity at the highest concentration a negative imprint of the showerhead holes appeared (Fig. 4.2 c). The imprints could be removed by increasing the number of gas outlet holes in the showerhead. However, the basic thickness-inhomogeneity remained.

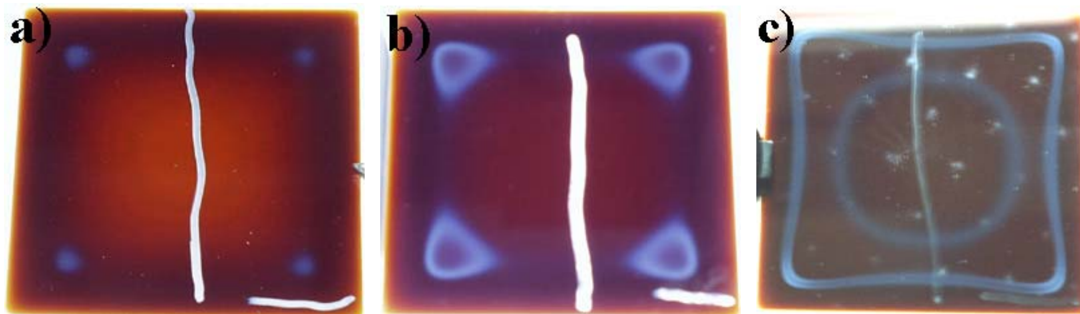

Fig. 4.2: Photographs of deposited μc-Si:H layers (70.0 MHz) approaching the transition within a dilution series (c(SiH_4)= a) 3.9%, b) 4.5 %, and c) 5.1 %) at high-pressure (3 mbar).

Investigations by Raman spectroscopy revealed strong local differences in crystallinity ranging from highly microcrystalline towards amorphous, even on the same sample (Fig. 4.2). The appearing thickness-inhomogeneity given by the spots introduces more amorphous zones (Fig. 4.2 a & b), while the rest remains microcrystalline. For the highest SiH_4 concentration, however, the amorphous zone was enlarged to the surface in between the circle and the surrounding square; inside the circle as well as outside the square μc-Si:H material was grown.

In Fig. 4.3 Raman spectra show measured from the glass side – the initial growth zone – strongly amorphous structured characteristics for the edges, while the layer is microcrystalline in the centre of the sample. Measured on the surface side of fully grown layer, the difference

in crystallinity seems to be less pronounced.

The analysis of the corresponding Raman crystallinity factor ϕ_c as shown in Fig. 4.4 confirms the strong differences in ϕ_c between the centre (grey bar) and the edge (hashed bar). While ϕ_c from the surface side as well as from the glass side revealed microcrystalline layers Si:H ($\phi_c > 0.5$) for the centre, amorphous layers ($\phi_c < 0.5$) were obtained in the edge.

However, ***changing the excitation frequency for 135.6 MHz to 70.0 MHz could not help avoiding inhomogeneity in the high-pressure regime.***

The question of importance was: “What causes this inhomogeneity and how can it be removed?”

The introduction of the plasma confinement box and its showerhead are thought to confine the plasma. However, this change in electrode design might influence the gas flux dynamics inside the box, by additional turbulences that occur in the high-pressure regime.

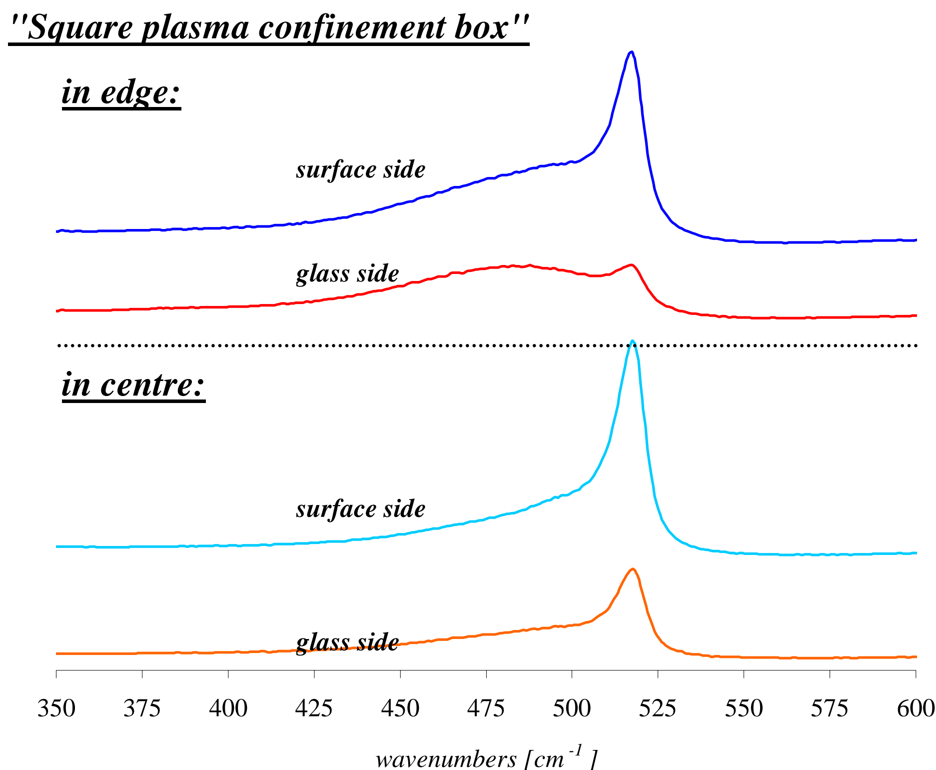

Fig. 4.3: Raman spectra of intrinsic μc-Si:H layer (Fig. 4.2 b) deposited in the square plasma confinement box illustrating local differences in crystallinity in the centre and the edge (measured from glass and surface side).

The increase of the industrial plasma excitation frequency (13.56 MHz) to the range of Very High Frequencies is reported to increase the deposition rate of Si:H layers. However, this beneficial effect is accompanied by the inconvenience of a less uniform deposition. In small

surface research reactors the loss was so far reported to be negligible in the VHF range, while the uniformity is an essential concern for large-area deposition [102]. In our small surface reactor working in the high-pressure high power regime, however, we seem to be concerned by the problem of inhomogeneity, even for surfaces as small as ~8 × 8 cm^2.

Based on the suspicion of disturbing turbulences in the gas flux dynamics, two modifications of the plasma confinement box were studied. In a first approach the gas outlet holes in the plasma confinement box were made smaller. In a second approach an additional gas outlet hole was added in each edge of the square plasma confinement box. However, neither of these two modifications improved the inhomogeneity.

Thus, we can exclude a disturbed gas flux dynamics within the plasma confinement box to be the origin of the inhomogeneity issue in the high-pressure regime (3 mbar).

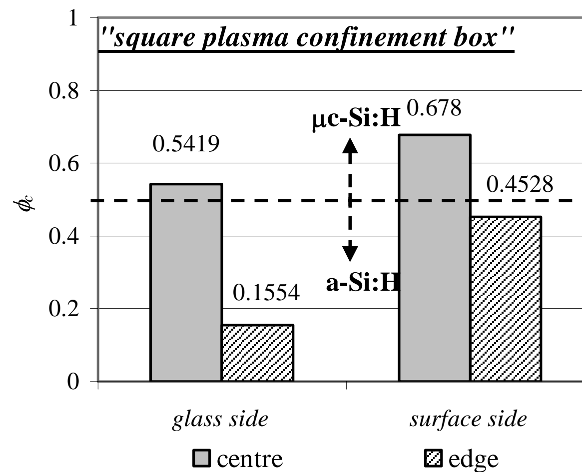

Fig. 4.4: Raman crystallinity factor ϕ_c from glass and surface side (sample Fig. 4.2 b) in the centre and in an edge.

In the high-pressure high power regime we can assume that due to the square geometry of the plasma confinement box we have a strongly inhomogeneous inter-electrode voltage distribution over the electrode area. Furthermore, it is known that a symmetrical geometry of the electrode would have a beneficial influence on the homogeneity.

4.2. Redevelopment of the plasma confinement box design

Thereupon, a new symmetric plasma confinement box design was developed. With respect to symmetry, edges are avoided by choosing a round shape, i.e. a cylindrical confinement box (Fig. 4.5 & Appendix B).

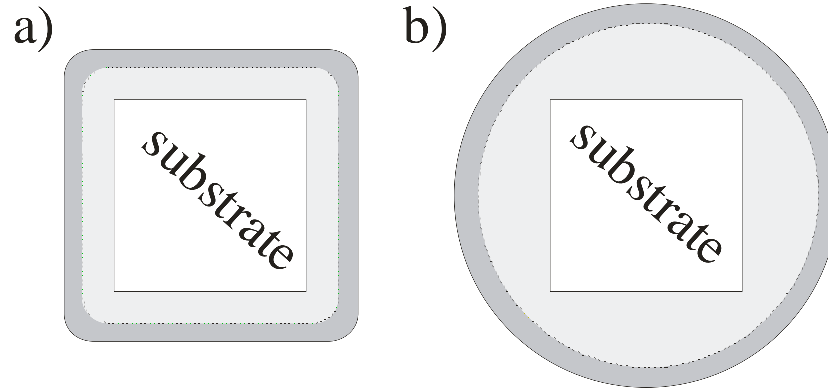

Fig. 4.5: Sketch of top view of square (a) and cylindrical (b) plasma confinement box.

Experimental:

The experimental parameters were chosen in the same range as used for the square plasma confinement box (chapter 4.1) and adapted to the new cylindrical design – it has a larger electrode surface of ~132 cm^2 instead of ~100 cm^2. However, we applied in this study (with the round box) only the excitation frequency of 70.0 MHz. All other experimental parameters were the same as described in chapter 4.1.

The plasma confinement box of the system was modified the in the present work from its initial square to a cylindrical shape (Fig. 4.5) keeping the previous distance of the gap d_{gap} at 20 mm.

Results and discussion:

The new cylindrical design (Fig. 4.5 b) enables in the high-pressure (3 mbar) high-power regime the deposition of homogeneous μc-Si:H layers compared to the square design.

The spots completely disappeared and homogeneous μc-Si:H deposition was achieved over the whole substrate. The Raman spectra of Fig. 4.6 measured in the centre and in the edges of the substrate show hardly any local difference in Raman crystallinity factor ϕ_c (Fig. 4.7). Comparing the Raman crystallinty factor ϕ_c of the Raman spectra, the ϕ_c-value of the centre is even slightly lower than the ϕ_c-value of the edge, for the cylindrical design (This

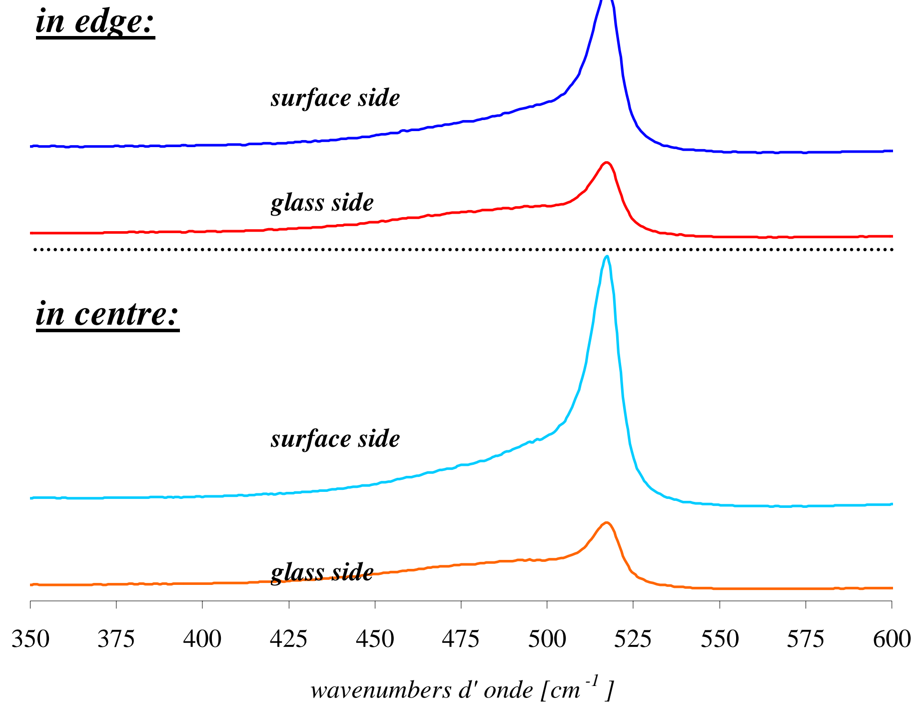

Fig. 4.6: Raman spectra of intrinsic μc-Si:H layer deposited in the cylindrical plasma confinement box illustrating local differences in crystallinity on the initial growth (glass) side and on the layer surface side.

is just the opposite of what is seen for the square shaped electrode). On the surface side the ϕ_c-values vary between 0.64 in the centre and 0.68 in the edge. On the glass side the ϕ_c-values are at lower levels of 0.42 in the centre and 0.45 in the edge. Compared to the square plasma

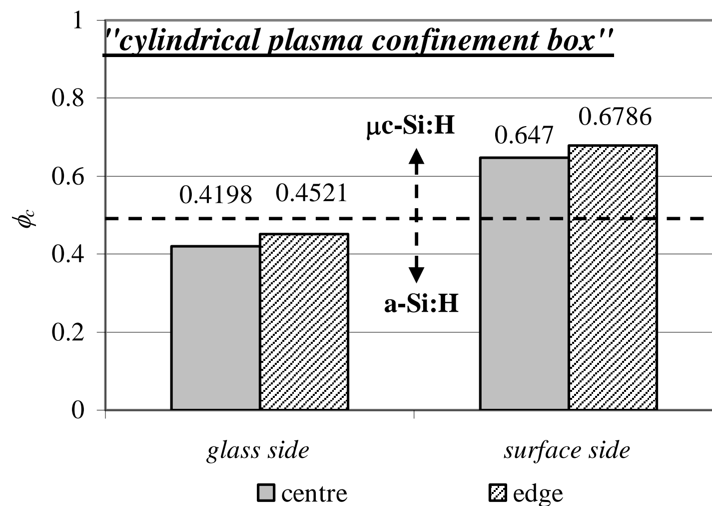

Fig. 4.7: Raman crystallinity factor ϕ_c from glass and surface side in the centre and in an edge for the cylindrical plasma confinement box.

confinement box, we now attain the same best ϕ_c-value of 0.68 (Fig. 4.4) as seen previously only in the centre now almost uniformly over the whole substrate (on the surface side). As seen from the glass side – i.e. for the initial growth zone- however, the best ϕ_c-value of 0.54 obtained for the square design slightly decreased for the cylindrical design to ~0.45. We attribute this to the increased SiH_4 concentration; this could be slightly adapted to attain a higher Raman crystallinity factor.

Thanks to the same measures (i.e. replacement of square electrode by cylindrical electrode), the risk of clogging the gas outlet holes of the plasma confinement box by the undesired silicon powder – this is a side-product of the high-pressure regime- was reduced. However, the powder formation itself was not reduced by this modification.

In the next chapter we will focus more on the aspect of reducing powder formation.

Conclusions:

By the introduction of a ***cylindrical design for the plasma confinement box***, the deposition uniformity reveals locally no more any strong differences in ***homogeneity over the whole substrate***. The only remaining inhomogeneity is a gradient of the Raman crystallinity factor ϕ_c from the glass side to the surface.

The change of the plasma confinement box design to a cylindrical shape resolved the issue of homogeneity in the high-pressure regime, at least for small laboratory –size reactors at 70.0 MHz excitation frequency.

4.3. Optimisation of d_{gap} for the high-pressure regime

It is known that higher working pressures (> 1mbar) during plasma-assisted deposition gives a further possibility to increase the deposition rate of μc-Si:H layers, as shown in chapter 2.2. However, this beneficial effect is accompanied by the inconvenience of increasing powder formation for increasing pressure.

Increasing the working pressure leads to an ***increase in the collisions of SiH_4 and H_2 molecules in the plasma confinement box***, and therefore a ***higher density of ions and radicals is created***. Hereby, higher pressure leads to an ***increased mean residence time $\tau_{res.}$ of the radicals in the plasma confinement box***. High residence time of SiH_4 derivatives, such as radicals, however, not only can increase the deposition rate of the μc-Si:H growth, but favours as well silicon powder formation, especially if atomic hydrogen is not present in sufficient quantities.

The ***residence time $\tau_{res.}$ of silane radicals*** in the plasma zone is a ***key parameter for the silicon powder formation***. How can $\tau_{res.}$ ***be reduced*** so as to avoid powder formation, but still assure high growth-rates of µc-Si:H layers. It seems that one of the methods to achieve this goal is the ***reduction of the inter-electrode gap distance d_{gap}***.

B. Chapman has established an equation (Equ. 4.1) for ***calculating the mean residence time $\tau_{res.}$ of a molecule within a defined volume***. The formula given by Chapman is based only on the gas flow rate, and does not consider the pumping rate of the process gas [103].

In the case of our plasma confinement box – for the cylindrical one-, we adapted the given equation of Chapman to our configuration. As chamber volume for the calculation, we only considered the volume of the confinement box. In our case, the volume is then defined by the fixed showerhead surface A of 132 cm^2, and by the variable inter-electrode gap distance d_{gap} (we can chose from 4 different distances).

We can then write:

$$\tau_{res.} = 7.9 \times 10^{-5} \times \frac{p_{depot}(mbar) \times A(cm^2) \times d_{gap}(cm)}{\phi_{total}(sccm)} \, [s] \qquad \text{Equ. 4.1}$$

It is known that the ***tendency of hydrogen for leaving the chamber*** – caused by its kinetics- is ***much higher***, and that hydrogen is ***also pumped much faster than SiH_4*** – both is due to the large difference in molecular mass and their molecular geometry. This probably leads in our system to a ***decreased density of atomic hydrogen***, especially in our case where the reduction valve of the gas outlet is the limiting factor.

However, doing this calculation we assumed that the SiH_4/H_2 ratio, influenced by the different pumping speeds, remains the same during the plasma deposition -the SiH_4 depletion case is hereby excluded. Therefore, the calculated residence time $\tau_{res.}$ of the series shown in Fig. 4.8 will not be the exact value of SiH_4 derivatives, but the relative tendency of $\tau_{res.}$ remains correct within the pressure series.

We presume that the process-pumping system used in our present deposition system is oversized (it has a pumping rate of about 4.2 m^3/ min. for a chamber volume of about 16 litre). Because of the oversized pump used, we had to limit the pumping speed with a reduction valve, otherwise high-pressures could not be obtained. It is then the very high “resistance” of the reduction valve to gas flows that determines the pressure obtained in the reactor chamber and, therefore, takes influence on $\tau_{res.}$.

Experimental:

As the plasma confinement box was modified, as described in the previous chapter, the showerhead as well had to be changed from square to cylindrical. At the same moment, the new design was planned so as to be able to select between 4 different inter-electrode distances d_{gap} of 20.0, 16.5, 13.0 and 9.5 mm. Therefore, during the growth-rate study of intrinsic µc-Si:H layers for different values of d_{gap} (chapter 2.1) powder formation was studied as well, for the different system configurations and process conditions.

Results and discussion:

Working with a d_{gap} of 20.0 mm in the high-pressure regime (> 2 mbar), silicon powder formation is observed for both designs of the plasma confinement box, the square as well as the cylindrical shape. The only difference for powder formation between the two designs is that for the square design, the gas outlet holes were often clogged with powder –especially the ones in the edges- and powder could stick on the substrate edges. Nevertheless, powder formation may not really disturb the deposition. This is at least claimed for deposition of a-Si:H layers [78], but powder formation surely competes with source-gas utilisation for the case of high deposition rate.

Changing the shape of the plasma confinement box to a ***round*** one, certainly ***avoids*** the ***clogging of gas outlet holes in the box by silicon powder***.

For the pressure series of the intrinsic µc-Si:H high-rate layers in chapter 2.1, we then observed the following behaviour of powder formation during the variation of d_{gap}.

For the pressure series at a d_{gap} of 20.0 mm the formation of powder was observed from 2 mbar on. Decreasing the gap to 16.5 mm first powder formation was observed at about 2.5 mbar. So far, the quantity of visually observed powder formation did not change. However, for a d_{gap} of only 13.5 mm the quantity of produced powder drastically decreased – as visually observed by eye - and only appeared at pressures above 3 mbar. A further decrease of d_{gap} to 9.5 mm led to the disappearance of powder formation throughout the whole pressure series (1- 8 mbar).

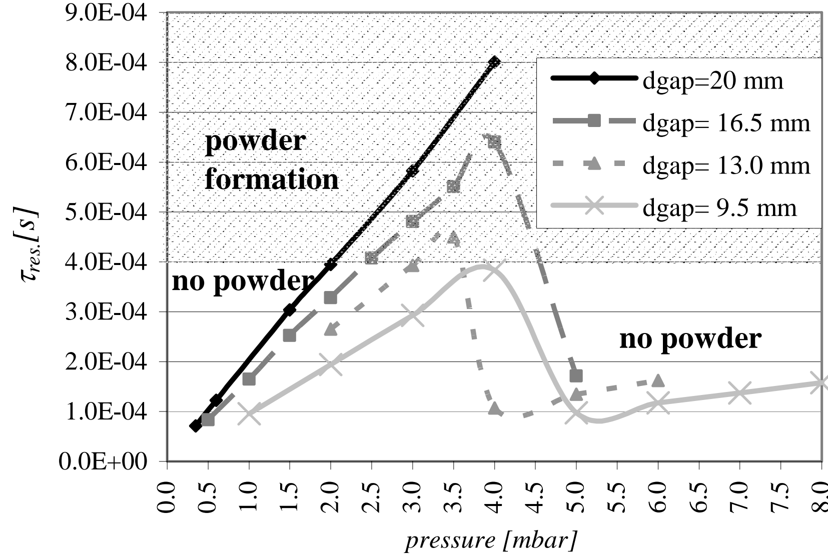

Fig. 4.8: Calculated value of $\tau_{res.}$ according to Equ. 4.1 (the lines are a guide to the eyes) as function of the process pressure, these calculated values are based on the experimental values of total gas flow ϕ_{total} (as shown in Tab. 2.1 of pressure-series Fig. 2.6) for different values of d_{gap}.

As powder formation may, indeed, have a detrimental role on devices (and may lead to shunts) all further developments in the high-pressure regime have been done at d_{gap}= 9.5 mm.

We expect that the mean time of ***residence $\tau_{res.}$ of SiH_4***, resp. its ***derivative radicals play a key role for silicon powder formation***. Therefore, we calculated $\tau_{res.}$ by equation 4.1 (using the experimental total gas flow rates of SiH_4 and H_2) for the 4 different inter-electrode gap distances d_{gap} in the range of 20.0 to 9.5 mm. Question of interest was to link the calculated $\tau_{res.}$ and the experimentally observed powder regimes to find an influence of pressure and d_{gap}.

The lines in Fig. 4.8 are a guide to the eye, they first show a linear increase of $\tau_{res.}$ for a constant total gas flow rates. Only when the gas flow rate was experimentally increased, $\tau_{res.}$ decreased. Linking the evolution of the calculated $\tau_{res.}$-values to the experimentally observed pressure-values where powder formation appears, we can clearly separate between a no powder regime (Fig. 4.8 lower transparent zone) and a powder formation regime (Fig. 4.8 hashed zone). For decreased $\tau_{res.}$ -values at higher pressures (≥ 4 mbar), however, the deposition rate of corresponding intrinsic μc-Si:H layers was also drastically decreased (Fig. 2.6 pressure-series) – probably due to increased hydrogen etching [50].

Due to the suspected limitation of $\tau_{res.}$ by the pumping speed and the reduction valve and not by the process gas flow rate, we must assume that the mean residence time calculated according to Equ. 4.1 strongly deviates from the real value in the process. Nevertheless, a relative comparison between the different values for d_{gap} remains valid.

<u>*Conlusions:*</u>

The series in ***decreasing*** $\boldsymbol{d_{gap}}$ revealed a decreasing silicon powder formation. At a $\boldsymbol{d_{gap}}$ ***of 9.5 mm powder formation*** was even ***no longer observed*** at all.

Appendix

A Novel ZnO lift-off structuring tool for p-i-n solar cells

A new structuring method for laboratory-scale solar cells on 8×4 cm^2 substrates was introduced to avoid the problem of non reproducibility of exact surface for the solar cells of laboratory size (< 1 cm^2). The challenge was to develop a method which is simple and quick (5 – 10 min.) and still exact in surface reproducibility.

Fig. A.1: novel structuring tool with necessary marker (Staedtler size S).

The novel strategy is a positive masking of the Si:H layers (cells are not covered) before deposition of the back ZnO contact, followed afterwards by separate ZnO lift-off and Si:H layer etching of the surface that is not covered by ZnO.

Structuring process:

1. The substrate with the raw solar cell (TCO/ p-/ i-/ n- layer) is fixed by hand in the first pocket of the structuring tool (Fig. A.1). The circles of the mask are drawn (not filled!) with a marker (type: Staedtler with tip S) keeping it straight and perpendicular to the substrate (see Fig. A.2 a). This is repeated in the other pockets of the structuring tool, so that 16 solar cells of a surface of 0.19 cm^2 are obtained on the substrate surface of 4×4 cm^2.

The substrate is taken out of the pocket and all or part of the outer circle surface is also covered by marker (Fig. A.3 b).

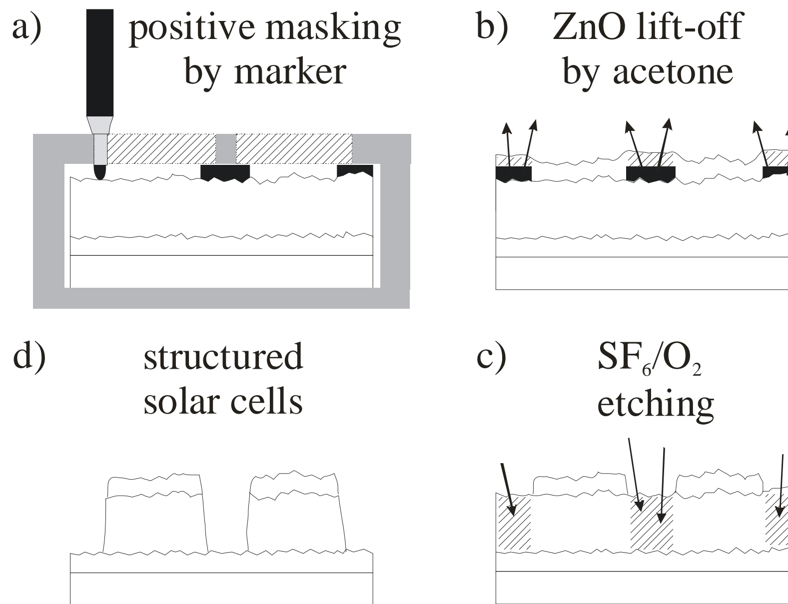

Fig. A.2: Schematic structuring of thin-film solar cells: a) negative masking on Si:H layers by marker b) partially lift-off of ZnO by acetone, followed by polish with a smooth towel before c) etching of Si:H layers.

2. TCO (back ZnO) deposition is carried out.
3. ZnO lift-off by dip of substrate with its back contact in an acetone bath – marker dissolves and ZnO is peeled off (step Fig. A.2 b to c).
   In order to avoid “ZnO crumbs” on the cell boarder – they can short circuit a cell-, the structured ZnO surface has to be cleaned until no crumbs are visible by eye. Therefore, the sample is first cleaned with a strong air jet and then polished by a smooth clean room wipe (TechniCloth ® V whipers (blend)).
4. The Si:H layer –except for the ZnO covered parts- is etched by SF_6/O_2 etching gas in the IPL (Integrated Plasma Limited) 200 E etching system during 3- 5 min.
5. 16 solar cells of 0.19 cm^2 surface size are obtained (Fig. A.3 c)

The new structuring method demands a very precise handwork with the marker.
A proper blow off of the ZnO cumbs after the ZnO lift-off followed by polishing is crucial to attain good uniformity over the whole substrate.
This structuring method demands as well a certain experience – do not start with the “best solar cell”, but with samples of simple Si:H layers to get the exercise. If work is not done

properly, the structured surfaces can have different sizes! Note, different TCOs can influence the structuring results, e.g. the surfaces are not the same. However, for IMT standard LP-CVD ZnO the structuring method works properly.

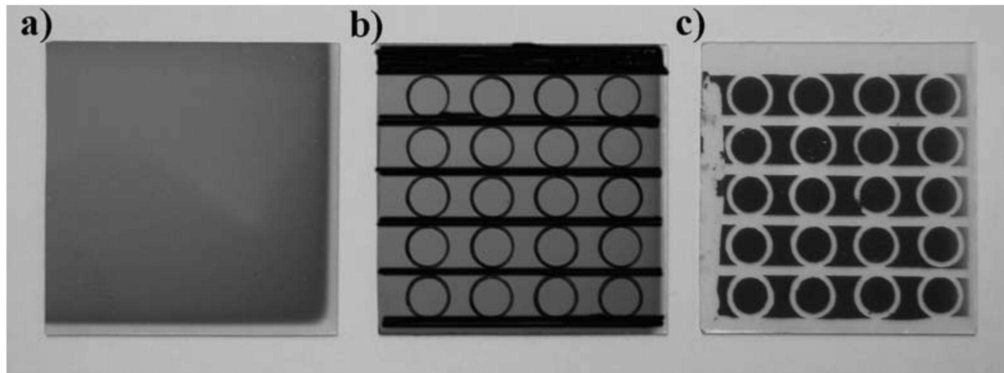

Fig. A.3: 3 steps during structuring: a) raw layer solar cells, b) positive masked by marker, c) 16 laboratory size (0.19 cm^2) structured solar cells.

The whole structuring process (except for the TCO deposition) takes about 5 minutes and shows a much better uniformity of the solar cell characteristics (see Fig. A.3), as compared with the previous structuring method of IMT (P70-structuring: masking after back contact).

B Evolution of plasma confinement box

So far, latest IMT "state-of-the-art" electrode design consisted of a square plasma confinement box as shown in Fig. B.2 a). The electrode consisted of a showerhead cathode of 100×100 mm^2 dimension (surface= 100 cm^2) with a fixed distance to the substrate (d_{gap}) of 20.0 mm.

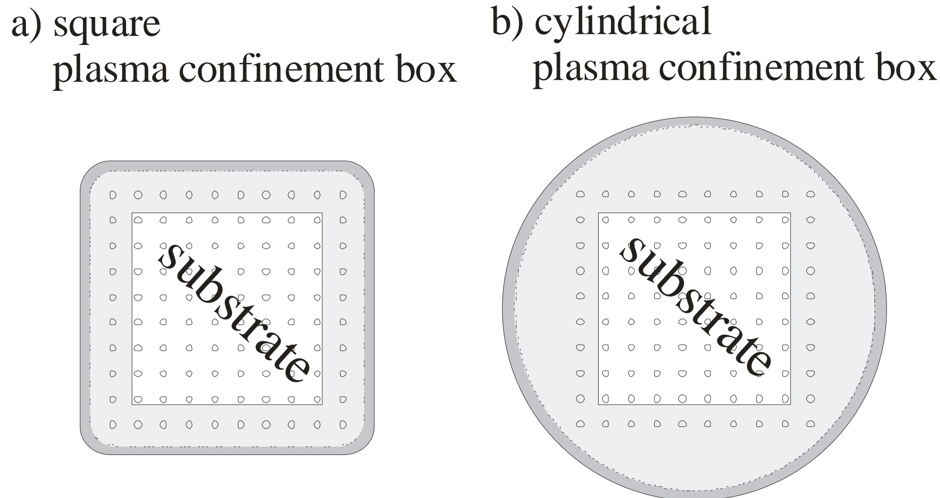

Fig. B.1: Schematic outline of top view of a) the square and b) the redeveloped cylindrical plasma confinement box.

As reported in chapter 4.1, the enlargement of the range of the working pressure p to the high-pressure regime (1 mbar < p > 10 mbar) led to a strong inhomogeneity of the deposited layer thickness uniformity and of the crystallinity over the whole substrate. The Raman crystallinity factor locally varied between very microcrystalline (ϕ_c> 0.5) and completely amorphous (ϕ_c<< 0.5). Therefore, the electrode design was redeveloped to avoid these inhomogeneities. We suspect that the inhomogeneities which are observed in the high-pressure regime (see also chapters as 2.2 & 4.1) are caused by a disturbing interaction of the edges of the plasma confinement box with the electrical VHF-field. Due to the known influence of the geometry on the VHF-field distribution over an electrode – the plasma confinement box is the mass and the showerhead the cathode-, we changed to a totally symmetric shape, i.e. to a cylindrical box (Fig. B.1 b).

The new cylindrical plasma confinement box is designed to be modular, e.g. the showerhead is only fixed by a screw on the VHF-input and can be exchanged with another design any time. In our case we developed four different showerhead-plates to have different gap distances between 20.0 and 9.5 mm (d_{gap}= 20.0/ 16.5/ 13.0/ 9.5 mm). Furthermore, a so-called "Hollow-effect"-showerhead electrode was recently developed according to idea as presented

by Ch. Niikura [104] – however, because of lack of time no deposition could be carried out with this new hollow electrode anymore. Therefore, this work will not be further discussed in this thesis.

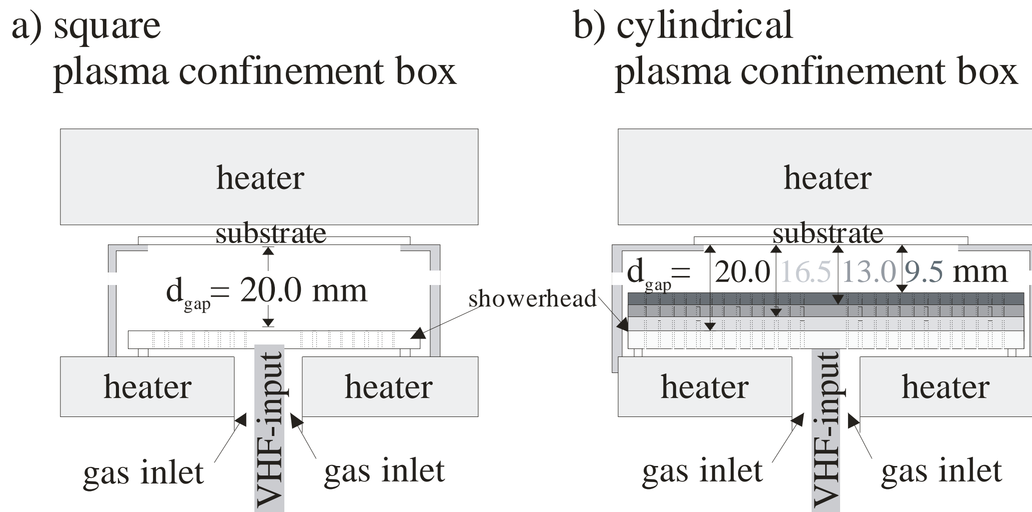

Fig. B.2: Schematic side view of the electrode design with a) the square and b) the newly developed cylindrical plasma confinement box. In contrast with the square box (fixed gap of 20 mm), the cylindrical box has a variable gap of 20.0/ 16.5/ 13.0 or 9.5 mm distance.

The change to a cylindrical shape introduced a larger showerhead surface of about 132 cm^2 instead of 100 cm^2 for the square shape. Due to the changed dimensions of the geometry, the process-parameters of the previous square plasma confinement box had to be slightly re-adapted. Indeed, 30% more VHF-power is needed to have the same power-density as before.

C Characterisation of the plasma confinement box:

In order to make precise experiments, it is necessary to know the transient characteristics of the deposition chamber. The deposition system used for this thesis (System A of IMT) does not consist of a simple parallel plate electrode design but uses a plasma confinement box.

This study focuses, on one hand, on the temperature of the substrate (for d_{gap}= 20 mm) and, on the other hand, on the pressure in the plasma confinement box, to clarify any differences with a deposition system with standard parallel plate electrodes.

C.1 Calibration of $T_{substr}(T_{heater})$

The temperature of the substrate (T_{substr}) was observed as a function of the regulated heater temperature (T_{heater}).

Hereby, T_{substr} was evaluated by PT100 temperature sensors which were fixed on the deposition side of a glass substrate in the substrate holder.

The ***temperature stabilisation*** was done ***under hydrogen flux*** (using flux values of 25/ 100 sccm) and ***without igniting a plasma*** for pressures ranging from 0.1 mbar to 3 mbar, while measuring the time. The temperature was assumed to be stable, when the change in $T_{substr.}$ no longer exceeded 1 - 2 °C during a 5 min period. These stabilisation experiments were carried out for T_{heater}–values of 180, 200 and 220 °C.

	T_{heater}= 180°C		T_{heater}= 200°C		T_{heater}= 220°C	
p [mbar]	$T_{substr.}$ [°C]	$\Delta T_{heat.-substr.}$ [°C]	$T_{substr.}$ [°C]	$\Delta T_{heat.-substr.}$ [°C]	$T_{substr.}$ [°C]	$\Delta T_{heat.-substr.}$ [°C]
0.1	159	21	176	24	194	26
0.3	167	13	187	13	203	17
1.5	175	5	193	7	211	9
3.0	176	4	194	6	214	6

Table.C.1: Summary the maximal T_{substr}. (1st column) and the difference between $T_{substr.}$ and T_{heater} (2nd column) for various pressures (hydrogen) and for different values T_{heater} of heater temperature.

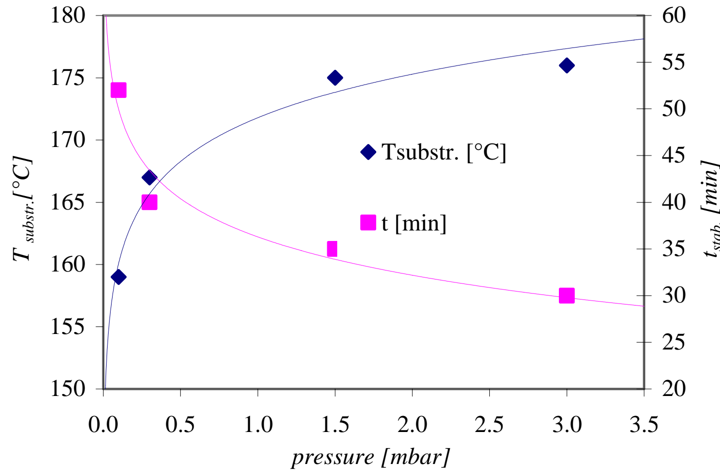

Fig. C.1: Calibration curve of the Substrate temperature and corresponding temperature stabilisation time as function of the chamber pressure.

Fig. C.1 shows the stabilized values of T_{substr} for T_{heater} at 180 °C and the stabilisation time ($t_{stab.}$) as function of the chamber pressure. Hereby, it is observed that the temperature stabilisation takes place faster, if the chamber pressure is higher. Furthermore, higher pressures give rise to a smaller difference between $T_{substr.}$ and T_{heater}; indeed, this is what one expects, because of the higher heat transmission due to the increased molecule density in the chamber. This tendency is confirmed as well for T_{heater}= 200 and 220 °C and summarized in Table C.1.

C.2 Influence of the chamber pressure to the plasma confinement box

Up to now, the pressure in the plasma confinement box ($p_{plasma\ conf.\ box}$) was assumed to be the same as the chamber pressure ($p_{chamber}$). This point has to be clarified.

It could be possible that the special design of the plasma confinement box with its gas inlet by the showerhead and the holes of gas outlet on the confinement box leads to a significant difference in pressure between the chamber and the plasma confinement box, especially when working in the high-pressure regime (>1 mbar).

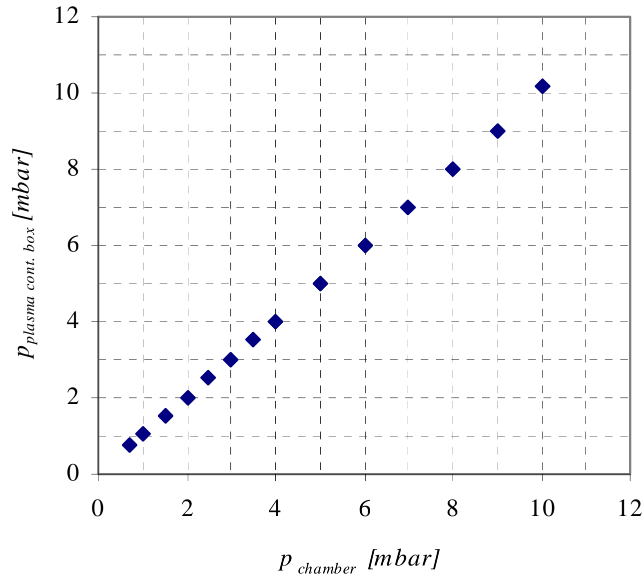

Fig C.2: The dependence of the pressure in the chamber ($p_{chamber}$) vs. the pressure in the plasma confinement box ($p_{plasma\ conf.}$) is shown for the pressure range from 1 to 10 mbar.

Therefore, a second pressure sensor directly connected to the plasma confinement box by a small tube was installed. The experiments were carried out at gap distances of 16.5 mm and 9.5 mm (typical values for the high-pressure regime), using hydrogen fluxes of 100 and 300 sccm and for the pressure interval ranging from 0.5 to 10 mbar. No plasma was ignited.

The pressure series (Fig. C.2) did not confirm our initial suspicion of a difference in pressure between the pressure as "seen" by the regulator situated in the chamber (but outside of the box) and the actual measured pressure with the plasma confinement box. A linear behaviour without any difference in pressure is clearly shown in the graph for the whole range from 0.5 to 10 mbar. The same behaviour is observed for both d_{gap} of 9.5 mm as well as for 16.5 mm.

References

1. Bundesam für Energie, *"Überblick über den Energieverbrauch der Schweiz im Jahr 2004"*, in *Auszug aus der Schweizerischen Gesamtenergiestatistik*. 2004.
2. SEMATECH, *"Global Warming: A White Paper on the Science, Policies and Control"*, in *Technologies that Impact the U.S. Semiconductor Industry*. 1994.
3. Heller, A. and A. Dietrich, *"Sorry, leider beginnt schon die zweite Halbzeit"*, in *NZZ Folio*. 2004: Zürich. p. 42- 45.
4. WIKIPEDIA, *freie Enzyklopädie*. 2005.
5. Markvart, T., *"Solar electricity"*. 2nd ed. ed. 2000: John Wiley & Sons.
6. The Associated Press, *"Barrel price"*. 2005.
7. Nakajima, A., et al. *"Improvement on actual output power of thin film silicon hybrid module"*. in *3rd World Conference on Photovoltaic Energy Conversion (WEPEC)*. 2003. Osaka, Japan.
8. Meier, J., et al., *"Intrinsic microcrystalline silicon (μc-Si:H)- a promising new thin film solar cell material"*. 1st World Conference on Photovoltaic Energy Conversion (WCPEC), 1994. **Vol. 1**: p. 409-412.
9. Meier, J., et al. *High-efficiency amorhpous and "micromorph" silicon solar cells*. in *3rd World Conference on Photovoltaic Energy Conversion (WCPEC3)*. 2003. Osaka.
10. Noda, M., et al. *"Large area thin film Si tandem module production using VHF plasma with a ladder-shaped electrode"*. in *3rd World Conference on Photovoltaic Energy Conversion (WCPEC)*. 2003. Osaka, Japan.
11. Repmann, T., et al. *"Advanced PECVD Processes for Thin Film Silicon Solar Cells on Glass"*. in *19th European Photovoltaic Specialist Conference (EU-PVSEC)*. 2004. Paris, France.
12. Yamamoto, K., et al., *"A high efficiency thin-film silicon solar cell and module"*. Solar Energy Materials and Solar Cells, 2004. **Vol. 77**: p. 939-949.
13. Benagli, S., et al. *"Amorphour silicon single-junction p-i-n solar cells prepared in industrial KAI (TM) PECVD reactor"*. in *20th European Photovoltaic Solar Energy Conference (EU-PVSEC)*. 2005. Barcelona.
14. Meier, J., et al. *"Amorphous Silicon single-junction and "Micromorph" tandem solar cells pprepared in UNAXIS KAI PECVD single-chamber reactors"*. in *20th EUPhotovoltaic Solar Energy Conference (EU-PVSEC)*. 2005. Barcelona, Spain.
15. Veprek, S. and V. Marecek, *"The preparation of thin layers of Ge and Si by chemical hydrogen plasma transport"*. Solid State Electronics, 1968. **Vol. 11**: p. 683-684.

16. Lucovsky, G., et al., *Deposition of μc-Si and μc-Si-C thin films by remote plasma-enhanced chemical-vapor deposition.* Solar Cells, 1991(30): p. 419-434.
17. Vallat-Sauvain, E., et al., *"Evolution of the microstructure in microcrystalline silicon prepared by very high frequency glow-discharge using hydrogen dilution".* Journal of Applied Physics, 2000. **Vol. 87**: p. 3137-3142.
18. Ziegler, Y., et al., *"More stable low gap a-Si:H layers deposited byPE-CVD at moderately high temperature with hydrogen dilution".* Solar Energy Materials & Solar Cells, 2001. **66**: p. 413- 419.
19. Meillaud, F., et al. *"Light-induced degradation of thin-film microcrystalline silicon solar cells".* in *31th IEEE Photovoltaic Specialist Conference*. 2005. Lake Buena Vista, FL, USA.
20. Shah, A., *"Matériaux électroniques amorphes".* 3ème ed. 1995: EPFL - Université de Neuchâtel. 65.
21. Hovel, H.J., *"Solar Cells".* "Semiconductors and Semimetals", ed. R.K. Williardson and A.C. Beer. Vol. Vol. II. 1975, New York: Academic Press.
22. Faÿ, S., *"L'oxyde de zinc par dépôt chimique en phase vapeur comme contact électrique transparent et diffuseur de lumière pour les cellules solaires"*, in *Intitut de Microtechnique*. 2003, Neuchâtel: Neuchâtel.
23. LeComber, P.G. and W.E. Spear, *"PECVD: plasma enhanced chemical vapor deposition".* Physical Review Letters, 1970. **Vol. 25**: p. 509.
24. LeComber, P.G., A. Madan, and W.E. Spear, Journal of Non Crystalline Solids, 1972. **Vol. 11**: p. 219.
25. Curtins, H., N. Wyrsch, and A. Shah, *"High-rate deposition of amorphous hydrogenated silicon : effect of plasma excitation frequency".* Electronic Letters, 1987. **Vol. 23**: p. 228-230.
26. Howling, A.A., et al., *"Frequency effects in silane plasma for plasma enhanced chemical vapor deposition".* Journal of Vacuum Science & Technology A, 1992. **Vol. 10**: p. 1080-1085.
27. Roschek, T., et al. *"Microcrystalline silicon solar cells prepared by 13.56 MHz PECVD at high growth rates: Solar cell and material properties".* in *Material Research Society Symposium (MRS)*. 2001. San Francisco, CA, U.S.A.
28. Roschek, T., et al., *"Comprehensive study of microcrystalline silicon solar cells deposited at high rates using 13.56 MHz plasma-enhanced chemical vapor deposition".* Journal of vaccum science and technology A, 2002. **Vol. 20**: p. 492-498.
29. Matsui, T., M. Kondo, and A. Matsuda, *"Origin of the Improved Performance of High-Deposition-Rate Microcrystalline Silicon Solar Cells by High-Pressure Glow Discharge".* Japanese Journal of Applied Physics, 2003. **Vol. 42**: p. 901- 903.
30. Mai, Y., et al. *"Microcrystalline silicon solar cells deposited at high rates by combination of VHF-PECVD and high working pressure".* in *19th EU Photovoltaic Solar Energy Conference (EU-PVSEC)*. 2004. Paris, France.
31. Kroll, U., *"VHF-Plasmaabscheidung von amorphem Silizium: Einfluss der Anregungsfrequenz, der Reaktorgestaltung sowie Schichteigenschaften"*, in *Institut de Microtechnique*. 1994, Université de Neuchâtel: Neuchâtel.

32. Meier, J., et al., *"Microcrystalline single junction and micromorph tandem thin film silicon solar cells".* Material Research Society Symposium Proceedings, 1998. **Vol. 507**: p. 139-144.
33. Torres, P., et al. *"Fast deposited microcrystalline solar cells".* in *26th IEEE Photovoltaic Specialists Conference*. 1997. Anaheim, CA, U.S.A.
34. Torres, P., et al., *"Device grade microcrystalline silicon owing to reduced oxygen contamination".* Applied Physics Letters, 1996. **Vol. 69**: p. 1373-1375.
35. Droz, C., et al. *"Electrical and microstructural characterisation of microcrystalline silicon layers and solar cells".* in *3rd World Conference on Photovoltaic Energy Conversion (WCPEC)*. 2003. Osaka.
36. Droz, C., et al., *"Relationship between Raman crystallinity and open-circuit voltage in microcrystalline silicon solar cells".* Solar Energy Materials and Solar Cells, 2004. **Vol. 81**: p. 61-71.
37. Vetterl, O., *Thesis*, in *Forschungszentrum Jülich GmbH*. 2001: Jülich.
38. Droz, C., et al. *Application of Raman spectroscopy for the microstructure characterisation in microcrystalline silicon solar cells.* in *17th European Photovoltaic Solar Energy Conference*. 2001. Münich, Germany.
39. Hang, Z., H. Shen, and F.H. Pollak, *"Comprehensive Investigation of Polish-Induced Surface Strain in (100) and (111) Gaas and Inp".* Journal of Applied Physics, 1988. **Vol. 64**(6): p. 3233.
40. Paillard, V., P. Puech, and P. Roca I Cabarrocas, Journal of Non-Crystalline Solids, 2002. **Vol.**: p. 299-302.
41. Beck, N., et al., *"Enhanced optical absorption in microcrystalline silicon".* J. Non-Cryst. Solids, 1996. **Vol. 198-200**: p. 903.
42. Bustarret, E., M.A. Hachicha, and M. Brunel, *"Experimental Determination of the Nanocrystalline Volume Fraction in Silicon Thin-Films from Raman Spectroscopy".* Applied Physics Letters, 1988. **Vol. 52**(20): p. 1675.
43. Tsu, R., et al., *"Critical volume fraction of crystallinity for conductivity percolation in phosphorus-doped Si:F:H alloys".* Applied Physics Letters, 1982. **Vol. 40**(6): p. 534.
44. Brodsky, M.H., M. Cardona, and J.J. Coumo, *" Infrared and Raman spectra of the silicon-hydrogen bonds in amorphous silicon prepared by glow discharge and sputtering".* Physical Review B, 1977. **Vol. 16**: p. 3556.
45. Droz, C., *"Thin Film Microcrystalline Silicon Layers and Solar Cells: Microstructure and Electrical Performances"*, in *Institut de Microtechnique*. 2003, Université de Neuchâtel: Neuchâtel.
46. Overhof, H. and P. Thomas, *"Springer tracts in modern physics: Electronic transport in hydrogenated amorphous silicon"*. Vol. Vol. 114. 1989: Springer-Verlag. 26.
47. Terrazzoni-Daudrix, V., et al. *"Enhanced light trapping in thin film silicon solar cells deposited on PET and glass"*. in *3rd World Conference on Photovoltaic Energy Conversion (WCPEC)*. 2003. Osaka, Japan.
48. Poruba, A., et al., *"Fourier transform infrared photocurrent spectroscopy in microcrystalline silicon".* Journal of Non-Crystalline Solids, 2002. **Vol. 299-302**: p. 536-540.
49. Vanecek, M. and A. Poruba, *"Fourier-transform photocurrent spectroscopy of microcrystalline silicon for solar cells".* Applied Physics Letters, 2002. **Vol. 80**: p. 719-721.

50. Bailat, J., *"Growth, Microstructure and Electrical Performances of Thin Film Microcrystalline Silicon Solar Cells"*, in *Institut de Microtechnique*. 2004, Université de Neuchâtel: Neuchâtel.
51. Cody, J.D., *"Urbach edge of crystalline and amorphous silicon: a personal review".* Journal of Non-Crystalline Solids, 1992. **Vol. 141**: p. 3-15.
52. Shah, A., et al., *"Thin film silicon and solar cell technology".* Progress in photovoltaics: Research and applications, 2004. **Vol. 12**: p. 1-30.
53. Benedict, J., R. Anderson, and S.J. Klepeis, *"Recent developments in the use of the tripod polisher for tem specimen preparation".* Material Research Society Symposium Proceedings, 1992. **Vol. 254**: p. 121-139.
54. Williams, D.B. and C. Barry Carter, *"Transmission electron microscopy".* 1996, New-York: Plenum Press.
55. Dubail, J., et al., *"Microstructure of microcrystalline silicon solar cells prepared by very high frequency glow-discharge".* Material Research Society Symposium Proceedings, 2001. **Vol. 609**: p. A13.6.1-6.
56. Flueckiger, R., *"Microcrystalline Silicon Thin Films Deposited by VHF Plasmas for Solar Cell Application"*, in *Institut de Microtechnique*. 1995, Neuchâtel: Neuchâtel. p. 96.
57. Holleman, A.F. and N. Wiberg, *"Lehrbuch der Anorganischen Chemie"*, in *"Lehrbuch der Anorganischen Chemie".* 1995. p. 541.
58. Roca I Cabarrocas, P., S. Kumar, and B. Drévillon, Journal of Applied Physics, 1989. **Vol. 66**: p. 3286.
59. Ballutaud, J., et al. *"Plasma deposition of p-i-n devices using a single PECVD chamber: study of boron contamination".* in *29th EPS Conf. on Plasma Phys. and Contr. Fusion*. 2002. Montreux.
60. Beyer, W., et al. *"Alternative gases and processes for amorphous and microcrystalline silicon etching".* in *3rd World Conference on Photovoltaic Energy Conversion (WCPEC)*. 2003. Osaka, Japan.
61. Vallat-Sauvain, E., et al., *"Influence of the susbtrate morphology and chemical nature on the nucleation and growth of microcrystalline silicon".* Thin Solid Films, 2005. **to be published**.
62. Hollingsworth, R.E. and P.K. Bhat, Applied Physics Letters, 1994. **Vol. 64**(5).
63. Torres, P., *"Hydrogenated Microcrystalline Silicon Deposited by VHF-GD for Thin-Film Solar Cells"*, in *Institut de Microtechnique*. 1998, Université de Neuchâtel: Neuchâtel.
64. Vallat-Sauvain, E., et al. *"Improved Interface Between Front TCO and Microcrystalline Silicon p-i-n Cells".* in *Materials Research Society Symposium (MRS)*. 2001. San Francisco, CA. U.S.A.
65. Roschek, T., et al., *Influence of the total gas flow on the deposition of microcrystalline silicon solar cells.* Thin Solid Films, 2004. **451-452**: p. 466-469.
66. Godet, C., N. Layadi, and P. Roca I Cabarroocas, *"Role of mobile hydrogen in the amorphous silicon recrystallisation".* Appl. Phys. Lett., 1995. **Vol. 66**(23): p. 3146-3148.
67. Kalache, B., *"Ion bombardment effects on microcrystalline silicon growth mechanisms and on the film properties".* Journal of Applied Physics, 2003. **93**.
68. Strzhemechny, Y.M., et al., *"Remote hydrogen plasma processing of ZnO single crystal surfaces".* Journal of Applied Physics, 2003. **Vol. 94**(7): p. 4256- 4262.

69. Hasegawa, S., et al., *"Initial growth of polycrystalline silicon films on substrates subjected to different plasma treatments"*. Japnese Journal of Applied Physics, 1998. **Vol. 37**: p. 4711- 4717.
70. Holleman, A.F. and N. Wiberg, in *"Lehrbuch der Anorganischen Chemie"*. 1995. p. 1367.
71. Shah, A., et al. *"Microcrystalline and micromorph solar cells and modules: status and potential"*. in *31st IEEE Specialists Conference*. 2005. Orlando, U.S.A.
72. Fukawa, M., et al., *"High rate growth of microcrystalline silicon using s high-pressure depletion method with VHF plasma"*. Solar Energy Materials and Solar Cells, 2001. **Vol. 66**(1- 4): p. 217 - 223.
73. Horvath, P., K. Rozsa, and A. Gallagher. *"Polysilane production in RF SiH_4 and H_2-SiH_4 plasmas"*. in *XXI ICPIG*. 2003. Greifswald (GER).
74. Matsuda, A., J. Vac. Sci. & Technol. A, 1998. **16**: p. 365.
75. Amanatides, E., et al., *"High pressure regime of plasma enhanced deposition of microcrystalline silicon"*. J. Appl. Phys., 2005. **Vol. 97**.
76. Smith, C., et al., *"Electron beam induced fluorescence measurements of the degree of hydrogen dissociation in hydrogen plasmas"*. Plasma Cources Sci. Technolo., 2004. **Vol. 13**: p. 729- 738.
77. Kondo, M. and A. Matsuda, *"Preparation and Properties of Nanocrystalline Silicon"*, in *"Thin Film Solar Cells Next Generation photovoltaics and its Applications"*. 2004, Springer-Verlag Berlin: Heidelberg. p. 69- 89.
78. Hollenstein, C., et al. in *Material Reserach Society Symposium (MRS)*. 1998. San Francisco, U.S.A.
79. Sansonnens, L., A.A. Howling, and C. Hollenstein, Plamsa Sources Sciencs Technology, 1998. **Vol. 7**: p. 114.
80. Vanecek, M., et al., *"Direct measurement of the deep defect density in thin amorphous silicon films with the 'absolute' constant photocurrent method"*. Journal of Applied Physics, 1995. **Vol. 78**: p. 6203-6210.
81. van den Donker, M.N., et al. *"The role of plasma induced substrate heating during high rate deposition of microcrystalline silicon solar cells"*. in *European-Material Research Society (E-MRS)*. 2005. Strasbourg, France.
82. Pernet, P., *"Développement de cellules solaires en silicium amorphe de type "n-i-p" sur substrats souples"*, in *Institut de Microtechnique*. 2000, Ecole polytechnique Fédérale de Lausanne (EPFL): Neuchâtel.
83. Kubon, M., et al. in *12th EC Photovoltaic Solar Energy Conference (PVSEC)*. 1994. Amsterdam, The Netherlands.
84. Platz, R., et al., Solar Energy Materials and Solar Cells, 1997. **Vol. 46**: p. 157-172.
85. Llorte, L., et al., Applied Physics A, 1992. **Vol. 55**: p. 573.
86. Kroll, U., et al., Thin Solid Films, 2004. **Vol. 451- 452**: p. 525.
87. Ballutaud, J., et al., Thin Solid Films, 2004. **Vol. 468**: p. 222- 225.
88. Rech, B., C. Beneking, and H. Wagner, *"Improvement in stabilized efficiency of a-Si:H solar cells through optimized p/ i-interface layers"*. Solar Energy Materials and Solar Cells, 1996. **Vol. 41/42**: p. 475- 483.
89. Brotherton, S.D., P. Bradley, and A. Gill, *"Iron and the iron-boron complex in silicon"*. Journal of Applied Physics, 1985. **Vol. 57**(6): p. 1941-1943.
90. Reiss, J.H., R.R. King, and K.W. Mitchell, *"Characterization of diffusion length degradation in Czochralski silicon solar cells"*. Applied Physics Letters, 1996. **Vol. 68**(23): p. 3302-3304.

91. Istratov, A.A., H. Hieslmair, and E.R. Weber, *"Iron and its complexes in silicon".* Applied Physics A, 1999.
92. Istratov, A.A., H. Hieslmair, and E.R. Weber, *"Iron contamination in silicon technology".* Appl. Phys. A, 2000. **Vol. 70**: p. 489- 534.
93. Kimerling, L.C. and J.L. Benton, Physica B & C, 1983. **Vol. 116**: p. 297.
94. Feichtinger, L., Acta Phys. Austr., 1979. **Vol. 51**: p. 161.
95. Lemke, H., Phys. Status Solidi, 1983. **Vol. 76**: p. 223.
96. Ghatnekar-Nilsson, S., et al., *"Indentification of the iron-boron line spectrum in silicon".* Semicond. Sci. Technol., 1993. **Vol. 8**: p. 1857- 1861.
97. Langowski, J., et al., Applied Physics Letters, 1993. **Vol. 63**: p. 3043.
98. Zot, G. and W. Bergholz, Journal of Applied Physics, 1990. **Vol. 67**: p. 6764.
99. Feitknecht, L., et al. *"Correlation Between TCO-Contact Layers and Performance of Microcrystalline Silicon p-i-n Solar Cells"*. in *19th EU Photovoltaic Solar Energy Conference*. 2004. Paris (F).
100. Tanda, M., M. Kondo, and A. Matsuda, *"A novel approach of the growth of mc-Si at a high rate over 3 nm/s".* Thin Solid Films, 2003. **Vol. 427**: p. 33 - 36.
101. Vetterl, O., et al., Thin Solid Films, 2003. **Vol. 427**: p. 46.
102. Kroll, U., et al. *"Fast Deposition of a-Si:H Layers and Solar Cells in a Large-Area (40 x40 cm^2) VHF-GD Reactor"*. in *MRS Symp., Spring Meeting*. 1999. San Francisco, CA, U.S.A.
103. Chapman, B., *"Glow Discharge Processes"*. 1980: John Wiley & Sons, Inc.
104. Niikura, C., et al., *"High-rate growth of microcrystalline silicon films using a high-density SiH_4/H_2 glow -discharge plasma".* Thin Solid Films, 2004. **Vol. 457**: p. 84- 89.

Acknowledgements

I would like to thank:

Professor Arvind Shah, who motivated me to join his research group and gave me the opportunity to effectuate my thesis in the motivating, future prospectively field of photovoltaics.

Prof. Ch. Ballif, Dr. W. Beyer and Prof. G. Calzaferri who have accepted to join the examination board and be devoted their time to the reading of this thesis.

Johannes Meier, as my project leader during the first three years of my thesis, who introduced me into the world of deposition of microcrystalline silicon. It was also very fruitful to have instructive exchanges, listen to his advice and to learn about the art of microcrystalline silicon deposition.

Not to fall into oblivion, Jean-Luc Kumin of the mechanical workshop, who helped to develop and realize all modifications of on my modular deposition chamber, e.g. the plasma confinement box design.

The whole team of the "Institut für Photovoltaik" from "Forschungszentrum Jülich GmbH" in Germany under Dr. W. Beyer, who has welcomed me with open hearts for half a year. They have taught me the spirit of very high "state-of-the-art" of microcrystalline solar cell fabrication in their very exact and humorous German way. I also would like to express my special thanks to Dr. Bernd Rech and Dr. Joachim Müller, who did not only give me very precious advice for my scientific work, but also let me feel very rapidly comfortable during daily life - like back home in Switzerland. My very special thank goes to Dipl. Ing. Andreas Mück, who essentially contributed with several SIMS-measurements –specially after my stay at their institute- to explain the serious issue of the boron cross-contamination.

Thanks to my stay at the "Institut für Photovoltaik" my final phases of the practical thesis work was much "facilitated", and even more importantly: my horizon has drastically increased to encompass also knowledge other than only scientific issues.

Special thanks to the persons who helped me to master the latest measurements, analysis and the correction of my manuscript in parallel, especially during the final part of my thesis:

Fanny Meillaud, who did me the kind favour to treat “old” Raman spectroscopy data of mine and to send me the results during my stay in Germany.

Ivano Pola, Martin Python and Samuel Rosset, who carried out a lot of characterisation work on my problematic microcrystalline solar cells with enthusiasm; this finally essentially contributed to the solution of the solar cell issue of this thesis.

Roman Schlüchter, who did his best to have a reliable LP-CVD front ZnO for my p-i-n solar cell fabrication. Jerôme Steinhauser, who took all SEM-measurements which visualise the crucial impact of the pre-deposition plasmas on ZnO.

Evelyne Vallat-Sauvain, who significantly supported me during the final stage of my thesis with critical reading and correcting of the manuscript –even during her vacations. She significantly contributed to the accomplishment of this thesis by letting me benefit from her impressive scientific competence and her enthusiasm for scientific research.

Corinne Droz and Julien Bailat, who were so kind to help me in the one and other manner to edit my manuscript.

The whole group, for the good time we had together and for their good sense of humour which created a comfortable atmosphere at work.

Many other person who I did not explicitly mention but who contributed in one way or another to the accomplishment of this work.

The Swiss Federal Office of Energy (Office Fédéral de l'Energie, OFEN), for their financial support.

Last but not least my parents for their continuous encouragement and support to lead this work to a good end.